

Optical measurements of mixing processes in turbulent fluid flows

Vom Fachbereich Produktionstechnik

der

UNIVERSITÄT BREMEN

zur Erlangung des Grades
Doktor der Ingenieurwissenschaften (Dr.-Ing.)
genehmigte

Dissertation

von

M.Sc.Eng. Huixin, Li

Gutachter: Prof. Dr. Marc Avila (Universität Bremen)

Gutachter: Prof. Dr. Michael Schlüter (Technische Universität Hamburg)

Tag der mündlichen Prüfung: 07.02.2023

German Abstract

Viele Prozesse in der Chemietechnik und Ozeanografie beruhen auf der Durchmischung von Flüssigkeiten. Diese Arbeit konzentriert sich auf optische Messtechniken zur experimentellen Untersuchung der Vermischung von mischbaren Flüssigkeiten und Gasen mit Flüssigkeiten. In früheren numerischen Studien wurde die turbulente kleinskalige Durchmischung untersucht, was aufgrund der begrenzten räumlichen Auflösung der Messverfahren eine experimentelle Herausforderung darstellt. Eine weitere Schwierigkeit ergibt sich bei der aktiven Flüssigkeitsmischung. Wenn Flüssigkeiten unterschiedlicher Dichte, wie Wasser und Ethanol, gemischt werden, werden experimentelle Messungen der kleinräumigen Fluktuationen in der Turbulenz durch die optische Verzerrung aufgrund des räumlich-zeitlich variierenden Brechungsindexfeldes erschwert.

In dieser Arbeit wurde zur Untersuchung der kleinskaligen Flüssig-Flüssig-Mischung ein hochskalierter T-Mischer mit einer Höhe von 40 Millimetern gebaut. Eine hochauflösende planare laserinduzierte Fluoreszenz (PLIF) wurde in Proof-of-Concept-Experimenten zum T-Übergang eingesetzt. Die Ergebnisse zeigen, dass die Messung der kleinskaligen Durchmischung im viskos-konvektiven Bereich, in dem die Geschwindigkeit nicht schwankt, wohl aber der Skalar, möglich ist. Anschließend wurden der T-Verzweigung lange Einlasskanäle hinzugefügt und die Particle Image Velocimetry (PIV)-Technik eingesetzt, um die voll entwickelten laminaren Strömungen zu überprüfen und die Strömungsregime für verschiedene Reynoldszahlen zu untersuchen. Es wurde festgestellt, dass mit dem vorliegenden Aufbau Einlassbedingungen mit vollständig entwickelten laminaren Strömungen erreicht werden können, wenn die Reynoldszahl kleiner als 1100 ist. Der Aufbau wurde durch Wiederholung der Strömungsregime in früheren Studien validiert. Geringe Temperaturunterschiede hatten jedoch eine schwache Auswirkung auf die

Strömungsverhältnisse, was bei den nächsten Messungen vermieden werden sollte. Insgesamt ist eine qualitativ hochwertige Messung der kleinräumigen Mischdynamik im T-Mischer nun in Reichweite.

Bei aktiver Vermischung mit Flüssigkeiten unterschiedlicher Dichte führt die Vermischung in der Regel zu optischen Messfehlern. In dieser Arbeit wird eine Ray-Tracing-Simulationsmethode in einer dreidimensionalen Strömung verwendet, um die Messfehler der Strömungsgeschwindigkeit und der Strömungsbeschleunigung für die tracerbasierte Velocimetrie, d. h. die Particle Tracking Velocimetry (PTV), zu quantifizieren. Das Strömungsfeld stammt aus einer direkten numerischen Simulation der einphasigen turbulenten Vermischung von zwei mischbaren Flüssigkeiten. Die Messfehler nehmen mit zunehmendem Brechungsindexunterschied zu. Die Fehler sowohl bei der Geschwindigkeit als auch bei der Beschleunigung werden auf die räumlichen und zeitlichen Gradienten der Brechungsindizes zurückgeführt. Da PTV, PIV und PLIF die gleichen, auf geometrischer Optik basierenden Arbeitsprinzipien haben, wird angenommen, dass die Ergebnisse auch für die Messungen anderer Techniken gelten. Der thermische Einfluss im T-Mischer auf die Messfehler wird anschließend abgeschätzt und als vernachlässigbar eingestuft.

Schließlich wird die Gas-Flüssigkeits-Mischung untersucht, bei der ein schwach lösliches Gas über die Gas-Flüssigkeits-Grenzfläche übertragen wird. Dieser Prozess ist mit der Klimabilanz verbunden und hängt von Oberflächenwellen und Turbulenzen unter Wasser im Ozean ab. Unter Ausnutzung der Brechung an der Grenzfläche und der optischen Verschiebungen wird eine synthetische Schlieren-Methode zur Messung der Oberflächentopographie entwickelt. Diese Methode wird in Experimenten angewandt und ermöglicht hochpräzise Messungen von freien Oberflächenwellen. Dies ermöglicht die gleichzeitige Messung von Oberflächenwellen, Stofftransport und Turbulenz unter Wasser.

Abstract

Many processes in chemical engineering and oceanography rely on fluid mixing. This thesis focuses on optical measurement techniques to experimentally investigate miscible liquid-liquid mixing and gas-liquid mixing. Previous numerical studies have examined the turbulent small-scale mixing, which is experimentally challenging because of the limited spatial resolution of the measurement techniques. A further difficulty emerges for active fluid mixing. When fluids of different densities, such as water and ethanol are mixed, experimental measurements for the small-scale fluctuations in turbulence are impeded by the optical distortion due to the spatio-temporally varying refractive index field.

In this thesis, in order to investigate small-scale liquid-liquid mixing, an upscaled T-mixer was built with a height of 40 millimetres. A planar laser-induced fluorescence (PLIF) with high resolution was employed in proof-of-concept experiments concerning the T-junction. The results indicate that measuring the small-scale mixing in the viscous-convective range where the velocity does not fluctuate, but the scalar does, is possible. Subsequently, long inlet channels were added to the T-junction and the particle image velocimetry (PIV) technique was used to verify the fully developed laminar flows and to investigate the flow regimes for different Reynolds numbers. It was found that the present setup can achieve inlet conditions with fully developed laminar flows when the Reynolds number is smaller than 1100. The setup was validated by repeating the flow regimes in previous studies. However, small temperature differences had a weak effect on flow regimes, which should be avoided in the next measurements. Overall, high-quality measuring of the small-scale mixing dynamics in the T-mixer is now within reach.

For active mixing with fluids of different densities, mixing usually causes optical measurement errors. In this thesis, a ray tracing simulation method is used in a three-dimensional flow to quantify the measurement errors of the flow velocity and flow acceleration for tracer-based velocimetry, i.e., particle tracking velocimetry (PTV). The flow field is from a direct numerical

simulation of single-phase turbulent mixing of two miscible fluids. The measurement errors increase with increasing the refractive index difference. The errors of both velocity and acceleration are attributed to the spatial and the spatio-temporal gradients of the refractive indices. Since PTV, PIV and PLIF share the same working principles based on geometric optics, the findings are also assumed to hold for the measurements of other techniques. The thermal effect in the T-mixer on the measurement errors is subsequently estimated and found to be negligible.

Finally, gas-liquid mixing is examined, in which a weakly soluble gas is transferred across the gas-liquid interface. This process is related to the climate balance and depends on surface waves and turbulence underneath the water in the ocean. Utilizing the refraction at the interface and optical displacements, a synthetic Schlieren method is developed to measure the surface topography. This method is implemented in experiments and allows high-accuracy measurements of free surface waves. This makes it feasible to implement simultaneous measurements of surface waves, mass transportation and turbulence under the water.

Acknowledgement

I am very grateful to many people for their contribution to and support of the work in this thesis.

My supervisor, Prof. Dr. Marc Avila, is both a mentor and a role model throughout my time at the University of Bremen. I would like to express my gratitude to him for continuous support, encouragement and scholastic advice as well as for profound insights into turbulence. Many thanks go to my co-supervisor, Dr. Duo Xu, for his guidance and the inspiring discussions as well as for his incredible patience with my PhD project and manuscripts. Their preciseness and high standards benefit me a lot and educate me to be a qualified researcher.

I would like to thank Prof. Dr. Andreas Fischer for his time and comments on my project related to the optical measurement error from the inhomogeneous refractive index field. And I also appreciate the time and help from Dr. Kerstin Avila and Bastian Bäuerlein for PIV experiments. Thanks for Dr. Daniel Feldmann helping me correct my German abstract. I am indebted to my lovely colleagues, past and present in the Fluid Simulation and Modeling group for bringing partnership and laughter to my experience. Thanks Changyong Li, Dr. Daniel Feldmann, Dr. Alberto Vela Martin, Carlos Plana Turmo, Daniel Moron, Stefan Gasow, Julia Tielke, Christoph Kühn, Feixiong Rao.

I really appreciate Katja Krömer, for her technical support and friendship throughout my graduate career. Thanks for the support from other technicians, Ronald Mairose, Peter Prengel, Holger Faust and Michael Peters. I am thankful to Maria Petrogiannis and Annette Leonhardt for their kind help with the paperwork.

Finally, I cordially acknowledge the China Scholarship Council (CSC) for the financial support for my doctoral research.

Contents

1	Introduction	1
1.1	Background	1
1.2	Passive and active scalar mixing	2
1.3	Turbulent mixing	4
1.4	Optical measurements of mixing processes	8
1.5	Gas-liquid mixing	10
1.6	Problems addressed in the thesis	13
1.7	Organization of the thesis	14
2	Measurements of small-scale liquid-liquid mixing in a T-mixer	15
2.1	Overview of mixing in T-mixers	15
2.2	PLIF observations in a T-junction	18
2.2.1	Experimental setup	18
2.2.2	PLIF principle	19
2.2.3	PLIF observations	22
2.3	Mixing in a T-mixer	24
2.3.1	Setup description	26
2.3.2	PIV measurements	35
2.3.3	Laminar inlet flows	36
2.3.4	Mixing patterns when $Re < 400$	38
2.3.5	Thermal convection	41
2.4	Summary and thoughts	44
3	Optical measurement errors in fluids flow with density differences	47
3.1	Optical distortion in different mixing fluids	47
3.2	Approach for an inhomogeneous refractive index field	51
3.2.1	Tracing light rays	52
3.2.2	Measurement arrangement	53
3.2.3	Determination of the measurement error	54

3.3	Setup of the numerical experiments	55
3.3.1	Simulated measurement object	55
3.3.2	Simulation of the mixing measurement	56
3.3.3	Verification and convergence	60
3.4	Results of the mixing measurement	62
3.4.1	Light deflection	62
3.4.2	Error of tracer position in images	64
3.4.3	Error of velocity measurement	68
3.4.4	Error of acceleration measurement	72
3.4.5	Optical errors in the T-mixer	73
3.5	Summary and recommendations	73
4	A measurement method for the gas-liquid mixing interface	77
4.1	Gas-liquid interface measurements	77
4.2	Methodology based on the refraction	79
4.3	Applications in air-water surface	85
4.3.1	Liquid ripples	85
4.3.2	Dam-break flows	89
4.4	Discussion of the method	95
4.4.1	Measurement uncertainty	95
4.4.2	Effect of camera vibration	97
4.4.3	Effect of resolution	99
4.4.4	Breakdown condition of the working principle	100
4.4.5	The effect of linearizing the governing equation	102
4.5	Summary and potential applications	104
5	Conclusion	107
5.1	Main results and summary	107
5.1.1	Mixing in the T-mixer	108
5.1.2	Optical errors in turbulent mixing	108
5.1.3	Surface wave measurements	109
5.2	Open questions and future studies	110
6	Appendix	113
6.1	Sources of measurement errors	113
	Bibliography	129

Introduction

1.1 Background

Mixing is a fundamental, multi-scale process, common in daily life and in nature, and is also ubiquitous in chemical and aerospace engineering. Mixing can be understood as an operation used to change an inhomogeneous system into a homogeneous system. The inhomogeneity can be one of concentration, phase, or temperature. Common examples contain mixing cream into coffee, smoke contaminant discharges in the atmosphere and chemical mixing in reactors, as shown in figure 1.1. Many processes in chemical or combustion engineering rely on the rapid mixing and the interface of fluid streams where reactants are dissolved. Thus, fluid mixing is a vital part of the chemical reactions. Similarly, mixing at the ocean surface is key for atmosphere-ocean interactions and for the distribution of heat and pollution gases in the atmosphere. Investigations of the ocean mixing play an important role in marine studies and in understanding the energy-mass exchange in the ocean interior. Overall, understanding mixing processes can not only improve the production efficiency in the chemical industry, but can also be beneficial to managing and decreasing pollution in the atmosphere and in the ocean.

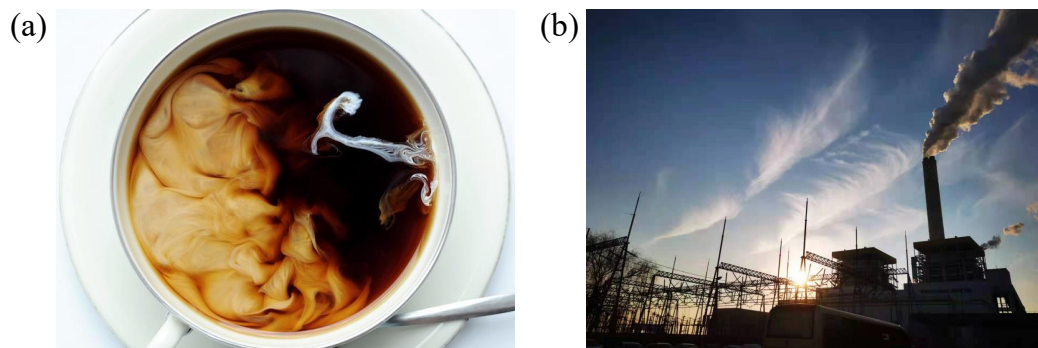


Fig. 1.1: Mixing pictures. (a) Mixing cream into coffee. (b) Smoke discharges in the atmosphere.

Mixing can be classified according to the various combinations between the gas, liquid, and solid phases, for example, gas-gas mixing, liquid-liquid mixing and gas-liquid mixing [126]. Gas-gas mixing happens e.g., in combustion engineering. Liquid-liquid mixing and gas-liquid mixing processes are commonly found in chemical engineering and oceanography. Liquid-liquid mixing is usually understood to be the mixing of two immiscible or miscible liquids. Liquids are considered to be immiscible if they cannot be mixed at molecular level, for example, oil and water. The immiscible mixing usually happens in two or more insoluble liquids present as separate phases. These phases are referred to as the dispersed (or drop) phase and the continuous phase [2]. By contrast, the miscible mixing of fluids refers to the property of various fluids that allows them to be mixed and form a single homogeneous phase. For example, water and ethanol are miscible in any proportions [126].

Similarly, for the gas-liquid mixing, a (poorly) soluble gas usually is contacted with a liquid to provide mass transfer, in which the absorption or desorption happens. For example, in chemical engineering, spray towers can be used to absorb gaseous reactants for flue gas desulfurization. Sulphur dioxide (SO_2) in a combustion gas is passed upward through an alkaline solution that usually contains calcium oxide. The SO_2 is absorbed into the liquid, which afterwards reacts to calcium sulfite and continues on to calcium sulfate [58, 39]. Sometimes the gas merely provides energy (via bubble wakes, bubble coalescence, or gas expansion) for mixing the liquid [126]. In oceanography, gas-liquid mixing is related to the mass/heat exchange at ocean-atmosphere interface. The primary driving mechanism that regulates the mass transfer rate across the gas-liquid interface is presumed to be near-interface turbulence [185]. The large interface area between gas and liquid generated by turbulence has good mass transfer performance [184].

1.2 Passive and active scalar mixing

Miscible fluid mixing is classified into two cases [44]. The simplest case of fluid mixing occurs between so-called passive scalars. Examples are dispersion and mixing of fluids with the same density or carrying non-reacting trace markers, such as pollutants [77], small temperature differences [71],

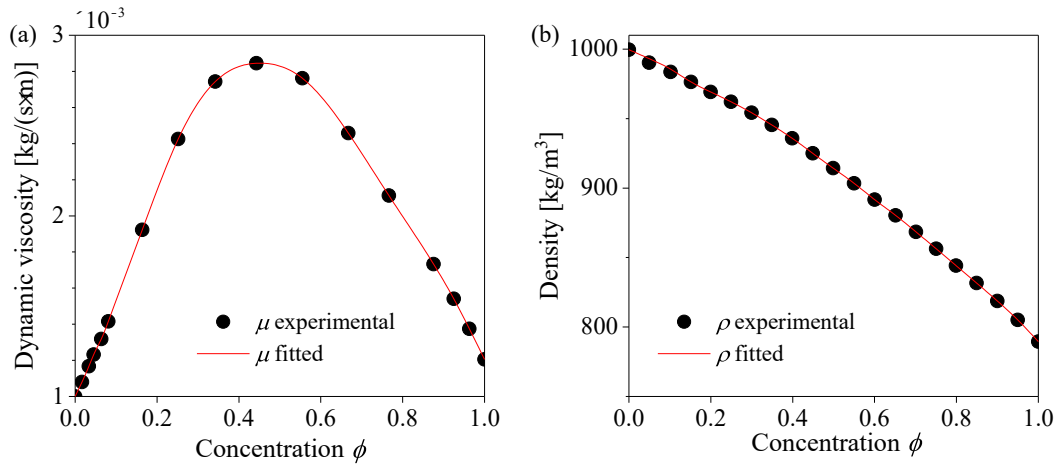


Fig. 1.2: Dynamic viscosity μ (a) and density ρ (b) as a function of the concentration ϕ (mass fraction), for a water-ethanol mixture. Here $\phi = 0$ and $\phi = 1$ correspond to the pure water and ethanol phases, respectively. The red solid lines indicate functions fitted to the experimental data (dots). The figure is reproduced from [142] and explicit fitting expression for $\mu(\phi)$ and $\rho(\phi)$ can be found in [46].

small-particle soot (smoke), and low-concentration dyes in a liquid (namely, the principle for laser-induced fluorescence), etc. The passive scalar mixing has no influence on the flow dynamics; dispersion and mixing are simply driven by the turbulent flow. Hence many studies focus on the turbulent mixing for high Reynolds number flows in canonical systems (e.g., jet flow [112, 111, 113] and channel flow [87]). By contrast, the active scalar mixing changes the fluid properties, e.g., density, viscosity and diffusion coefficient. As a consequence, momentum transport (governed by the Navier-Stokes equations) is modified, and the mixing process play a role in the fluid flow. Figure 1.2 shows the dependence of the measured viscosity and density on the normalized concentration for a water-ethanol mixture. The dynamic viscosity varies very strongly with the concentration. The density exhibits also a nonlinear trend with the concentration, albeit much less pronounced. During the active scalar mixing process, the dependence of viscosity and density on the concentration is a challenge for experimental and numeral studies. The Rayleigh-Taylor instability (e.g., [188, 191]), the mixing of the temperature and salinity fields in large-scale ocean currents (e.g., [172, 27, 174]) and turbulent premixed/non-premixed combustion [99] are examples of systems with the active-scalar mixing.

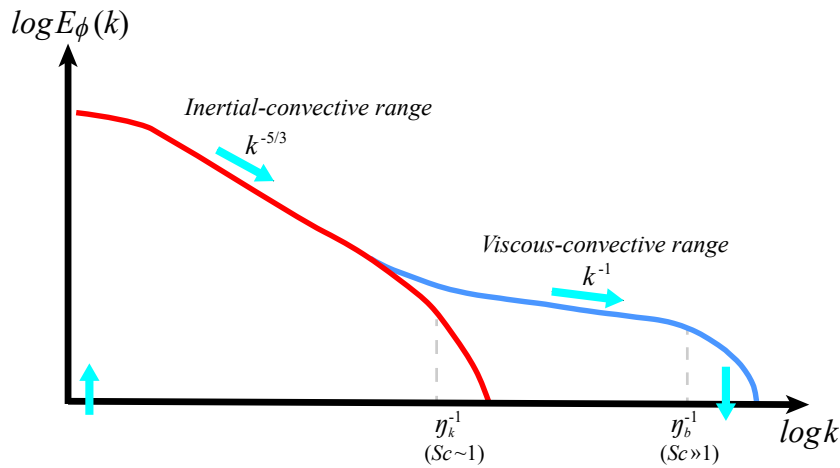


Fig. 1.3: Schematic of the scalar spectrum for $Sc \sim 1$ (red) and $Sc \gg 1$ (blue). The cyan arrows denotes the mean flux of scalar fluctuations. The figure is reproduced from [63].

1.3 Turbulent mixing

Mixing processes are critical to the successful manufacturing of many products. An example in chemical industry is polymer production, where the parameters describing mixing processes (e.g., mixing time, mass transfer coefficients and mass fractions) are considered to facilitate polymerization reactions, process efficiency and product quality [117]. In practice, mixing devices are commonly designed to produce highly turbulent flows to boost the mixing efficiency. Turbulent eddies occurring at multiple scales deform and drastically increase the interfacial area between the fluids, which enhances the overall mixing rate [44, 24]. Following the terminology of Eckart [48], turbulent mixing with the homogenization of fluids can be regarded as a three-stage process of entrainment, stirring, and diffusion [44]. For example, in the entrainment phase, there exists very large concentration gradients between regions, but the interfaces between two fluids have limited areas, so the average gradient is small, as in stratified fluids. Subsequently, the fluids are swirled and folded, and the average concentration gradients begin to increase. In the last stage, the gradients are smoothed and the fluid becomes homogeneous: diffusion completes the mixing. Diffusion is a molecular process, depending on the fluid diffusivities, whereas entrainment and stirring are kinematic processes that depend on the details (structures) of the fluid flow.

In turbulence, the largest eddies which entrain the fluids are constrained by the device geometry (e.g. the hydraulic diameter of a mixing channel). The smallest eddies are found at around the Kolmogorov scale $\eta_k = (\nu^3/\epsilon)^{1/4}$, where ϵ is the dissipation rate of turbulent kinetic energy and ν the kinematic viscosity of the fluid [130]. The turbulent kinetic energy cascade is characterized by an inertial subrange described with the $k^{-5/3}$ power law (k is a wavenumber) and by a viscous subrange at high Reynolds numbers [137, 92, 91]. Below the Kolmogorov scale, momentum transport is diffusive and controlled by the viscosity, and the turbulent kinetic energy is dissipated into heat [130, 40].

Analogously, the concentration of species (here ϕ denotes a scalar field) exhibits fluctuations until around the smallest mixing length scales. The mixing process also spans the full spectrum of space-time scales of the flow and depends on the Reynolds number and on the Schmidt number $Sc = \nu/D$ (analogous to the Prandtl number for the temperature), i.e. the ratio between the kinematic viscosity ν and the molecular (or thermal) diffusivity D . Many differences between the moderately diffusive ($Sc \lesssim 1$) and weakly diffusive ($Sc \gg 1$) regimes are known [32, 10, 176]. In particular, when $Sc \lesssim 1$ (i.e. $\nu \lesssim D$), the smallest scale is known as the Corrsin-Obukhov scale η_{co} with $\eta_{co}/\eta_k \sim Sc^{-3/4}$. And in the so-called inertial-convective range at a high Reynolds number, the spectrum of scalar fluctuations is expected to be followed with $k^{-5/3}$ power [32] (see red solid line in figure 1.3), in which the fluid viscosity and the scalar diffusivity are both important. If $Sc \gg 1$ (i.e. $\nu \gg D$), as in liquids, the smallest scale is known as the Batchelor scale [10, 93], $\eta_b = (\nu D^2/\epsilon)^{1/4}$, $\eta_b/\eta_k \sim Sc^{-1/2}$. There is a k^{-1} spectrum, called the viscous-convective range within which diffusion is not important but viscosity prevails, as shown in figure 1.3 with blue solid line. Below the Batchelor scale, molecular mass diffusion acts and the mixing process is completed. However, past evidence for the -1 scaling law for the power spectrum has been ambiguous, because resolving the Batchelor scale is a great challenge in both experiments and simulations. In liquids, with $D \sim 10^{-9}$ m²/s and $\nu \sim 10^{-5}$ m²/s ($Sc = \mathcal{O}(10^3)$), the Batchelor scale is approximately 30 times smaller than the Kolmogorov scale. In the viscous-convective range, the velocity field does not fluctuate, but the scalar field does, which poses an enormous challenge to simulations and experiments

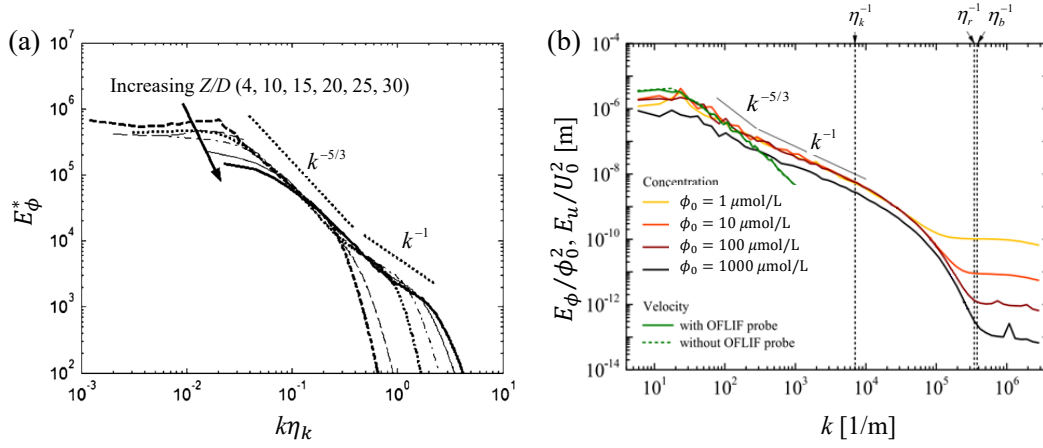


Fig. 1.4: The measured spectra in the literature (reproduced from [157] and [78], respectively). (a) Spectra of scalar fluctuation along the jet axis for $Z/D = 4$ to $Z/D = 30$. Here D is the diameter of jet nozzle and E_ϕ^* means the dimensionless scalar spectra for simplicity, see [157] for details. (b) Spectra of scalar fluctuation for different initial concentration at the jet exit ϕ_0 and spectra of streamwise velocity fluctuation. The scalar and velocity spectra are normalized by ϕ_0^2 and U_0^2 (jet exit bulk velocity). η_r^{-1} denotes the wave number corresponding to the spatial resolution of their OFLIF technique, see [78] for details.

alike. In particular, for $Sc \sim 10^3$, resolving the Batchelor scale requires 30 times finer spatial resolution (in each direction) than for the Kolmogorov scale. For a direct numerical simulation (DNS), this requirement implies that the spatial discretization of the scalar transport equation is four orders of magnitude larger than that for resolving the Navier-Stokes equations [44].

Similarly, when carrying out experiments on turbulent mixing, it is of importance to evaluate the resolution of the measuring technique and estimate whether it can resolve fluctuations above and under the Batchelor scale. To achieve high resolution measurements, many previous studies obtained the time series of the concentration fluctuation with high frequency and converted the measurement into space by exploiting Taylor's hypothesis. Gibson and Schwarz [60] measured the passive scalar in grid turbulence and reported the k^{-1} spectral prediction based on Taylor's hypothesis. Grant et al. [66] in the ocean and tidal channel reported that the temperature fluctuations can be fitted by the k^{-1} spectral prediction. In a turbulent propane jet, Talbot et al. [157] used hot-wire anemometry and Rayleigh light scattering to simultaneously measure the velocity and concentration field, in which the scalar spectra exhibit k^{-1} scaling law with the Taylor's frozen hypothe-

sis, see figure 1.4(a). Similarly, based on Taylor's hypothesis, Iwano et al. [78] used optical fiber laser-induced fluorescence probe (OFLIF) with a 2.8 μm spatial resolution to investigate the power spectrum in a high Schmidt number turbulent jet, in which the spectrum almost follows the k^{-1} scaling but has a small bump, see figure 1.4(b). Meanwhile, similar results were also reported in other measurements with turbulent jets [112, 111, 113]. Recently, Clay [30] obtained evidence that the -1 power region does exist and becomes better defined with increasing Sc through the DNS. Despite this great progress achieved with the DNS of homogenous, isotropic turbulence, it is necessary to revisit this scaling through the perspective of experiments without Taylor's frozen hypothesis.

The passive scalar transported by turbulence exhibits intermittency, and its strong fluctuations are in general related to practical problems such as mixing in chemical reactions and localized high concentration of air pollutants [177]. The generic ramp-cliff structure of passive scalar is recognized to be related to the intermittency, reflected in the scaling anomaly of high-order structure functions of scalar fluctuations [79, 152, 20]. As expected, the ramp-cliff structure contains the sharp fronts of larger scalar gradients (cliffs) and regions of weaker gradients (ramps). Recent DNS studies [20, 21] indicate that the scaling exponents of the scalar structure functions in the inertial-convective range appear to saturate concerning the moment order. And a simple model for the ramp-cliff structures is developed and shown to characterize the scalar derivative statistics very well [21]. It additionally suggests a possible modification of the Batchelor scale as the relevant smallest scale in the scalar field. Overall, the experimental evidence for these existing phenomenology of scalar turbulence needs further investigations. This would also be instructive for understanding active scalars at large Sc .

1.4 Optical measurements of mixing processes

When fluids of different densities, such as water and ethanol are mixed, optical experimental investigations are difficult to implement because of

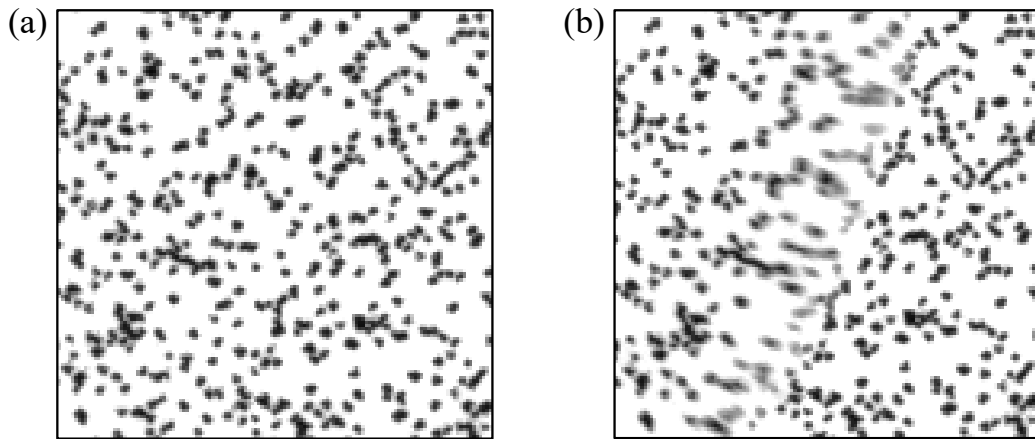


Fig. 1.5: (a) Undisturbed background pattern, recorded as reference. (b) The same background pattern behind a water-ethanol mixing process. Image distortion and displacements can be observed due to the different refractive indexes of water and ethanol. Note that for clear demonstration, the images are tuned through brightness and contrast.

the optical distortion. Different fluids have different refractive index, and the inhomogeneous refractive index field poses a substantial impediment to performing optical velocity and concentration measurements, for example, particle tracking velocimetry (PTV) [124], particle image velocimetry (PIV) [51, 50] and planar laser-induced fluorescence (PLIF) [123], etc, which share the principle of geometrical optics. The measurement images are blurred because of the optical distortion (e.g., figure 1.5), which leads to the errors in the experimental measurements of velocity and concentration [155, 86, 170]. Oljaca and Glezer [123] observed this optical distortion in fluorescence images of scalar mixing from two water streams with different temperatures. Similarly, Dimotakis et al. [45] experimentally reported optical distortions of scalar-field images created by shear layers with high Reynolds number, in which a high-speed helium or nitrogen flow (with low refractive index) mixed with a lower-speed ethylene flow (with high refractive index). Kim et al. [86] carried out a PIV experiment with two miscible fluids with different refractive indices in a Y-shaped micro mixer and they found that a discrepancy in the velocity profile was observed between the experimental and numerical results, especially close to the two-fluid interface, which was attributed to the image-blurring caused by a strong gradient of the refractive index. Thus, for studying active scalar mixing at a fundamental level, the working fluids must be selected carefully to ensure the refractive indices of the substances are very nearly equal and there are no chemical reactions

among them, e.g., helium and air [18]. However, these well-chosen fluids only reveal a part of the nature of the mixing process and also are far away from practical applications.

Assessing the optical distortion induced by an inhomogeneous refractive index field may be a viable approach to correct the errors in these optical techniques. Previous studies have attempted to quantify and correct the optical distortion in a planar PIV for the shock waves and combustion, but without consideration of the effects of spatio-temporal changing refractive index field [51, 133, 187]. Raffel and Kost [132] introduced a formula to quantify the displacements of the imaged tracers seen across the shock wave. Elsinga et al. [51] studied aero-optical errors of planar PIV measurements and applied the background oriented schlieren technique (BOS) to correct the optical error in PIV results. For the approximately two-dimensional shock wave attached to a conical-head vehicle, Guo et al. [69] simulated light rays deflection over discrete grids following Snell's law. In turbulent flames, Stella et al. [155] realized that the measurements with the PIV technique were affected by the inhomogeneous refractive index field induced by temperature differences. They theoretically estimated the deflection of light propagation of particles while crossing the flame front but without consideration of the spatio-temporal temperature changes inside the flame. Thus, it is worthwhile to investigate and evaluate the effects of the varying refraction index field during the mixing process for the common optical techniques, at least in the scope of experimental fluid dynamics.

1.5 Gas-liquid mixing

The experimental characterization of the mixing process of two-phase immiscible fluids is equally challenging, because of the refractive index difference between two fluids. Gas-liquid mixing is a typical case, which is ubiquitous in the air-water interface in the ocean. Heat and gas are constantly exchanged with the atmosphere. More importantly, the exchange between the ocean and the atmosphere is related to the climate balance and environmental process. For example, the wind energy from the atmosphere is transferred to the ocean surface, driving the wave and circulation (e.g., figure 1.6), trans-

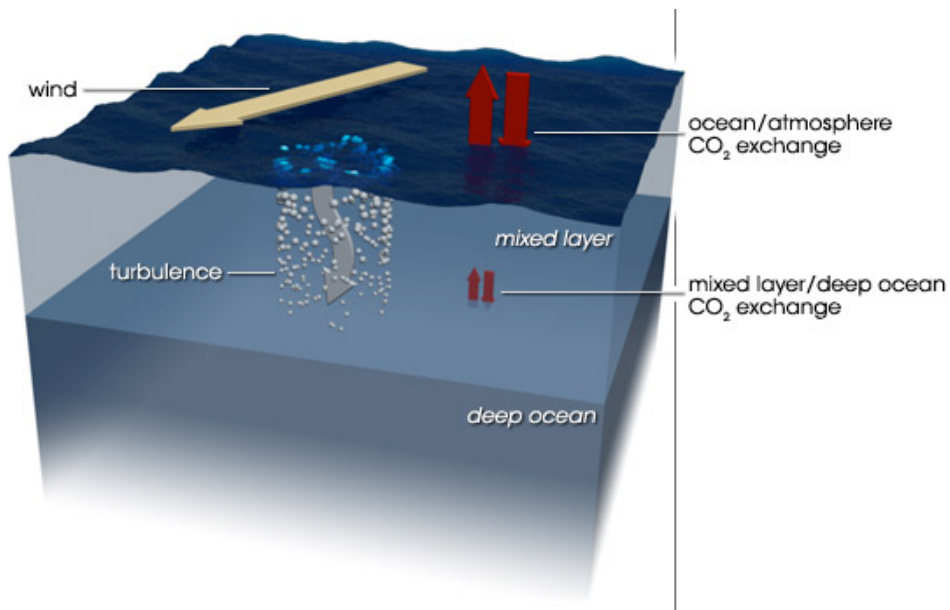


Fig. 1.6: An example of CO₂ exchange driven by a wind at the ocean–atmosphere surface. The picture is reproduced from [138].

porting oxygen and achieving the reaeration of rivers, lakes and oceans. In turn, the energy and carbon dioxide from the ocean (e.g., by internal wave) are fed back to the atmosphere through the surface, affecting atmospheric circulation, weather and even climate [94]. Besides, air-water exchange at water surfaces is one of the paths for transport of various pollutants, e.g., sulfur oxides, methane, freons, and many organic chemicals used in pesticides, herbicides and detergents into the lake, marine and atmosphere environment [110]. This air-water exchange process is governed by interaction among molecular diffusion, turbulent mixing and waves near the interface as well as the solubility of the exchange materials [109, 185, 127].

Additionally, gas-liquid exchange plays an important role in many engineering processes as well, such as condensers, evaporators, desalination systems and the purification of toxic gases from exhaust gases and chemical reactors, etc [80, 106, 42]. The falling liquid film with dynamic free surfaces is a typical example, which is utilized for the efficient heat and mass exchange in steam condensers and evaporators [85]. In particular respect to the miscible condensation process, the heat-transfer coefficient inside the condenser is mainly dependent on the mass fraction of liquid and vapour, on which the air-liquid transfer has crucial effects [156, 131]. Thus, investigations and

understanding of the gas-liquid exchange at the surface can further improve and optimize these processes in engineering.

The scalar transfer and mixing across the air-water interface works on both sides [175]. In oceanography, the research mainly focuses on the transfer of momentum and sensible and latent heat on the air side [80, 109]. In contrast, on the water side, most research interest focuses on the gas transfer process, because of the slow transport of common gases (such as O_2 , CH_4 , CO , CO_2 , NO) across the interface and their low solubility in water [163]. The primary physical factor that influences the exchange of these gases is wind speed. From low to moderate wind speeds (nominally below 10 m/s [185, 59]), the air-water interfacial shear due to the wind forcing stirs the water near the interface and the diffusive gas exchange is dominated. At moderate to high wind speeds, the oceanic bubble-mediated exchange produced by breaking waves plays an important role [101, 185, 59]. Thus, at the low wind speed, neglecting the effects of bubbles, the air-water exchange can be simplified as a transport problem in the direction normal to the interface. The mass flux \bar{F} across the mass boundary layer maintained by pure molecular diffusion can be modeled as [80, 72, 175]

$$\bar{F} = \bar{k}(C_w - sC_a), \quad (1.1)$$

where s is the solubility coefficient, C_w and C_a are the gas concentrations in the bulk water and the atmosphere, respectively, and \bar{k} is the gas transfer velocity, which depends on the gas diffusivity in water and the thickness of mass boundary layer (typically $\mathcal{O}(100 \mu\text{m})$ [80]). This typical thickness is smaller than the Kolmogorov scale of the liquid flow [73] and changes in time and space because of the water turbulence, increasing the simulation costs and complicating understanding mechanisms of gas transfer in the interface. Most of previous studies make efforts to establish empirical and conceptual models to predict the gas transfer velocity [100, 37, 8, 159] and also investigate the gas transfer velocity by simulations and experiments [49, 164, 72, 163, 73, 74]. It has been evidently reported that the surface waves (e.g., wave slopes) have effects on the turbulent mass transfer across the air-water interface [9, 13, 185, 95]. Both short/long wind-driven waves can enhance the mass transfer, but the mechanisms for the enhancement are

less well known in detail [80]. Thus, investigating the topography structures of free surface waves is important to understanding the scalar transfer and mixing across the air-water surface.

In summary, a better understanding of the mixing process would have numerous applications in nature and engineering. However, experimental measurements are challenging for the small-scale fluctuations in turbulence because of spatio-temporally varying refractive indexes in the mixing cases of fluids with different densities. These challenges are investigated in this thesis in detail, and studies are provided.

1.6 Problems addressed in the thesis

This thesis focuses on the miscible liquid-liquid and gas-liquid mixing. Firstly, this research is aimed at measuring the passive scalar mixing characteristics in T-mixer flows at moderate Reynolds numbers. In the investigation, the mixing is considered with water and water (with Rhodamine 6G). The optical distortion caused by thermal effects is considered. Subsequently, the optical distortion for the measurement errors is estimated through a turbulent mixing process where fluids mix with a spatio-temporally varying refractive index field. It is intended to show that the present T-mixer setup and optical techniques are useful and reliable tools to investigate the dynamics of turbulence small-scale mixing.

At the same time, due to the delay with T-mixer mixing experiments caused by the pandemic and twice laser repairs (including shipment to the United States), a surface wave measurement method was developed for gas-liquid mixing. Here, the gas is considered to be weakly soluble. The method is based on refraction and optical displacements, which is promising for understanding the mixing and mass/heat transfer at the air-water mixing interface.

The main achievements of this thesis can be summarized as follows:

- **Small-scale liquid-liquid mixing in a T-mixer:** A PLIF technique with high resolution is employed in proof-of-concept experiments, which indicates that measuring the full viscous-convective range in the present setup is possible. In addition, the PIV technique is used to examine the fully developed laminar flows and measure the flow characteristics. The latter is cross-validated with DNS results through Strouhal numbers. The design of the setup can be adjusted and improved through this validation of the flow measurements. The optical distortion is realized through the thermal effect. This setup will be used for the investigation of the spatio-temporal dynamics in the viscous-convective range.
- **Optical distortion induced by a miscible two-fluids mixing:** Optical measurement errors and fidelity of optical techniques (e.g., PIV/PTV and PLIF) in the T-mixer liquid-liquid mixing are expected, but they are difficult to be studied in experiments. To estimate the optical errors caused by a mixing process or heat transfer with an inhomogeneous refractive index field, ray tracing simulation is employed in a single-phase turbulent miscible mixing process to evaluate the measurement errors.
- **A promising method to measure an air-water interface:** According to the refraction and optical displacements due to the gas-liquid interface, a single-camera synthetic Schlieren method is developed to resolve the topography and flow structures of the free surface. The accuracy of the method is also estimated. This method can be used in further investigations of the mixing and turbulence at the air-water interface.

1.7 Organization of the thesis

Chapter 2 covers the experimental work (PIV and PLIF) in the T-mixer setup. It contains the design of the experimental setup, experimental techniques, results and discussion from the experiments.

Chapter 3 introduces the ray tracing method and mainly discusses the optical error for the PTV technique with a spatio-temporally varying refractive index field.

Chapter 4 contains the principle and accuracy for the single-camera synthetic Schlieren method and experimental applications.

Chapter 5 is a summary of the thesis with an outlook.

Measurements of small-scale liquid-liquid mixing in a T-mixer

2.1 Overview of mixing in T-mixers

Miscible liquid-liquid mixing is a fundamental process in engineering applications (e.g. in chemical and aerospace engineering). In chemical (process) engineering, micromixing devices are used to study mixing processes and their impact on chemical reactions. Among a variety of canonical mixers, the T-shaped mixing geometry has been widely used because it is easy to fabricate and exhibits good mixing efficiency. Thus, the T-mixer has attracted intensive investigations on understanding the physics of the mixing process, characterizing the mixing performance, and quantifying the quality of the mixing outcomes [23].

A typical T-mixer consists of two branches (inlets) of square cross-section (H , height), and an outlet (main mixing channel) of the rectangular cross-section with dimensions of $2H \times H$ (width \times height), as shown in figure 2.1(a). The Reynolds number plays an important role for the mixing flow in a T-mixer and is usually defined as $Re = U_0 H / \nu$. Here U_0 is the bulk velocity of the mixing channel and ν is the kinematic viscosity of the fluid. With increasing Reynolds number, different flow regimes have been broadly identified in previous numerical and experimental studies: the steady symmetric flow, the engulfment flows (including steady asymmetric flow and periodic asymmetric flow), the unsteady symmetric flow, and chaotic flows [23, 189, 160, 55, 56], see figure 2.2. When the Reynolds number is small ($Re \lesssim 105$), the steady and symmetric flow is dominant. Two parallel streams of fluid form and flow from the inlet channels to the mixing channel [142, 160, 161]. In this regime, mixing occurs only by diffusion. As the Reynolds number increases, the symmetric flow state becomes unstable and is replaced by the called engulfment flow state, which has been observed with PLIF [75, 161] and in

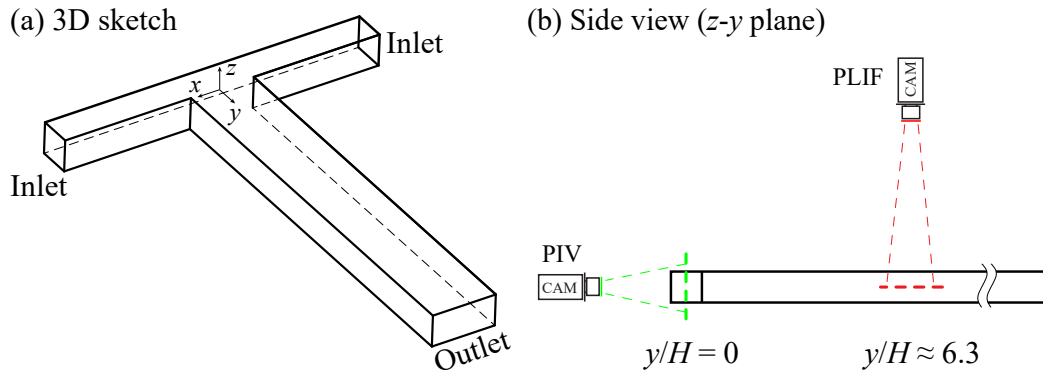


Fig. 2.1: (a) A sketch of a T-junction section and coordinates. (b) The green dashed line means the position where PIV measurements are taken and the camera view is from the back of the T-mixer looking down the outlet channel. The red dashed line denotes the position where PLIF measurements are taken and the camera is placed upon the junction. The coordinate origin is the centerpoint of the junction.

flow simulations [142]. To identify the critical Re at which the transition from symmetric flow to engulfment flow occurs, Soleymani et al. [150] provided an expression based on a numerical study, and having the mixing channel length and aspect ratio of the T-mixers as parameters. Their expression was found to be consistent with experimental data for different T-mixers in the literature. Furthermore, through simulation and experiments, Poole et al. [129] and Cherlo and Pushpavanam [29] further confirmed this expression for predicting the critical Reynolds, but they found that the expression failed when the height of the T-mixer was greater than the width.

In the engulfment flow, the symmetric flow structure is broken due to the high flow momentum of two inlet channels, and the shear layer in the T-junction starts to engulf both flow streams. Two vortexes are observed obviously and the flow pattern has central symmetry. The resulting enhancement of the mixing process has been discussed in several studies [189, 160, 55, 56]. At low Reynolds number, the engulfment flow is steady and later becomes unsteady (periodic) and chaotic [142]. Transition Reynolds numbers from steady flow to unsteady engulfment flow were also reported in the literature, e.g., $Re \approx 142$ [160, 161, 53], or $Re = 180-195$ [189]. Fani et al. [55, 56] analysed the instability mechanism and precisely determined this critical Reynolds number ($Re \approx 175$) through direct numerical simulation (DNS) for aspect ratio equal to 1. The difference of these critical Reynolds numbers mentioned above might come from different aspect ratios of the setups.

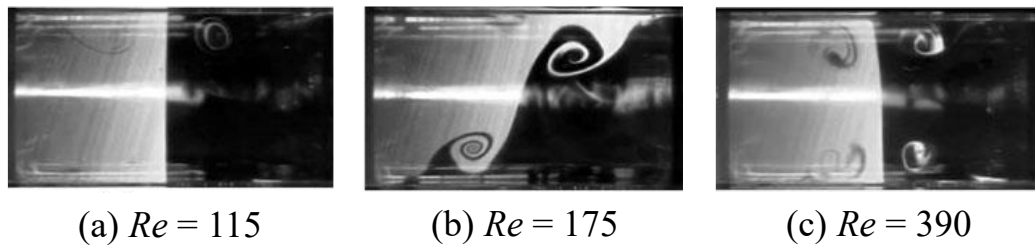


Fig. 2.2: The mixing regimes with different Re in the T-junction ($y/H = 0$ plane): (a) Steady symmetric flow, (b) Engulfment flow, and (c) Unsteady symmetric flow. The pictures are reproduced from the experimental results [160].

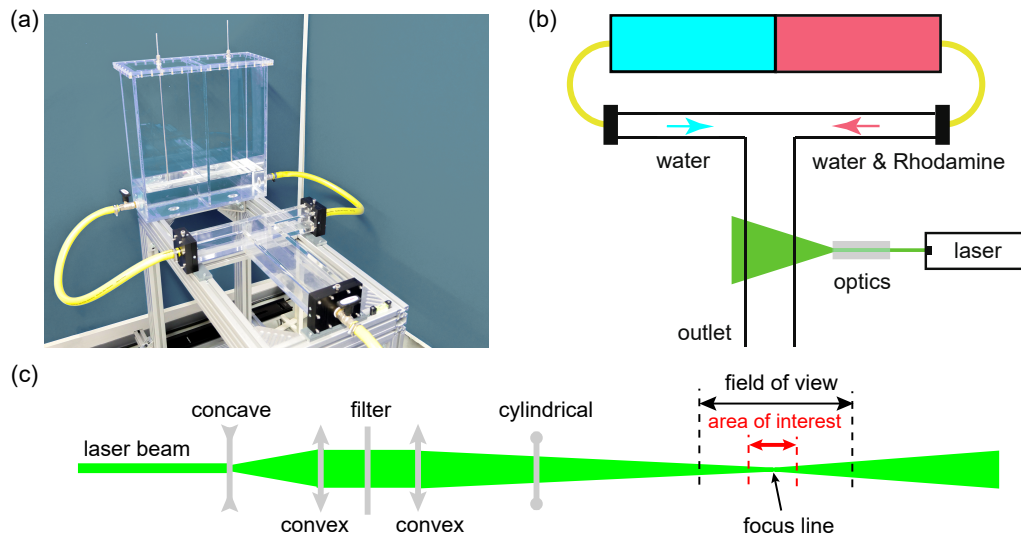


Fig. 2.3: T-mixer test device consisting of two equally sized tanks (red and cyan) feeding two inlets which meet at a T-junction, where the incoming fluid streams make a 90 degree turn and then mix along the main channel. In the main (mixing) channel PLIF measurements are made. (a) picture of the setup (b) sketch of the top view. (c) The optical configuration viewed along the laser sheet.

With further increasing Reynolds numbers ($\gtrsim 320$), the flow begins to regain symmetry but is unsteady. First it is periodic, and later the flow pattern exhibits quasi-periodic behaviors, in which oscillatory stagnation point behavior is unpredictably interrupted by asymmetrical breaks [160]. Periodic breaks from symmetry that occur in this regime are more frequent with increasing Re , as the momentum field of the inlet flow in the T-mixer becomes increasingly more energetic [160]. Subsequently, the flow regime becomes chaotic with the increase of the Reynolds number. When the Reynolds number is beyond 650, the flow in the mixing channel becomes eventually turbulent [143]. However, only a few studies [114, 143] focused on the flow and mixing dynamics at high Reynolds numbers (> 500) for a T-mixer, especially through experiments.

For accurate, high-resolution measurements (PIV and PLIF) at moderate to high Reynolds numbers, a T-junction was designed in this thesis for mixing experiments. It has a height of 40 millimeters (namely $H = 40$ mm), which is much larger than the dimensions of typically used micro-scale T-mixers with the same geometry. The PLIF and PIV techniques were applied respectively, as shown in figure 2.1(b). The principle, as well as experimental arrangements and results of these two techniques are demonstrated below.

2.2 PLIF observations in a T-junction

A PLIF technique with high resolution was employed to quantify the mixing process. The aim of this part is to implement a PLIF technique in the T-junction through preliminary, proof-of-concept experiments.

2.2.1 Experimental setup

As shown in figure 2.3(a), the test unit consists of a T-junction, with two 200 mm long square inlets ($H \times H$) and a 400 mm long rectangular outlet ($2H \times H$, width \times height). The T-junction has a height of 40 mm. Note that the inner corners in the junction region are associated with small radii of curvature, measured smaller than 1 mm, which has negligible effects on

flow behaviour [161]. Each inlet is connected to a tank via a half-stiffness tube. One tank is filled with water and the other is filled with a uniform mixture of water and fluorescent dye (Rhodamine 6G) to the same height level (see figure 2.3b). The fluid streams are driven by gravity and flow into the T-junction unit at approximately the same flow rate. By adjusting the fill level (kept equal in both tanks), the flow rate (Reynolds number) can be adjusted. Because of the geometry, The flow rates at the two inlets are kept equal, and the average speed (and hence the Reynolds number) is the same at the inlets and main channel. A pulsed Nd: YAG laser system of 527 nm wavelength (DM50-527 Photonics) with a group of optics was used to generate a laser sheet to illuminate the flow and the light focus line was placed in the field-of-view. The peak absorption and emission wavelengths of Rhodamine 6G are around 530 and 565 nm [139], respectively. The respective Schmidt number is approximately 600 [122]. A 12-bit CMOS camera (Phantom VEO 640L, 2560×1600 pixel²) was placed about one meter above the laser sheet to record the PLIF images. PLIF technique was applied to measure the concentration at a test unit with a given location ($y/H \approx 6.3$) in the middle height of the outlet channel, see figure 2.1(b).

2.2.2 PLIF principle

The grayscale value of every location in the PLIF image $g(\mathbf{x}, t)$ is related to the local dye concentration $\phi(\mathbf{x}, t)$ and local laser intensity $I(\mathbf{x}, t)$, i.e.,

$$g(\mathbf{x}, t) = \Gamma \cdot I(\mathbf{x}, t) \cdot \phi(\mathbf{x}, t) + g_b(\mathbf{x}), \quad (2.1)$$

where Γ quantifies the system optical collection efficiency (depending on the camera sensor) as well as the effective quantum yield of fluorescence dye [181, 34], and $g_b(\mathbf{x})$ denotes the background noise. Furthermore, in the dyed solution, because of the absorption along the laser light propagation path, the local laser intensity $I(\mathbf{x}, t)$ is determined by the initial local laser intensity $I_0(\mathbf{x}, t)$, the local dye concentration along the laser propagation $\phi(s, t)$, an absorption constant coefficient ϵ and the laser propagation path S in the experiment according to the Bouguer-Lambert-Beer Law. This leads to

$$g(\mathbf{x}, t) = \Gamma \cdot I_0(\mathbf{x}) \cdot \exp\left(-\int_S \epsilon \phi(s, t) ds\right) \cdot \phi(\mathbf{x}, t) + g_b(\mathbf{x}). \quad (2.2)$$

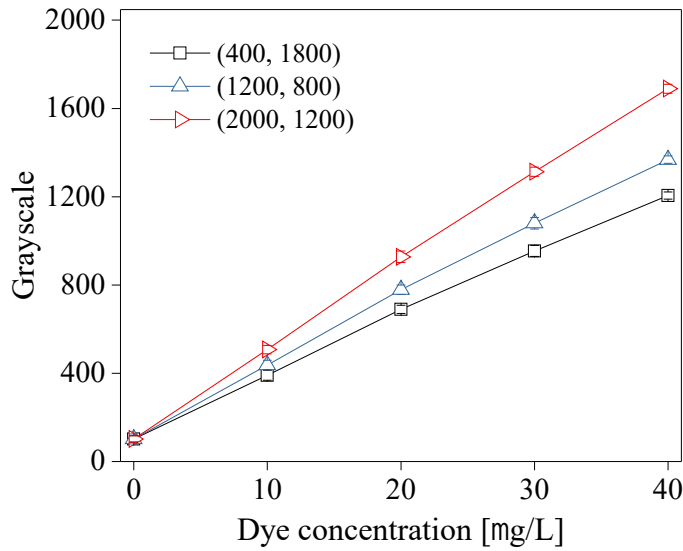


Fig. 2.4: The example of the PLIF calibration linear curves at three characteristic pixel locations in the PLIF image. The averaged grayscale values are computed using 100 snapshots at each of the five calibration concentration levels. Symbols show the ensemble average, and the error bars show the standard deviation values. The figure is reproduced from [181].

Equation 2.2 features a non-linear relationship between fluorescence intensity and concentration. However, for sufficiently low dye concentration, the laser attenuation can be negligible, i.e. $\int_S \epsilon \phi(s, t) ds \ll 1$, allowing the equation 2.2 to be linearized as [25, 33]

$$g(\mathbf{x}, t) \approx \Gamma \cdot I_0(\mathbf{x}) \cdot \phi(\mathbf{x}, t) + g_b(\mathbf{x}). \quad (2.3)$$

Thus, the grayscale information of the PLIF images can be converted to concentration of dye solution with equation 2.3, leading to

$$\phi(\mathbf{x}, t) = \frac{g(\mathbf{x}, t) - g_b(\mathbf{x})}{\Gamma \cdot I_0(\mathbf{x})}. \quad (2.4)$$

The coefficient $\Gamma \cdot I_0(\mathbf{x})$ can be obtained through a calibration procedure with equation 2.3. The averaged grayscale values at every pixel location, computed using many snapshots at each of the different uniform concentration levels, are curve fitted to establish a linear relationship of concentration $\phi(\mathbf{x})$, see figure 2.4.

In chemical engineering, the hydraulic diameter of T-mixer devices is usually $H \lesssim 1$ mm and spatio-temporal measurements of the concentration can

only be performed with μ LIF [75]. For a T-mixer at moderate Reynolds number, e.g., $Re = 650$, the smallest mixing scale (Batchelor scale η_b) is about $6.25 \times 10^{-4}H$ ($0.625 \mu\text{m}$ with $H = 1 \text{ mm}$), as estimated from numerical simulations [143]. Such a small scale is nearly impossible to be measured by common PLIF and μ LIF technique along the depth direction of the laser sheet. To overcome this experimental challenge, a T-junction with $H = 40 \text{ mm}$ was built (see figure 2.3a), in which the Batchelor scale is about $25 \mu\text{m}$ at $Re = 650$. Since the out-of-plane resolution of the PLIF system is determined by the thickness of the laser sheet [34], a high-resolution PLIF technique was used in this thesis (see figure 2.3c). Both improvement make the accurate measurement feasible for the smallest mixing scales.

To achieve a smaller laser-sheet thickness (for high resolution out-of-plane) at the measurement location, the optics configuration shown in figure 2.3(c) was implemented. The diameter of the laser beam exited from the pulsed laser is expanded to $\sim 16 \text{ mm}$ through a combination of two spherical lenses before being focused by a 300 mm focal length plano-convex lens. A reverse apodizing filter (NDYR20B, Thorlabs) was employed to produce a sharp Gaussian profile and further decrease the thickness of the laser sheet. These components served to focus the laser beam down to a waist diameter of approximately $20 \mu\text{m}$ ($\lesssim \eta_b$ for $Re \leq 650$), and the area-of-interest (named Rayleigh length) corresponding to this configuration was about 2 mm [136, 34]. Then, this laser beam is expanded by the cylindrical lens to form a horizontal laser sheet for the flow. The pixel-wise resolution in plane can reach down to the Batchelor scales through a camera lens with 50 mm focal length.

2.2.3 PLIF observations

A sample of the PLIF measurements at $Re \approx 440$ is shown in figure 2.5(a), and three profiles of the dye concentration ϕ are shown in (b). More PLIF snapshots are displayed in figure 2.8. For these measurements, the camera resolution was set to about $51 \mu\text{m}$ per pixel, which was sufficient to resolve the smallest scalar scales in this example and allowed at the same time

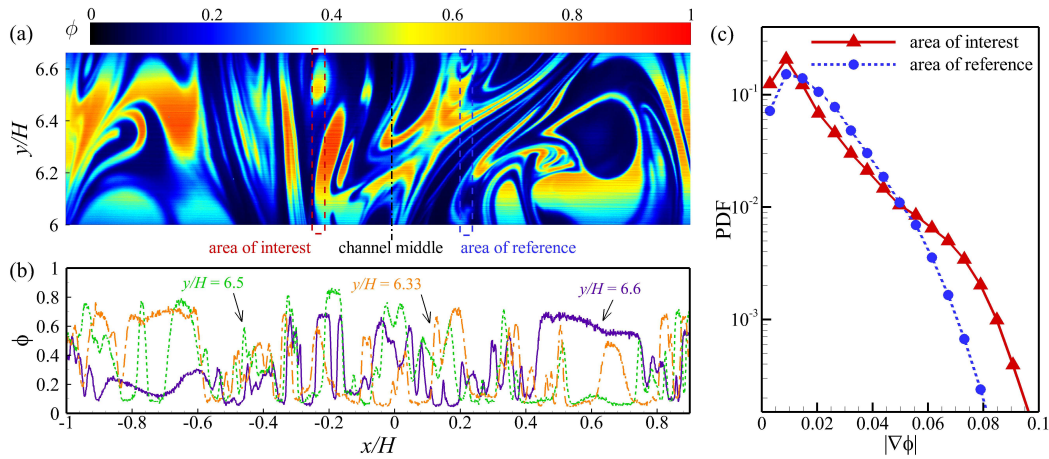


Fig. 2.5: (a) Colormap of a PLIF measurement, where the concentration ϕ of fluorescent dye is normalized by the maximum. (b) Profiles of ϕ at three selected positions in (a). (c) Probability density function (PDF) of $|\nabla\phi|$, where the red and the blue lines correspond to the statistics from the area-of-interest and the area-of-reference (marked in a), which have the same area (40 by 600 pixels) and are at the same distance from the channel mid-plane. Note that 48,000,000 data points ($40 \times 600 \times 2000$; pixels \times snapshots) were collected to obtain sufficiently converged statistics.

measuring nearly the whole cross section (albeit at lower resolution outside the area of interest).

The flow is spatio-temporally chaotic and the sharper gradients of dye concentration $\nabla\phi$ separate regions of unmixed fluids. The measurements of dye concentration at the area of interest (in which it is expected to resolve the viscous-convective range) and at the area of reference are compared. Both areas were placed at the same distance from the channel middle, left and right respectively. The area of interest is highlighted with red dashed lines and the area of reference with blue dashed lines in figure 2.5(a). With sufficient number of samples, the flow statistics should be the same in the two areas, because of the time-averaged left-right symmetry of the flow state. For the comparison, the spatial gradients of the dye concentration $\nabla\phi$ with a central-difference scheme are computed. The probability density function (PDF) of $|\nabla\phi|$ is shown in figure 2.5(c), where sharper interfaces, indicated by larger $|\nabla\phi|$, are evident in the area-of-interest. The laser sheet in the area-of-interest is thin, but in the area of reference, the laser sheet is thicker and the fluid interfaces appear more diffuse. The close-up of the concentration profiles at the area of interest and the area of reference are shown in figure 2.6. Besides,

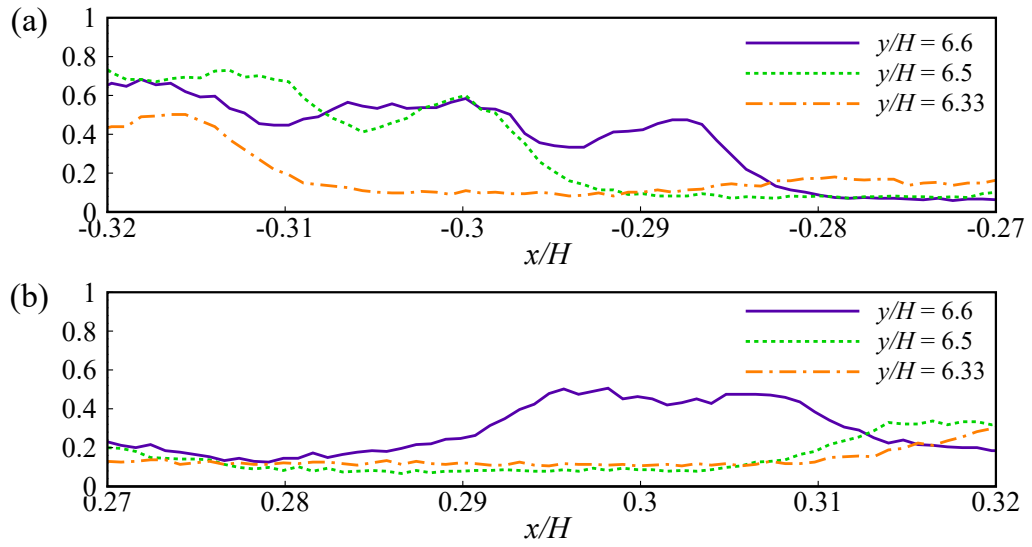


Fig. 2.6: Close-up of the concentration profiles of figure 2.5(b) at the area of interest (a) and the area of reference (b).

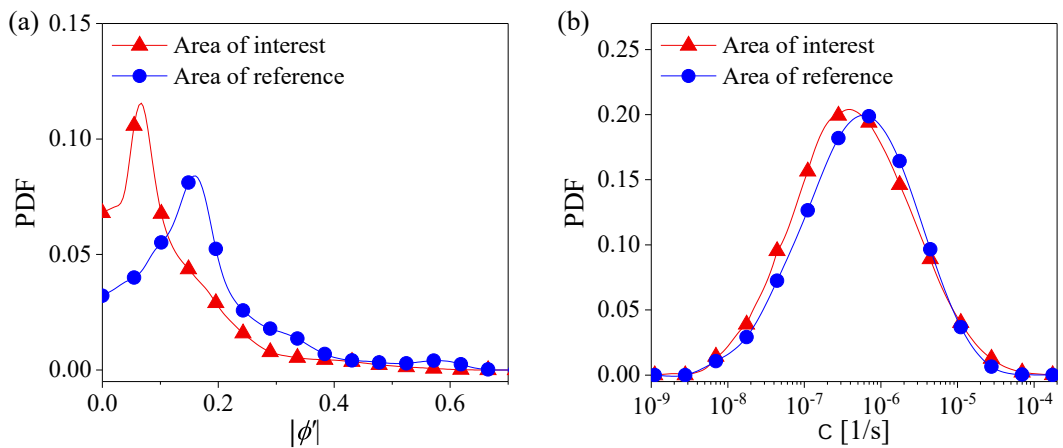


Fig. 2.7: PDF of the scalar fluctuation, ϕ' (a), and scalar dissipation rate, χ (b), for the area of interest and the area of reference, respectively.

figure 2.7 demonstrates the PDF of the scalar fluctuation (ϕ') and scalar dissipation rate ($\chi = 2D[\partial\phi/\partial x)^2 + (\partial\phi/\partial y)^2]$). Here D is the mass diffusivity of the Rhodamine 6G in water, equal to $1.667 \times 10^{-3} \text{ mm}^2/\text{s}$ [122]. In the area of interest, the smaller fluctuations can be measured because the out-of-plane resolution is improved by the thin laser sheet. Similar to the spatial gradients of concentration, the larger χ , namely the higher rate at which two fluids mix and molecular diffusion processes lead to small-scale mixing, can be detected at the area of interest. The distribution of the χ has been investigated in many studies and it has been argued whether the distribution is log-normal [36, 128, 151]. This argument will be checked in further work. In the next step, the laser beam profile will be accurately measured by the knife-edge technique [41, 82]. Subsequently, this high-resolution PLIF technique will be used in the setup with certain inflow conditions to investigate the turbulent small-scale mixing.

2.3 Mixing in a T-mixer

The preliminary PLIF measurements indicate that measuring the full viscous-convective range in experiments is possible. But these results are only a proof of concept, which can hardly be exactly reproduced by other groups or in simulations because of the uncertain inflow conditions in the T-junction. Furthermore, the mass flows cannot be precisely controlled. This may lead to slight asymmetries in the flow states and makes estimations of the actual Reynolds number inaccurate. Indeed, a recent study has reported that inflow boundary conditions determine T-mixer mixing efficiency [143]. Thus, even if the Batchelor scale can be measured in the preliminary setup, the results would not offer a good basis for the development of accurate models and for the understanding of the mixing process. Hence, a full-scale, precisely manufactured setup (figure 2.9) was designed with sufficiently long inlets (to allow fully developed laminar duct flow up to at least $Re \approx 650$). The description of the setup and experimental results are illustrated below.

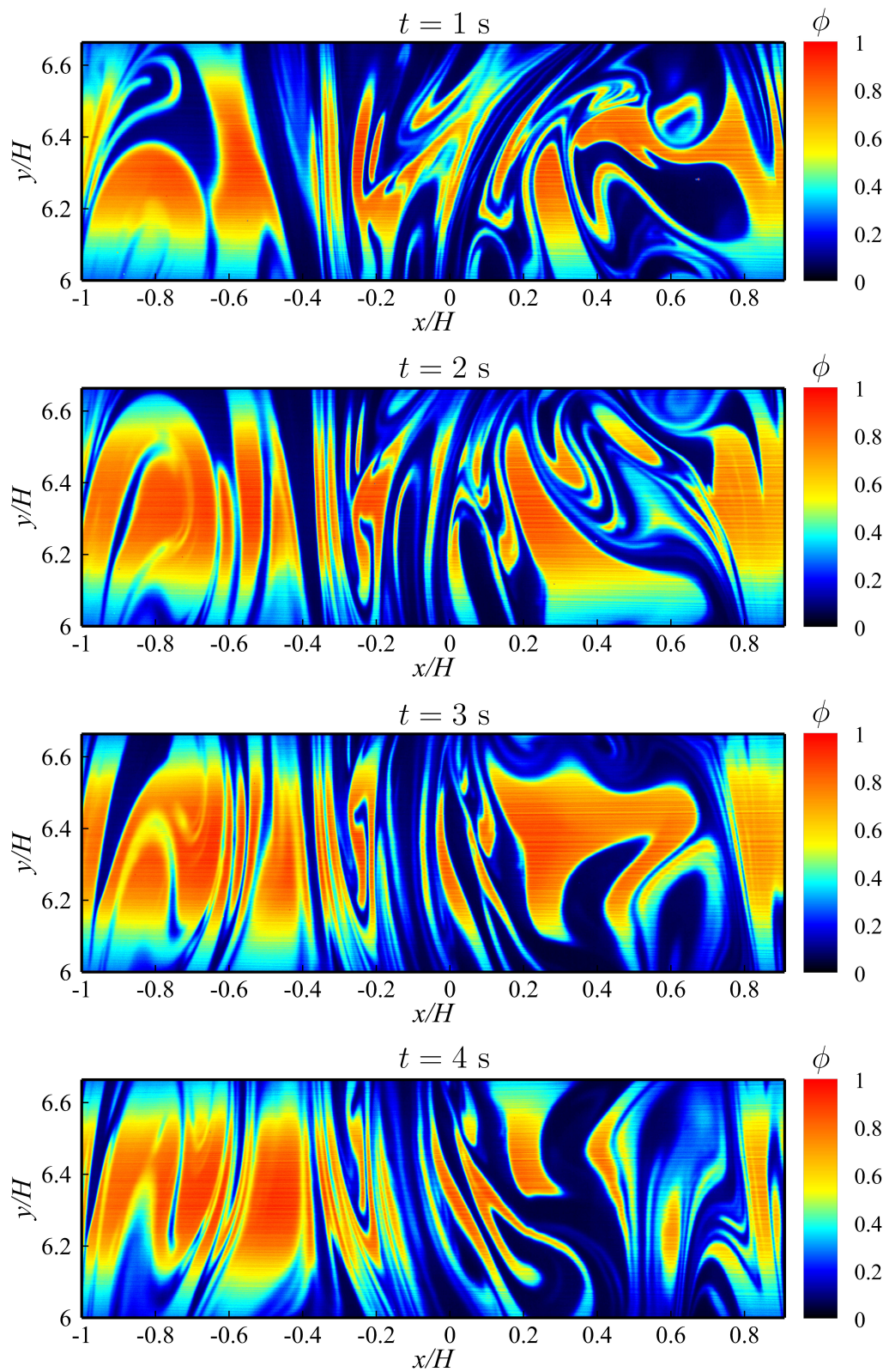


Fig. 2.8: PLIF snapshots at different times, from 1 s to 4 s.

2.3.1 Setup description

Figure 2.9 shows a picture of the T-mixer experiment. The fluid flow is driven at the two inlets by two pistons, which push at the same speed. The maximum output power of the servo motors is 570 W with the rotation speed 4980 RPM. The motors are connected to the end of the threaded shaft of the linear actuator, and the cart mounting on the actuator moves continuously, as shown in figure 2.9 and figure 2.10. Each piston connected to the cart by a shaft is driven to push the fluid at the desired flow rate. The outlet of each piston is connected to an acrylic tank through a rubber tube. Each connection position is located in the corner of the tank bottom. These two equal-sized acrylic tanks have a dimension of 340 mm × 340 mm × 500 mm. In this way, two tanks can facilitate decaying the perturbations from the linear driving systems. The outlet of each tank is connected to the square-cross section inlet (in dimension $H \times H$, $H = 40$ mm) through a contraction nozzle. The nozzle profile is key to generate a fully developed flow, and is designed according to

$$H_n(X_n) = H_i - (H_i - H_e)[6(X_n/L_n)^5 - 15(X_n/L_n)^4 + 10(X_n/L_n)^3]. \quad (2.5)$$

Here H_n is the height of the nozzle along the streamwise direction. H_i and H_e are the nozzle height at inlet and exit, respectively, which are equal to 120 mm and 40 mm based on the recommended contraction ratio (between 6 and 12) [17, 12]. Here X_n denotes the streamwise distance of the nozzle and L_n is the contraction length.

The present T-mixer setup aims to achieve the flow state at $Re = 650$ with fully developed laminar flow inlet conditions and the flow state at $Re = 4000$ with turbulent inlet conditions (the former being a more severe constraint on the development length). The T-mixer setup has a length of 6 meters and consists of T-junction and two inlet channels of square cross-section $H = 40$ mm with a length of 3 m ($75H$), see the sketch figure 2.10. As reported in Shah and London [146], the entrance length of a square duct for fully laminar developed flow can be approximated as $L/H = C \cdot Re$, in which the coefficient C varies between 0.0328 and 0.09. The worse-case coefficient $C = 0.09$ yields an entrance length of $L \approx 59H$ for $Re = 650$. Thus, for the

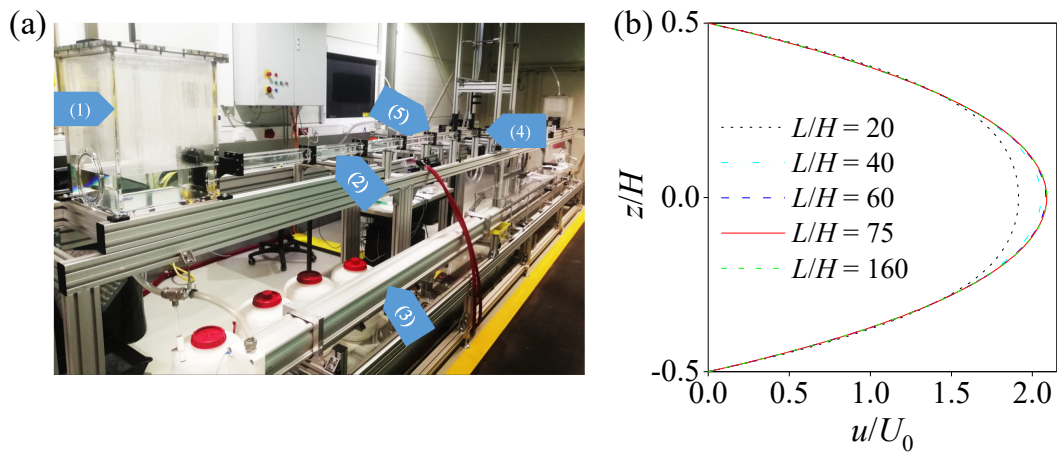


Fig. 2.9: (a) Picture of the T-mixer setup with two equally sized tanks (1), inlet channels (2), pistons and driving systems (3), a T-junction (4) as in figure 2.3(a) and an outlet channel (5). (b) Numerically computed velocity profiles at different development lengths for $Re = 650$.

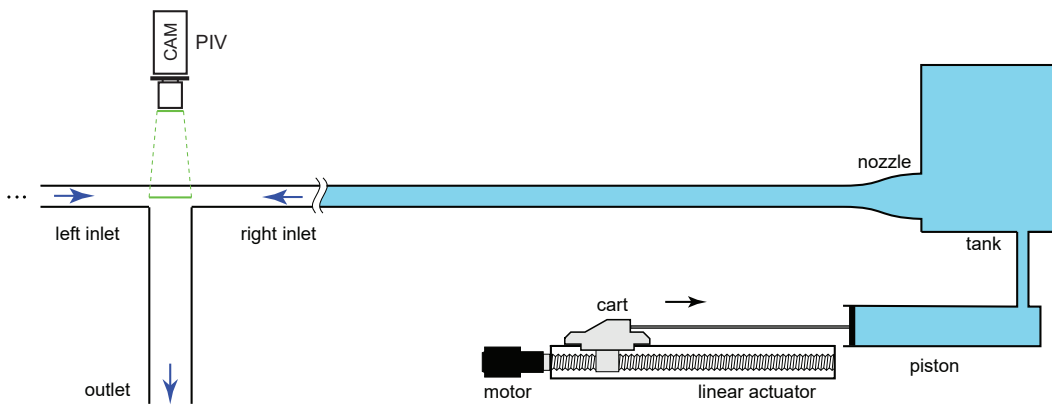


Fig. 2.10: (a) Sketch of the T-mixer setup, where the left branch is omitted (represented by three dots) to leave sufficient space for the details of the right-branch inlet. The setup consists of two symmetric branches and a T-junction section, where PIV measurements are taken. The arrows indicate the flow direction. The green parts show the laser sheet.

present inlet height ($H = 40$ mm), the inlet channel with a length of $75H$ (3 m) should be enough to obtain fully laminar developed flow for experiments. The simulations of this specific geometry (with the contraction nozzle) were also performed by ANSYS Fluent v18.2 in order to confirm that a fully developed flow will indeed be achieved in the present setup. Grid convergence studies were performed and a long inlet channel $160H$ was chosen to ensure the reliability of the simulations. As shown in figure 2.9(b), the profile is fully developed at the designed entrance length ($75H$). This guarantees that the target measurements with laminar inlet conditions up to at least $Re \leq 650$ are possible. The PIV technique was used to examine the fully developed laminar flows in the subsequent Section 2.3.3, thus in this thesis, the details of the simulations are not shown. The outlet (mixing channel) of the T-mixer with a rectangular cross-section $2H \times H$ (width \times height) is $25H$ long. The T-junction is the same as that in the Section 2.2.

The channels of the T-mixer are segmented and fabricated using acrylic glass (PMMA). Careful glueing of acrylic glass plates makes the square channels have the tolerance smaller than ± 0.25 mm for inlet width and height. Each segment channel has a length of 500 mm. They are connected through adapters and the connection parts are well sealed by O-ring, polytetrafluoroethylene band and silicon. The whole setup is supported by Bosch profiles for better operation and stability. During the assembly and experiments, the entire setup was carefully levelled using hydrodynamic equilibrium.

2.3.1.1 Experimental running time

The experimental running time (t_p) is determined by the volume of the pistons in the driving system. The running time of the T-mixer must be larger than $300 t_{adv}$ to account for transitions, to resolve the total mixing process and to provide sufficient experimental data for statistics and analysis [141]. Here t_{adv} is the advection time scale, defined as $t_{adv} = H/U_0$. It is found that the ratio of the running time (t_p) and the advection time (t_{adv}) is Re independent, namely,

$$t_p/t_{adv} = \frac{V_p}{Q_p} \frac{H}{U_0} = \frac{V_p}{H^2 \cdot U_0} \frac{H}{U_0} = V_p/H^3. \quad (2.6)$$

Tab. 2.1: The list of the main geometry parameters for the T-mixer system.

Parameters	T-mixer height	Entrance length	Piston diameter	Piston length
Symbol	H	L	d_{piston}	L_{piston}
Unit	[mm]	[mm]	[mm]	[mm]
Vaule	40	3000	125	2500

Here V_p is the volume of one piston and Q_p is the volume flow rate of one piston. Here, pistons with a diameter of 125 mm and a length of 2500 mm (about 30 liters) were chosen to ensure longer experimental time. The maximum experimental time can reach $475 t_p/t_{\text{adv}}$.

2.3.1.2 Consumption power estimation

The driving system is expected to achieve high Re flows (inlet conditions with turbulence), i.e. $Re = 4000$. Based on this Re , the consumption power in the T-mixer setup were evaluated to indicate the requirement of the input power. The consumption power contains two parts: friction power of pistons and friction power of liquid in the T-mixer channels.

Belforte et al. [11] investigated the relationship between the friction and velocity of the pneumatic piston. Here, the empirical formula is fitted based on their data, which gives

$$f_{\text{friction}} = 1.78 + 176.42 \times v_{\text{piston}} + 1179 \times v_{\text{piston}}^2, \quad (2.7)$$

where f_{friction} is the friction of the piston with unit N and v_{piston} means the velocity of the piston with unit m/s. The piston velocity for $Re = 4000$ can be calculated through the mass continuity equation, namely,

$$v_{\text{piston}} = \frac{4U_0H^2}{\pi d_{\text{piston}}^2} = \frac{4 \times 100 \text{ mm/s} \times 40^2 \text{ mm}^2}{\pi \times 125^2 \text{ mm}^2} \approx 0.013 \text{ m/s}. \quad (2.8)$$

Here the meaning and values of symbols are introduced in table 2.1. Thus, the piston friction power in one branch is estimated as

$$W_{\text{piston}} = f_{\text{friction}} \cdot v_{\text{piston}} = 4.27 \text{ N} \times 0.013 \text{ m/s} \approx 0.06 \text{ W} \quad (2.9)$$

Besides, for the safety of the driving system, the design factor is selected as 1.5, which gives the consumption of piston systems (two pistons) about 0.18 W. In addition, the consumption power of liquid friction is related to the pressure lose, which can be described as [179]

$$P_H = \Delta p_H \cdot Q_H. \quad (2.10)$$

Here the P_H is the consumption power of liquid friction, Δp_H is the pressure loss in the present system and Q_H denotes the volume flow rate in the channels. In practice, the turbulent dissipation is typically estimated as [143]

$$\varepsilon_{\Delta p} = \frac{\Delta p_H}{\rho} \frac{Q_H}{V_H} \propto \frac{U_0^3}{H}, \quad (2.11)$$

where V_H is the volume of fluid in the T-mixer and ρ is the density of water. V_H is about $200H^3$ for the present T-mixer. According to the T-mixer DNS of Schikarski et al. [143], their turbulent dissipation $\varepsilon_{\Delta p,S} \approx 4000 \text{ m}^2/\text{s}^3$ for $Re = 4000$ with the height $H_S = 1 \text{ mm}$. Here the subscript $(\cdot)_S$ refers the parameters from Schikarski et al. [143]. Thus, the dissipation in the present setup can be estimated through

$$\frac{\varepsilon_{\Delta p}}{\varepsilon_{\Delta p,S}} = \frac{U_0^3}{H} \frac{H_S}{U_{0,S}^3} = \frac{(0.10 \text{ m/s})^3}{0.04 \text{ m}} \times \frac{0.001 \text{ m}}{(4 \text{ m/s})^3} \approx 3.90 \times 10^{-7}, \quad (2.12)$$

$$\varepsilon_{\Delta p} = 3.90 \times 10^{-7} \times 4000 \text{ m}^2/\text{s}^3 \approx 1.60 \times 10^{-3} \text{ m}^2/\text{s}^3. \quad (2.13)$$

Following equation 2.10 and 2.11, the consumption power of liquid friction of the motions for the present T-mixer system is obtained and shown below,

$$\begin{aligned} W_H &= Q_H \times \Delta p_H = \rho \varepsilon_{\Delta p} V_H \\ &= 1000 \text{ kg/m}^3 \times 1.60 \times 10^{-3} \text{ m}^2/\text{s}^3 \times 200 \times 0.04^3 \text{ m}^3 \approx 0.02 \text{ W}. \end{aligned} \quad (2.14)$$

The fluid dissipation is negligible compared to the dissipation because of the friction of the motions. The total energy consumption of the T-mixer system is about 0.20 W, which is far smaller than the maximum power ($585 \times 2 \text{ W}$) of motors in the driving system.

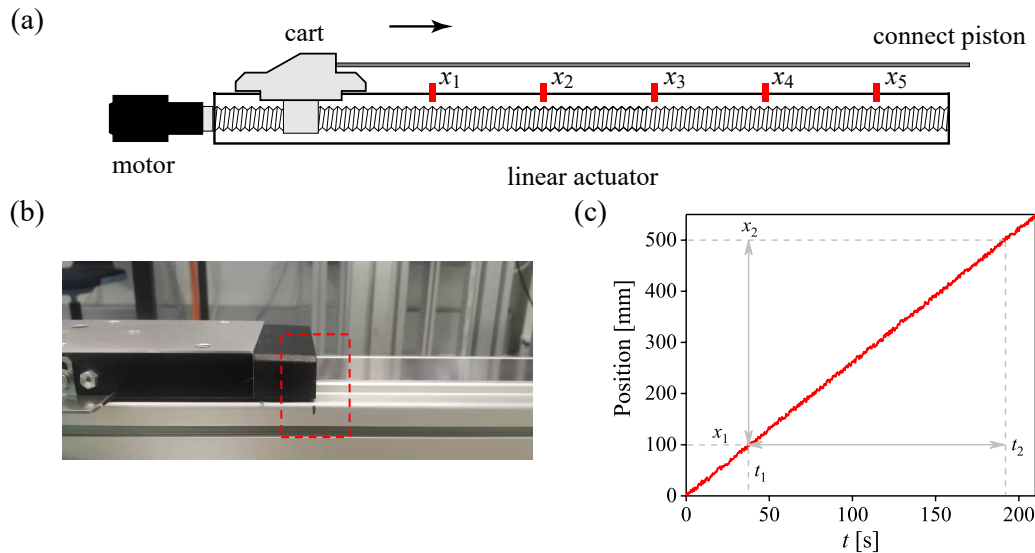


Fig. 2.11: (a) The sketch of five equidistant marked positions (400 mm) for the measurement of the piston velocity. (b) A snapshot when the cart of the driving system gets through a marked position. (c) Example sketch for the piston velocity measurements with $Re = 800$. The position velocity is calculated by the mean of the velocities in segments, namely $\sum_{i=1}^4 (x_{i+1} - x_i) / [4(t_{i+1} - t_i)]$.

2.3.1.3 Measurement uncertainty of Re

The Reynolds number is a crucial parameter for the flow in the T-mixer. Thus, this section mainly focuses on the maximum uncertainty of Re , which originates from the assembly error and displacement error of the driving system. Firstly, the piston velocity is verified through the below method. The motors of the driving system are precisely controlled via a National Instrument card. The software *IndraWorks* from Bosch-Rexroth[®] company is installed in a workstation. The driving system is set to synchronized motion mode. The motion of the pistons is steady. To check the velocity of the piston motion, a given distance is marked by black color on the linear actuator, as shown in figure 2.11(b). The video camera is used to capture the time when the cart gets through the markers. For a known distance, the mean velocity can be obtained based on the corresponding time interval (figure 2.11c). Thus, the length in the linear actuator, from 100 mm to 1700 mm, were separated as four equidistant segments, see figure 2.11(a). The tests were respectively assigned for the two pistons (use left side and right side to represent below) and were carried out twice for every distance. Figure 2.12 shows the comparison between the measured mean velocity and the mean

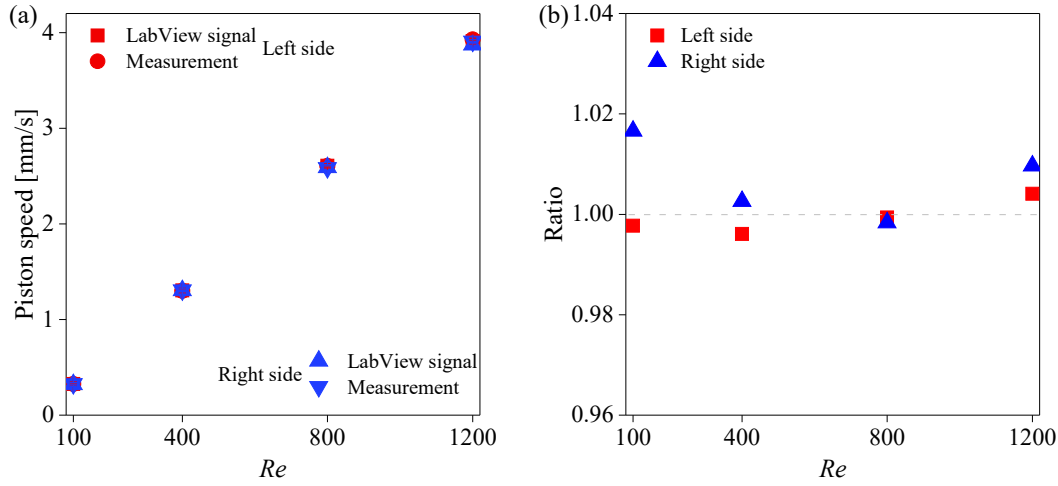


Fig. 2.12: The comparison between the measured mean velocity and the mean velocity from LabView signals at different Re , (a) for velocity and (b) for the ratio of the measured velocity and the input velocity. The red color denotes the data from the left side piston, while the blue color denotes the data from the right side piston.

velocity from the LabView signals. The error bar for measured velocity is calculated by the standard deviation of tests. For LabView signals, the mean and standard deviation of the data along the time is regarded as the mean velocity and the error bar, respectively. In figure 2.12, all data have good agreement and the maximum ratio of the measured and input velocity is only 1.02. Besides, the standard deviations of all measured velocities almost keep at the magnitude of $\mathcal{O}(10^{-2})$ mm/s.

Furthermore, the measurement uncertainty of Reynolds number can be estimated. For legibility, the Re number is shown here again,

$$Re = \frac{U_0 H}{\nu}. \quad (2.15)$$

Due to the mass continuity (see equation 2.8), the Re can be written as

$$Re = \frac{\pi v_{\text{piston}} d_{\text{piston}}^2}{4\nu H} \quad (2.16)$$

Thus, according to propagation of uncertainty, neglecting correlations and assuming independent variables,

$$\ln Re = \ln \frac{\pi}{4} + \ln v_{\text{piston}} + 2 \ln d_{\text{piston}} - \ln H - \ln \nu. \quad (2.17)$$

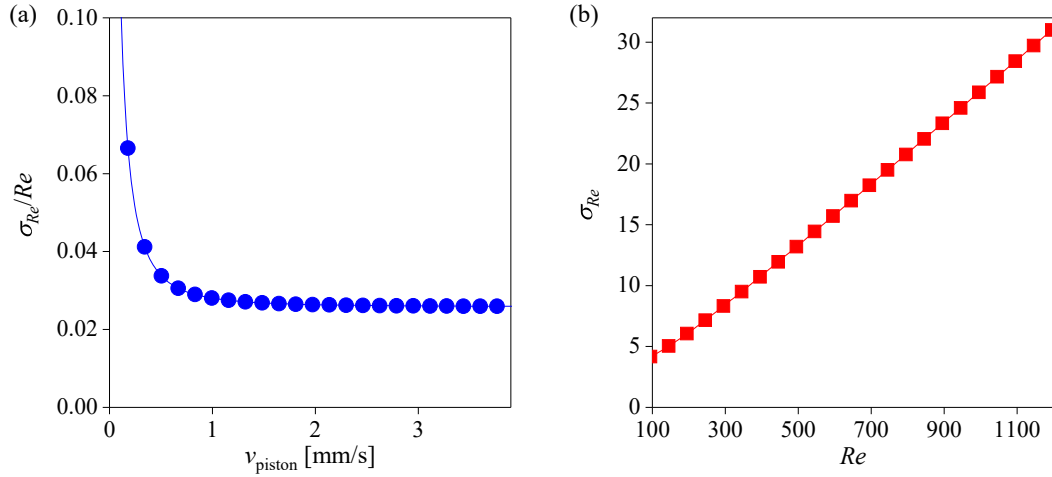


Fig. 2.13: The relative uncertainty of Re with different piston speeds (a). The Re uncertainty with different Re (b). The uncertainties when $Re < 100$ are not shown because the corresponding piston speeds are not verified.

The relative uncertainty of Re can be written as

$$\begin{aligned} \frac{\sigma_{Re}}{Re} &= \sqrt{\left(\frac{\partial \ln Re}{\partial v_{\text{piston}}}\right)^2 \sigma_v^2 + \left(\frac{\partial \ln Re}{\partial d_{\text{piston}}}\right)^2 \sigma_d^2 + \left(\frac{\partial \ln Re}{\partial \nu}\right)^2 \sigma_\nu^2 + \left(\frac{\partial \ln Re}{\partial H}\right)^2 u_H^2} \\ &= \sqrt{\left(\frac{1}{v_{\text{piston}}}\right)^2 \sigma_v^2 + \left(2\frac{1}{d_{\text{piston}}}\right)^2 \sigma_d^2 + \left(\frac{-1}{H}\right)^2 \sigma_H^2 + \left(\frac{-1}{\nu}\right)^2 \sigma_\nu^2}, \end{aligned} \quad (2.18)$$

where the symbol σ stands for the uncertainty and the subscript corresponds to each factor, which are listed respectively as follow:

- $\sigma_v = \pm 0.011$ mm/s: the uncertainty of the piston motion speed, which is the mean of measured standard deviations obtained by the method in figure 2.11.
- $\sigma_d = \pm 0.1$ mm: the uncertainty of piston diameter.
- $\sigma_H = \pm 0.3$ mm: the uncertainty of T-mixer channels, including manufacture error and assembly error.
- $\sigma_\nu = \pm(0.0247)$ mm²/s: the uncertainty of water viscosity, which is considered as the standard deviation of the four times measurements with a measuring instrument, namely Ubbelohde viscometer.

When other parameters are assumed as constants, furthermore, the Re uncertainty can be calculated by

$$\begin{aligned}\frac{\sigma_{Re}}{Re} &= \sqrt{\left(\frac{0.011}{v_{\text{piston}}}\right)^2 + \left(\frac{2 \times 0.1}{125}\right)^2 + \left(\frac{0.3}{40}\right)^2 + \left(\frac{0.0247}{1.003}\right)^2} \\ &= \sqrt{\left(\frac{0.011}{v_{\text{piston}}}\right)^2 + 6.65 \times 10^{-4}}\end{aligned}\quad (2.19)$$

Based on formula 2.19, the relative uncertainty of Re with different piston speeds is shown in figure 2.13(a). With the increase of the piston speed, the relative uncertainty becomes small. As an increase of Re , the Re uncertainty also increases, as shown in figure 2.13(b). When Re is over 100, the uncertainty almost has a linear trend with experimental Re . This figure demonstrates that in present experiments ($Re \leq 1100$), the maximum Re uncertainty is 27.6. The estimation in formula 2.19 also indicates that two important factors which can decrease the uncertainty during the experiments: (a) Ensure the temperatures of fluids in both inlets are the same all the time, which will reduce the uncertainty induced by variation of viscosity; (b) The assembly error is supposed to be negligible. Careful assembly is needed to have an alignment inlet channels.

2.3.2 PIV measurements

Particle image velocimetry (PIV) was employed in the full-scale setup (figure 2.10) for the velocity fields. PIV technique was used to measure the velocity field at a given location ($y/H = 0$) in the middle height of the outlet channel, see figure 2.1(b). A pulsed laser system (DM50-527 Photonics) and the same 12-bit CMOS camera (Phantom VEO 640L, 2560×1600 pixel²) were applied to implement two-dimensional PIV measurements. For PIV measurements, the whole setup was full of water seeded with 9-13 μm hollow glass spheres of specific gravity 1.03. The tracers are illuminated by a pulsed laser and the Mie scattering light is recorded by the camera. At least two images are acquired in brief succession so that the movement of the tracers in the images can be estimated. In a planar configuration, one camera enables measurements of the in-plane velocity components (commonly called 2D2C). The images are discretized in small interrogation windows, e.g. with a size

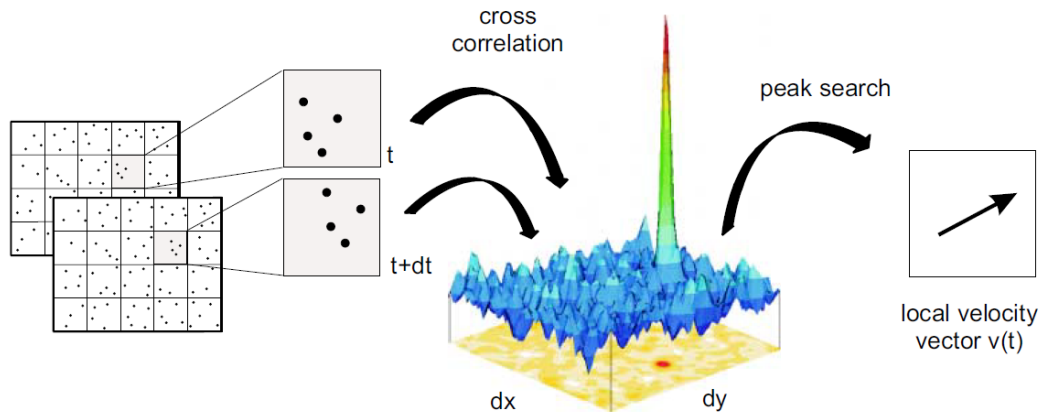


Fig. 2.14: Evaluation of PIV recordings using cross-correlation. The picture is adapted from [61].

of 32×32 pixels. Evaluation methods (e.g. Minimum Quadratic Difference and correlation schemes [68]) are then performed to find the most likely displacement of image patterns (or intensity distribution) in each interrogation window (see figure 2.14). The results are shown with displacement data on a rectangular grid. Finally, velocity data is obtained by scaling the physical tracer displacements (through the magnification of the camera) by the time separation between the recorded images. More details of the PIV technique can be found in the reference [134].

In this section, the displacement (velocity) fields were processed from raw PIV images using LaVision Davis 10 PIV processing software[©]. The multi-step algorithm is used with interrogation window 64×64 pixel² at the initial step reducing to the window 32×32 pixel² without overlap at the final step. The interrogation window at the final step includes approximate 7 dots for accurate displacement tracking [134]. The sample area of PIV measurement is of 80×40 mm², and the spatial resolution is $35 \mu\text{m}/\text{pixel}$. A typical uncertainty estimate of the instantaneous PIV sample is up to about 0.05 pixel (from LaVision Davis[©], see [180]). Machined hardware mounts were used to rigidly fix the camera and laser sheet orthogonally.

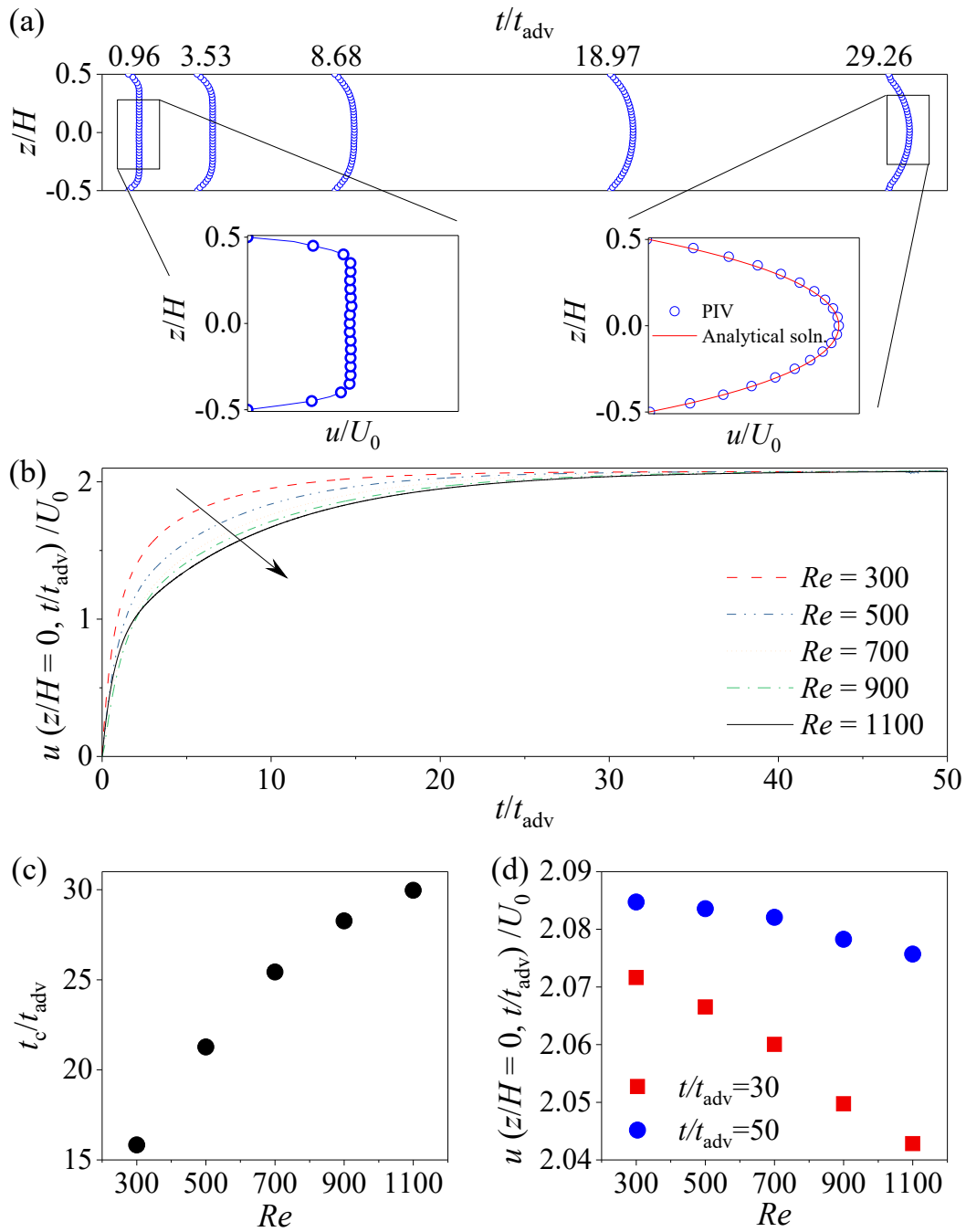


Fig. 2.15: (a) Comparison of velocity profiles between PIV and analytical solution in the left inlet channel of the T-mixer at $Re = 700$ and $x/H = -2.5$. In the inset, the red solid line is the analytical velocity profile from the square duct flow [146] and the blue hollow circle means the velocity profile from PIV measurements. (b) Comparison of centerline ($z/H = 0$) velocity normalized by the bulk mean velocity (U_0) versus dimensionless developed time t/t_{adv} for varying Reynolds numbers (here $t_{adv} = H/U_0$). The arrow indicates the direction of the curves' transition from $Re = 300$ to $Re = 1100$. (c) The critical developed time t_c/t_{adv} when the centreline velocity reaches 98% of asymptotic steady state velocity. (d) Centerline u/U_0 at different Re when $t/t_{adv} = 30$ and $t/t_{adv} = 50$.

2.3.3 Laminar inlet flows

For a square duct flow, the fully developed velocity profile is described as [146, 26]:

$$u(x, t) = -\frac{4H^2}{\pi^3} \frac{dp}{\mu dx} \sum_{n=1,3,\dots}^{\infty} \frac{1}{n^3} (-1)^{\frac{n-1}{2}} \left[1 - \frac{\cosh(n\pi y/H)}{\cosh(n\pi/2)} \right] \cos\left(\frac{n\pi z}{H}\right), \quad (2.20)$$

where dp/dx is a pressure drop and μ is the dynamic viscosity of water. The mean velocity, U_0 is

$$U_0 = -\frac{H^2}{12} \frac{dp}{\mu dx} \left[1 - \frac{192}{\pi^5} \left(\frac{a}{b}\right) \sum_{n=1,3,\dots}^{\infty} \frac{1}{n^5} \tanh\left(\frac{n\pi b}{2a}\right) \right]. \quad (2.21)$$

In the setup, the fluid is driven by an imposed constant volume flux, note however that in the laminar regime the results are identical as for fluid driven at a constant pressure drop (e.g., [28]). To check the fully developed laminar flow of the present setup, the PIV technique is employed in both upstream inlets at the plane $y/H = 0$ ($x/H = -2$ to $x/H = -3$, $x/H = 2$ to $x/H = 3$, see the coordinates in figure 2.1). The measurement is taken in the upstream positions with a distance $2.5H$ to the centre of the T-mixer to avoid the effects of the flows at the T-junction on the velocity profiles. Figure 2.15(a) demonstrates the velocity profiles of an inlet channel for $Re = 700$. The measurement results are in very good agreement with corresponding theoretical velocity flow profiles (equation 2.20 in a square duct, see the inset in figure 2.15(a)). When the centerline velocity reaches 98% of asymptotic steady state velocity, here, the flow is defined to reach a fully developed state [28]. These results indicate that the entrance length can guarantee a fully developed laminar flow with $Re \leq 1100$. Besides, the centerline velocities for different Reynolds numbers are shown in figure 2.15(b). The required dimensionless time (by $t_{adv} = H/U_0$) for each flow to reach asymptotic steady state velocity increases monotonically as the Reynolds number increases, which can also be observed in figure 2.15(d). To guide the experiments below, the critical development times for different Reynolds numbers are extracted and shown in figure 2.15(c). According to these findings, the following experiments are started when the fully developed laminar flow is achieved.

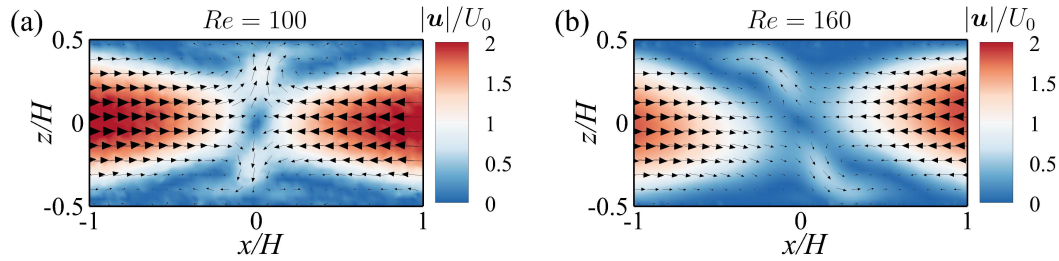


Fig. 2.16: The velocity field from PIV results when (a) $Re = 100$ and (b) $Re = 160$. The velocity vector components are displayed every 3 points in x and z directions for clarity.

2.3.4 Mixing patterns when $Re < 400$

When $Re = 100$, flows are left-right, top-down symmetric and accordingly the four vortices are approximately symmetric, as shown in the PIV results in figure 2.16(a). It is notice that after a long-time running the experiments, the flow pattern in this range gradually becomes slightly asymmetric, which is due to thermal convection effects. Because the room temperature is not uniform in space and has a difference from the water temperature, in the present large-scale setup, it gives rise to a weak thermal convection circulation and then affects the flow regimes in the T-junction. Investigations of this effect are not reported in previous experimental studies because of their small-scale setups, leading to much smaller Rayleigh numbers. The physics and effects of the thermal convection on T-mixer flows are worth to be investigated further. Here a brief introduction of this thermal effect on velocity profiles is shown in the Section 2.3.5.

When $Re > 105$, the steady engulfment flow emerges in agreement with DNS of [142]. For example, in figure 2.16(b), two counterclockwise rotating vortices were observed. During the experimental time, these two vortices remain approximately steady. In different experimental trials, the two vortices are equally likely to occur clockwise and counterclockwise, which was already observed in [160] as well and confirms that the setup was built to high accuracy, thus preserving the spatial symmetries of the system. With the increase of Re , the flow pattern becomes unsteady (periodic) engulfment flow. Figure 2.17 shows the velocity field at a different time in a period when $Re = 280$. This regime is characterized by a periodic shear-layer process at the fluid interface. In the beginning, two vortices are gradually formed at

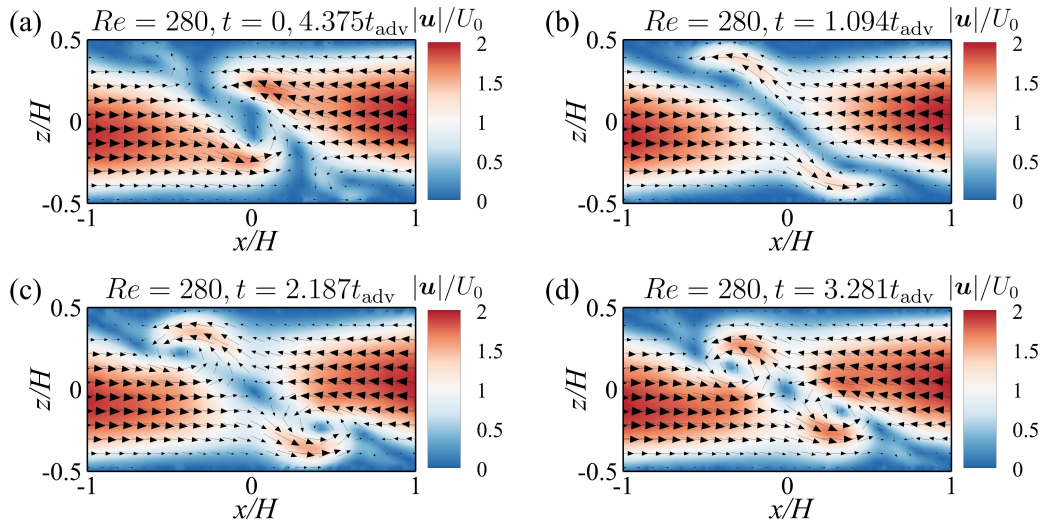


Fig. 2.17: The velocity field from PIV results at a different time when $Re = 280$: (a) $t = 0$ and $t = 4.375t_{adv}$; (b) $t = 1.094t_{adv}$; (c) $t = 2.187t_{adv}$; (d) $t = 3.281t_{adv}$. The period is $4.375t_{adv}$. The velocity vector components are displayed every 3 points in x and z directions for clarity.

the left-upper and right-low corners (see figure 2.17a-b). Subsequently, two vortices slowly roll along with the inter-fluid interface (figure 2.17c-d), and engulf each other in the centre of the channel figure 2.17 (a), before a new process begins.

For $300 < Re < 340$, both periodic unsteady engulfment flow and unsteady symmetric flow can occur, but the likelihood of unsteady symmetric flow increases with increasing Re . For $Re > 340$, almost all realizations yield symmetric flow with quasi-periodic temporal dynamics. Figure 2.18 shows the velocity field at different times for PIV results when $Re = 360$. In the figure, four vortices (clockwise and counterclockwise) stay in the symmetric position leftward and rightward. At a different time, these four vortices move quasi-periodically around their positions at the top and bottom walls, resulting in the centerline of the two streams also tilting along with the time rather than being strictly vertical. As Re increases, this topology is less likely to be maintained and the degree of asymmetry increases as the flow becomes chaotic. Note that when the time average is taken, the left-right and top-bottom symmetries are recovered in this regime (in contrast to the chaotic engulfment regime, which only retains a central symmetry in average).

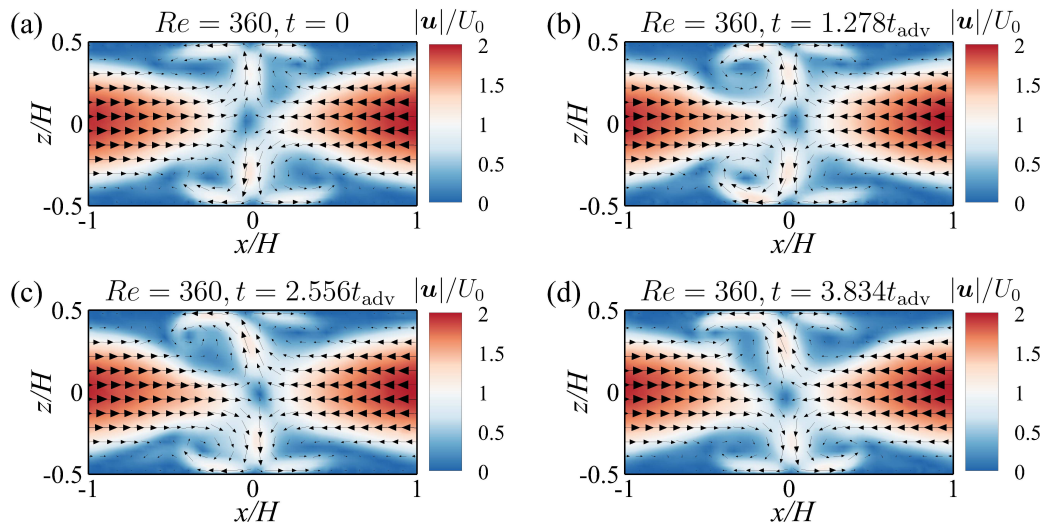


Fig. 2.18: The velocity field from PIV results at a different time when $Re = 360$: (a) $t = 0$; (b) $t = 1.278t_{adv}$; (c) $t = 2.556t_{adv}$; (d) $t = 3.834t_{adv}$. The quasi period approximates $5.112t_{adv}$, as shown in figure 2.19. The velocity vector components are displayed every 3 points in x and z directions for clarity. how to estimate the frequency, More snapshots

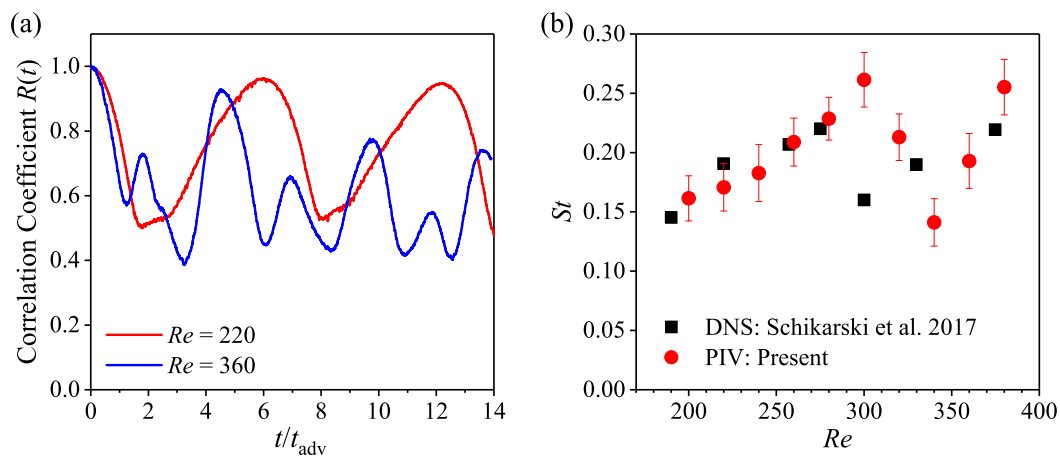


Fig. 2.19: (a) The time correlation of the velocity magnitude when $Re = 220$ and 360 . (b) Strouhal number as a function of Reynolds number. The data from the simulations of Schikarski et al. [142] are shown as black circles.

The main frequency f of the periodic and quasi-periodic flow, expressed with the dimensionless Strouhal number (St), can be compared to the present study by computing $St = fH/U_0$. In order to quantify periodicity for unsteady flows in the present study, the velocity magnitude $|u|_k$ between frame $k - 1$ and frame k (where k is from 2 to the total number of image frames), was correlated to $|u|_1$ between image frame 1 and frame 2 using

$$R(k) = 1 - \frac{1}{M \times N} \sum_{m=1}^M \sum_{n=1}^N (|u|_1(m,n) - |u|_k(m,n))^2, \quad (2.22)$$

where M and N are the number of the velocity vectors along x and z directions, respectively. Equation 2.22 is similar to one of the image correlation algorithms, named the Minimum Quadratic Difference method [68]. The correlation coefficient along time is plotted in figure 2.19(a), in which the periodicity can be observed in 14 advect time units. As shown in figure 2.19(b), between $Re = 300$ and 340 there is a sharp change of the Strouhal number, which was attributed to the onset of regaining the symmetric flow occurs. Our experimental results are in agreement with those of Schikarski et al. [142]. As the flow becomes asymmetric and chaotic, it becomes difficult to extract the main oscillation frequency and longer experimental runs analyzed with Fast Fourier transform to extract the spectra would be necessary.

2.3.5 Thermal convection

When the experiments were carried out, it was found that the room temperature was not uniform in space and was different from the water temperature. The fan for laser system is under the T-mixer setup, thus the temperature of the T-mixer bottom is a little higher than that of the top, as shown in figure 2.20(b). In the present full-scale setup, this temperature difference affects the velocity profile of the laminar flow and the flow regimes in the T-junction. The temperature difference roughly gives the Rayleigh number,

$$Ra = \frac{\beta \Delta T H^3 g}{\nu \alpha} = \frac{0.21 \times 10^{-3} \text{ 1/K} \times 0.54 \text{ K} \times (0.04 \text{ m})^3 \times 9.8 \text{ m/s}^2}{0.96 \times 10^{-6} \text{ m}^2/\text{s} \times 0.143 \times 10^{-6} \text{ m}^2/\text{s}} \approx 5.18 \times 10^5, \quad (2.23)$$

where β is the thermal expansion coefficient, ΔT is a temperature difference and α is the thermal diffusivity. The Rayleigh number indicates that the

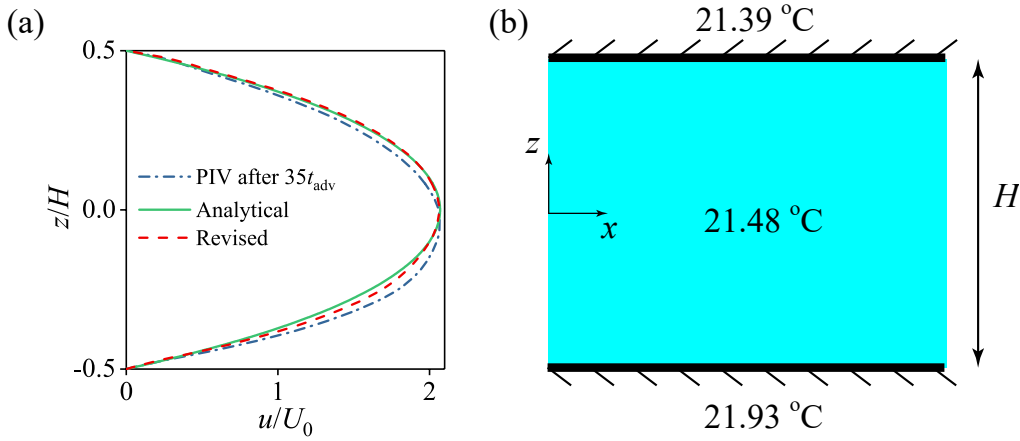


Fig. 2.20: (a) The velocity profile at $x/H = -2.5$ when $Re = 500$. The green solid line denotes the analytical solution and the red dash dot line is the laminar velocity profile according to thermal effects. (b) The sketch of the T-mixer inlet channel with a temperature difference. The gravity acceleration is along the negative z direction.

convection in the present setup is laminar [97] but affects the velocity profiles. As shown in figure 2.20(a), for the velocity profiles of PIV results upstream of the T-junction ($x = -2.5H$), after a long time running, at $35t_{adv}$, the velocity profile should have been fully developed (see green solid line in figure 2.20a) however it became asymmetric with respect to the centre plane of the channel height (the blue dash-dot line in figure 2.20a). This phenomenon is thought to be induced by the thermal convection. Because when the driving system is turned off, the weak motions of the water in the channels are also observed after 20 minutes duration, which is expected to be driven by the thermal convection circulations, see the PIV measurements in figure 2.21. The transverse convection rolls perpendicular to the flow direction in channel flows have been reported in many studies [183, 120, 65]. The motion of this thermal effect is worthy to be investigated but needs to be avoided for the mixing experiments in the T-mixer.

The PIV time-average velocity (within 4 minutes) u_q in the quiescent experiment (in figure 2.21) are used to compensate the measured laminar fully developed flow velocity u_{PIV} (see the blue dash-dot line in figure 2.20a), namely,

$$u_r(x/H = -2.5) = u_{PIV}(x/H = -2.5) - u_q(x/H = -2.5). \quad (2.24)$$

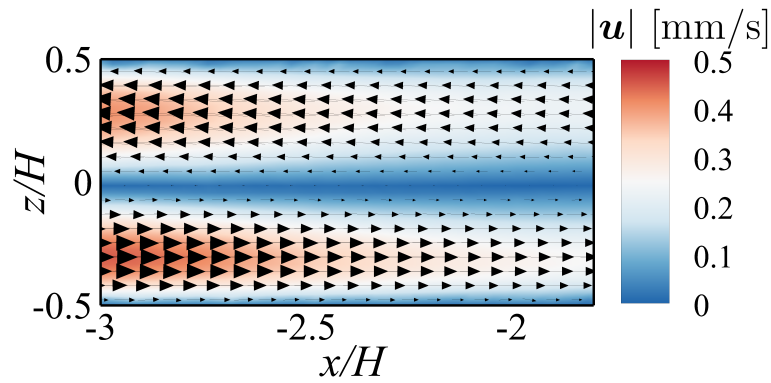


Fig. 2.21: A snapshot of the thermal convection of PIV results after 20 minutes stopping of the driving systems at left inlet channels.

The revised velocity profile u_r is shown in figure 2.20(a) with a red dash line and agrees with that from the analytical result at $Re = 500$ (see green solid line in figure 2.20 by equation 2.20), which is thought that this thermal convection is the main factor that influences the fully developed laminar velocity profile and possibly further affects the flow regimes in the T-junction. It should be noted that experimental results in previous sections are measured at different times on different days to mitigate this thermal effect. In addition, whether this thermal effect can cause PIV measurement errors because of the density difference is unclear. It will be investigated in detail in the next Chapter.

2.4 Summary and thoughts

In this Chapter, a large-scale T-mixer with a height of 40 mm was presented. It is beyond the dimensions of mostly used micro-scale T-mixers with the same geometry. The design description is shown in detail. A high-resolution PLIF technique is implemented and preliminary PLIF measurements in the T-junction indicate that measuring the full viscous-convective range (down to the Batchelor scale) in experiments is possible. Subsequently, the PIV technique is used in the improved setup with sufficiently long inlets. It is found that the present setup can produce the inlets with fully developed laminar flows when $Re \leq 1100$ and reproduces the flow regimes in previous studies. With the increase of the Reynolds numbers in the T-mixer, different flow regimes have been identified, i.e., steady asymmetric flow and periodic asym-

metric flow and the unsteady symmetric flow. In further work, the chaotic flows will be measured and the spatio-temporal dynamics of turbulence will be investigated.

Due to the a height of 40 mm, thermal effects can influence the flow regimes during the experiments. The thermal effects are measured with PIV, which are used to compensate the velocity profile and it agrees with that from the analytical solution. In the future, the whole setup should be improved with adjustments (e.g., isolation between the setup and room, homogenization of the air in the room) to avoid this effect. Finally, the high-resolution PLIF should be performed and the scaling of mixing down to the Batchelor scale could be measured in the full-scale setup. It is noted that Schwertfirm et al. [145], Gradl and Peukert [64] have performed experimental measurements of the species concentration and obtained temporal spectra of the passive scalar fluctuations in a T-mixer with circular inlets by using a high-resolution PLIF technique (similar to the present PLIF technique, section 2.2.3). They showed that the spectra broaden as the Reynolds number increases, suggesting that the Batchelor scale decreases. But their velocity field measured with PIV is only in qualitative agreement with that of DNS, which can mainly attributed to differences in the inflow conditions. In the present setup, the T-mixer is designed with square inlets, and the inflow conditions can guarantee to have a fully developed laminar flow. This is helpful to compare the velocity field with DNS and further understand the turbulent mixing and flow instabilities in T-mixers, in order to achieve a qualitative and quantitative understanding of small-scale mixing.

In addition, the characterization of small-scale mixing in the T-mixer can serve as a basis for studying the case of active scalar mixing, which is much less understood, e.g. of fluids with different viscosities, as in recent experimental work in a T-mixer [19]. In their study, refractive index matching is used to obtain the fluids with the same refractive index but different viscosities, which minimize the reflection, refraction, and diffraction for PLIF images. However, in applications, the fluids usually are used with different densities, refractive indexes and viscosities (e.g., water and ethanol), which makes it difficult to implement the optical technique during the liquid-liquid mixing. Besides, in the present setup, the thermal effect can also give rise to the

inhomogeneous refractive index field of the water in the channel. It brings a new question of whether this difference can cause large measurement errors in PIV and PLIF results. Thus, it is necessary to quantify the measurement error induced by the inhomogeneous refractive indexes for optical technique during the mixing. On the other hand, the optical measurement errors can also be utilized to understand the development of the density field during the mixing. For example, the technique, named background-oriented schlieren (BOS), can measure the inhomogeneous refractive index field and further obtain the density field distribution in a 3D domain along the time [158, 119]. In the next Chapter, a ray tracing simulation is used to estimate the optical measurement errors during the mixing processes.

Optical measurement errors in fluids flow with density differences

3.1 Optical distortion in different mixing fluids

In the previous Chapter, the mixing of two water systems (one of which has a small amount of Rhodamine 6G) was investigated with PLIF and PIV techniques. It should be noted that measurement precision of these two optical techniques relies on a sufficient quality of the images (e.g. noise and sharpness), which are limited by the refractive index field of the fluid. As shown in the previous Chapter, a weak inhomogeneous temperature distribution had a small but noticeable effect on the flow regime. To what extent it can contaminate the optical measurements is unclear. Furthermore, in many applications, mixing happens in two streams with large density difference, e.g., between ethanol and water, and the flow field has an such inhomogeneous refractive index field. In such flow fields, photons (from tracers or fluorescent dye) do not travel along straight paths, but follow more complex trajectories (light ray), e.g., due to light refraction and diffraction. Consequently, the images from PIV or PLIF technique can be blurred, as shown in figure 1.5. The deterioration of the image quality then results in an increased measurement error of the flow velocity and concentration.

This inhomogeneity in the refractive index field spatio-temporally change in flows with shock waves, thermal convection, combustion or liquid mixing of different fluids (e.g., water and ethanol in a turbulent T-mixer). If the PIV measurement is carried out in these flows, the quality of the measurement images is contaminated by the inhomogeneity. In compressible air flows, a

shock wave has a discontinuity of the refractive index field produced by the density (temperature) fields, and is often approximately two-dimensional. Thus, when the illuminated field is seen through shock waves or shear layers, the position error and the blur of the tracer image can be dramatic [132, 51]. Raffel and Kost [132] introduced a formula to estimate the size enlargement of the imaged tracers in order to quantify the position error of the imaged tracers seen across the shock wave. Elsinga et al. [51] studied aero-optical errors of PIV measurements in an approximately two-dimensional flow and found that the formula of Raffel and Kost [132] overestimates the light ray deflection.

For thermal convection, because of the existence of temperature differences, three-dimensional turbulent flow structures make the density field inhomogeneous and the corresponding refractive index field changes in space and time. One example is Rayleigh-Bénard convection in a closed cell, which is heated at the bottom and cooled at the top [14, 104]. The characteristic three-dimensional flow structures (e.g. plumes and large-scale circulation) advect in time [14] with velocity and temperature fluctuating strongly at small scales [104]. In the meanwhile, correspondingly, the three-dimensional refractive index patterns deflect the light in space, and importantly the deflection also changes in time. The variation of the light deflection over time brings in another dimension of the deterioration of the tracer image quality. The optical distortions of tracers due to temperature difference (giving rise to refractive index difference) were observed in Rayleigh-Bernard convection experiments [166], in which background oriented schlieren (BOS) technique was used as a preliminary investigation before doing PIV measurements, to check whether at the chosen experimental conditions the optical distortions still allowed to sufficiently see the particles. It was found that for the temperature difference equal to 2.6 K in their experiments, blurring due to optical distortions did not obstruct the visualization of the tracers, except in the boundary layer regions.

In turbulent flames, measurements with PIV and laser Rayleigh imaging techniques are also affected by the inhomogeneous refractive index field produced by temperature differences [155, 84]. In a recent experimental study [169], PIV measurement error in combustion (propane) flow was

quantified, where the tracer position error inside the flow was measured in a time-averaged manner. This averaged error of the tracer position was then combined with the time-averaged flow velocity from the PIV measurement inside the flame to determine the PIV measurement error. Specifically, Vanselow et al. [169] found that the *time-averaged* relative velocity error over 500 PIV measurements is up to 4 %. This systematic measurement error is larger than the typical relative error of about 1 % for a single PIV measurement [178, 134]. More recently, they extended their study to the velocity measurement errors for stereoscopic PIV in the same experimental setup and found that the measurement error can be one order of magnitude larger than the standard PIV [171].

Laser beam deflection, the image distortion and the PIV measurement error were also reported for a hot jet, porous media flows (with the refractive index difference between the solid and the liquid), and a thermal boundary layer of a melting paraffin wax, respectively [170, 125, 54]. Thus, for the optical techniques, not only in turbulent mixing flows but also in other flows, the errors induced by the inhomogeneous refractive index field should deserve more attention. Particular care can reduce the refractive index difference, e.g., with refractive index matching technique [181, 43, 7], but for general situations, especially with spatial-temporal changing refractive index field, this technology is of limited use.

In summary, the photon trajectories in many flows are determined by the spatio-temporal behaviour of the refractive index field inside the flow [170]. The temporal evolution of the flow influences the photon trajectories, even if the photon starts at the same position and along the same direction. The time-dependent error of the tracer position and the velocity error are coupled [51, 169], thus the position error and the actual velocity are simultaneously required for the quantification of the *instantaneous* velocity error to evaluate the systematic and the random error of the measurements. However, this is difficult (or infeasible) in experiments.

As an alternative approach, the effects of the inhomogeneous refractive index field can be studied with ray tracing simulations in simulated flows [89], where the photon trajectories inside the flows can be simulated on the basis of

Tab. 3.1: The list of studies on tracer position error (or angle deflection) from inhomogeneous refractive index field.

Reference	Flow	Medium	Δn_{\max}	K (m^3/kg)	Method
Vanselow and Fischer [170] ¹	Hot jet flow	Air	9.9×10^{-5}	2.3×10^{-4}	Experiment: laser beam
Guo et al. [69] ²	Shock wave on conical vehicle	Air	2.0×10^{-5}	2.3×10^{-4}	Simulation: Snell's law (DSMC)
Elsinga et al. [51] ³	Compressible shear layer	Air	9.0×10^{-5}	2.3×10^{-4}	Theory
		Air	6.9×10^{-5}	2.3×10^{-4}	Experiment: PIV & BOS
	Prandtl-Meyer expansion fan	Air	7.4×10^{-5}	2.3×10^{-4}	Theory
		Air	7.1×10^{-5}	2.3×10^{-4}	Experiment: PIV & BOS
Stella et al. [155] ⁴	Premixed turbulent flames	Air-propane	1.3×10^{-3}	3.0×10^{-4}	Theory
		Air-propane			Experiment: laser beam
Raffel and Kost [132] ⁵	Shock wave	Air	1.0×10^{-4}	2.3×10^{-4}	Experiment: Snell's law
Kirmse et al. [88] ⁶	Shock wave	Air	6.3×10^{-6}	2.5×10^{-4}	Simulation: ray tracing (CFD). Experiment: BOS
					Experiment: PLIF
Oljaca and Glezer [123] ⁷	Plane shear layer	Water	3.4×10^{-4}	–	Experiment: PLIF

¹ Gradient of refractive indices along the direction perpendicular to the laser beam was converted and used here.

² Incidence angle was not explicitly defined.

³ Refractive index field was extracted from their figure 9 and 10.

⁴ Refraction at flame fronts was considered. The data from their table 5 were extracted.

⁵ The shock wave was assumed as the interface of two media with refractive index difference.

⁶ Maximum refractive index difference was extract from the legend of their figure 12.

⁷ Dependence of deflection angels on spatial distribution of refractive index field was discussed but no data were presented. The temperature difference is up to 5°C .

the known refractive index field in the scope of geometric optics (neglecting light diffraction). This approach enables studying three-dimensional spatio-temporal refractive index fields. It is particularly important for turbulent flows which are spatio-temporally chaotic, three-dimensional and feature substantial scale interactions. In previous work, Guo et al. [69] simulated light rays over discrete grids following Snell's law for the approximately two-dimensional shock wave attached to a conical-head vehicle. However, the numerical iteration of Snell's law over discrete grids possibly gives an insufficient accuracy, if grid sizes are not sufficiently small [154]. In contrast, solving the Fermat's ordinary differential equation, e.g., with a Runge-Kutta scheme, provides good accuracy in ray tracing simulations [88]. The latter is employed in this Chapter to render almost realistic PTV images in a simulated single-phase, three-dimensional turbulent flow.

In order to only study the effects of the spatio-temporally varying refractive index field on the motion in measured images, the present Chapter is focused on the tracer-based measurement principle, especially PTV measurement error of the flow velocity and the flow acceleration, respectively. The refractive index field is obtained from a DNS of a homogeneous buoyancy-driven turbulent mixing process (shared by Johns Hopkins Turbulence Database [103]). This mixing process is different from the mixing in the T-mixer, the optical measurement errors can also be extrapolated to other systems, such as the T-mixer.

3.2 Approach for an inhomogeneous refractive index field

3.2.1 Tracing light rays

The tracing of a light ray of an illuminated tracer in an inhomogeneous density field is illustrated in figure 3.1(a). The flow domain is three dimensional in size of $L \times L \times L$. In the two-dimensional sketch, the $x_2 - x_3$ plane at $x_1 = 0$ is illuminated with a light sheet (the green line). A illuminated tracer scatters a

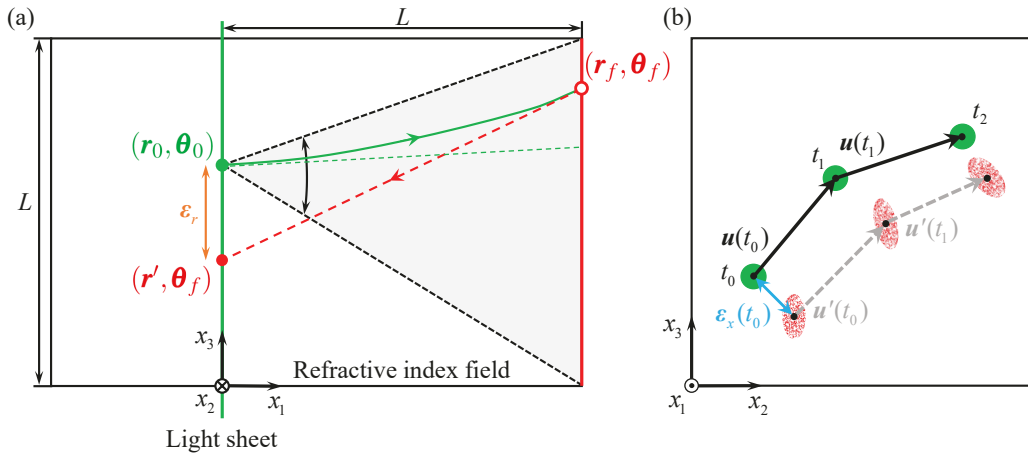


Fig. 3.1: (a) Two-dimensional schematic of tracing a light ray in a three-dimensional inhomogeneous refractive index field. The gray area (enclosed by two black dashed lines) marks the range of θ_0 . The ray position shift is $\epsilon_r (= r_0 - r')$ marked by an orange double-head arrow. (b) Illustration of tracer position and tracer velocity at three times (t_0, t_1, t_2) for the homogeneous and the inhomogeneous refractive index field cases. For the latter, the red dots at the position r' in (a) form elliptical shaped tracers, while the green circles indicate the imaged tracers from the former case. Black dots mark the respective tracer center. Black and gray arrows indicate the respective velocity, and the blue double-head arrow marks the position error at t_0 .

light ray at the position r_0 (the green dot) towards the plane $x_1 = L$, and the initial direction of this ray (the green dashed line) is defined by a vector θ_0 of angles in reference to x_1 . In the scope of geometric optics, the propagation trajectory of a photon can be described by Fermat's equation as

$$\frac{d}{ds} \left[n(\mathbf{r}) \frac{d\mathbf{r}}{ds} \right] = \nabla n(\mathbf{r}), \quad (3.1)$$

where \mathbf{r} is the ray curve, $n(\mathbf{r})$ is the refractive index field, and ds is an infinitesimal increment of arc length along the trajectory. $n(\mathbf{r})$ is obtainable from a flow field with the DNS, so that a ray curve in a flow can be computed numerically in Fermat's equation when the initial conditions of the ray are given. In practice, light rays leaving the domain border of the flow field are collected by a group of optical lenses to a camera screen. The lenses may produce aberrations [67], which cause difficulties in isolating the effect of the refractive index field on the measurement error. As shown in figure 3.1(a), in this study, a ray (the green line with an arrow) reaching the final position (the hollow red circle) in the final plane (red solid line) was projected back to the light sheet plane (the green vertical line) along a straight line (the red

dashed line with an arrow) with the angle θ_f . This configuration ensures that the studied ray deflection and the tracer position error are only associated with the refractive index field [51]. The projected ray reaches its destination \mathbf{r}' (the red dot in figure 3.1) at $x_1 = 0$ (the light sheet), and a sufficient number of rays consequently forms an imaged tracer (see figure 3.1b).

3.2.2 Measurement arrangement

Given the working principle of PTV techniques, the measurement precision is closely associated with the quality of tracer images, which is linked with the position of the imaged tracers that are formed by light rays. For this, the direction of the light ray, and then the position of the imaged tracers, as well as the flow velocity and the acceleration are evaluated.

The direction of the light ray, characterized by θ_0 and θ_f , is directly obtained from the ray tracing simulation. When a large number of the light rays from a tracer reaches $x_1 = 0$ (the imaging plane, the same as the light plane), an image of the tracer is rendered (see details in Section 3.3.2). The measured tracer position \mathbf{x}' is the tracer center obtained by the centroid method for the image of a tracer,

$$\mathbf{x}' = \int_0^L \int_0^L \mathbf{g}'(x_2, x_3) \cdot w(x_2, x_3) dx_2 dx_3 / \left(\int_0^L \int_0^L w(x_2, x_3) dx_2 dx_3 \right), \quad (3.2)$$

where \mathbf{g}' are pixel coordinates in the image (see Section 3.3.2), and w is the weighting factor which is the pixel grayscale in this study.

The tracer velocity is obtained from the change of the tracer position $\mathbf{x}'(t)$ in a sufficiently short time interval Δt :

$$\mathbf{u}'(t) = d\mathbf{x}'(t)/dt \approx [\mathbf{x}'(t + \Delta t) - \mathbf{x}'(t)]/\Delta t, \quad (3.3)$$

see figure 3.1(b). In this Chapter, the Lagrangian tracking of a tracer is considered, so that three positions of an individual tracer, rendered at three time instants in sequence, are used to evaluate the acceleration

$$\begin{aligned}
 \mathbf{a}'(t) &= d\mathbf{u}'(t)/dt \\
 &\approx [\mathbf{u}'(t + \Delta t) - \mathbf{u}'(t - \Delta t)]/\Delta t \\
 &\approx [\mathbf{x}'(t + \Delta t) - 2\mathbf{x}'(t) + \mathbf{x}'(t - \Delta t)]/\Delta t^2.
 \end{aligned}
 \tag{3.4}$$

3.2.3 Determination of the measurement error

Regarding the measurement quantities above, the deflection of the light, the position error of the tracers and the velocity measurement error, as well as the acceleration measurement error are investigated.

The deflection of the light ray is represented by the direction difference $\Delta\boldsymbol{\theta} = \boldsymbol{\theta}_f - \boldsymbol{\theta}_0$, a quantity commonly used to evaluate aero-optical effects [69, 83]. When the refractive index is homogeneous, $\Delta\boldsymbol{\theta} = 0$. The position error between the measured position of the tracer and the true position (free of the inhomogeneous refractive index effect) is given by

$$\boldsymbol{\epsilon}_x(t) = \mathbf{x}'(t) - \mathbf{x}(t),
 \tag{3.5}$$

where \mathbf{x}' is the tracer position measured in the inhomogeneous refractive index field and $\mathbf{x}(= \iint \mathbf{g} \cdot \mathbf{w} \, dx_2 dx_3 / (\iint w \, dx_2 dx_3))$ is the tracer position obtained based on the pixel coordinates (\mathbf{g}) in the tracer image rendered from the homogeneous refractive index field.

The velocity error is quantified by the difference between the velocity measured in the inhomogeneous refractive index field \mathbf{u}' and the one in the homogeneous refractive index field \mathbf{u} ,

$$\boldsymbol{\epsilon}_u(t) = \mathbf{u}'(t) - \mathbf{u}(t),
 \tag{3.6}$$

where \mathbf{u} , the ground truth, is obtained through a cubic interpolation over the data of the DNS at the nearest eight neighbor grid points. Similarly, the acceleration measurement error is obtained by,

$$\epsilon_a(t) = \mathbf{a}'(t) - \mathbf{a}(t), \quad (3.7)$$

where \mathbf{a}' and \mathbf{a} are the measured acceleration and the true value, respectively. The acceleration \mathbf{a}' is calculated with equation (3.4) using the measured velocity \mathbf{u}' . The true acceleration is not available in DNS, and it is computed also according to equation (3.4) using the DNS velocity \mathbf{u} instead.

In order to simulate the light rays in the refractive index field, the velocity and the density data of a DNS are used to carry out the numerical experiments.

3.3 Setup of the numerical experiments

3.3.1 Simulated measurement object

The DNS data used for the ray tracing numerical experiments in this study are from the simulations performed by Livescu and Ristorcelli [102]. They implemented a DNS of homogeneous, buoyancy driven turbulence in a cube with periodic boundary conditions (1024 Fourier modes were used along each dimension), and zero-mean velocity and constant mean pressure gradient were imposed. They solved the incompressible Navier-Stokes equations of miscible two-fluid in single phase using a pseudo-spectral method and the Adams-Bashforth-Moulton scheme coupled with a pressure projection method. The equations were made dimensionless with density $\rho_{\text{fluid}} = (\rho_1 + \rho_2)/2$, velocity U_0 and reference length L_0 (leading to the cube edge of 2π), where ρ_1 and ρ_2 correspond to the density of light and heavy fluids, respectively. U_0 and L_0 are not specified explicitly in [102]. The simulation was initialized with randomly distributed blobs of fluids, then turbulence was produced by the different buoyancy of the two fluids. The Reynolds number was $Re = \rho_{\text{fluid}} L_0 U_0 / \mu_{\text{fluid}} = 12500$, where the dynamic viscosity μ_{fluid} was the same for both fluids. The Schmidt number was $Sc = \mu_{\text{fluid}} / (\rho_{\text{fluid}} D_0) = 1$ with

Tab. 3.2: Parameters in the simulation cases.

Case	C0	C1 (air flow)	C2	C3	C4 (water flow)
$K_{\text{fluid}}\rho_{\text{fluid}}$	3.34×10^{-5}	2.82×10^{-4}	3.34×10^{-3}	3.34×10^{-2}	3.34×10^{-1}
Δn_{max}	2.85×10^{-6}	2.40×10^{-5}	2.85×10^{-4}	2.85×10^{-3}	2.85×10^{-2}

the diffusion coefficient D_0 . The density ratio of two fluids was $\rho_2/\rho_1 = 1.105$. Their dataset is available through the Johns Hopkins University Turbulence Database [103]. The dimensionless velocity \mathbf{u} , density ρ and spatial gradients of density $\nabla\rho$ were downloaded for a grid of 512^3 points (1/8 of the full domain) in a dimensionless time interval 0.005 (L_0/U_0) around the time 11.400 (see figure 3.2b for a snapshot of the refractive index field), where the flow turbulent kinetic energy reaches the maximum.

The inhomogeneous refractive index field n is obtained from the dimensionless density ρ via the Gladstone-Dale equation [125],

$$n = K_{\text{fluid}}\rho_{\text{fluid}}\rho + 1, \quad \text{and thus,} \quad \nabla n = K_{\text{fluid}}\rho_{\text{fluid}}\nabla\rho, \quad (3.8)$$

where K_{fluid} is the Gladstone-Dale constant (depending on the fluid), and ρ_{fluid} is the (dimensional) fluid density. In our study, $K_{\text{fluid}}\rho_{\text{fluid}}$ is changed from 3.34×10^{-5} to 3.34×10^{-1} to represent five kinds of fluid, as shown in table 3.2, where C1 and C4 correspond to air ($K_{\text{air}} = 2.3 \times 10^{-4} \text{ m}^3/\text{kg}$, $\rho_{\text{air}} = 1.225 \text{ kg}/\text{m}^3$) and water ($K_{\text{water}} = 3.34 \times 10^{-4} \text{ m}^3/\text{kg}$, $\rho_{\text{water}} = 10^3 \text{ kg}/\text{m}^3$), respectively.

3.3.2 Simulation of the mixing measurement

The numerical experiment was carried out in a cubic domain, the gray box in figure 3.2(a). The flow domain has a length $L(= \pi)$ along each of the three dimensions. A Cartesian coordinate (x_1, x_2, x_3) is set with $x_1 \in [0, L]$, $x_2 \in [0, L]$ and $x_3 \in [0, L]$. Two-dimensional measurements (for x_2 and x_3 components) are simulated at the plane $(x_1 = 0, x_2, x_3)$. The plane $x_1 = 0$ is illuminated with a light sheet with a light wavelength of $\lambda = 532 \text{ nm}$. In the light sheet, 10^5 tracers in size of $10 \text{ }\mu\text{m}$ are distributed homogeneously and randomly, and they are assumed to move within the plane of the light sheet $x_1 = 0$ only. For each individual tracer, \mathbf{r}_0 pointing towards 100×100

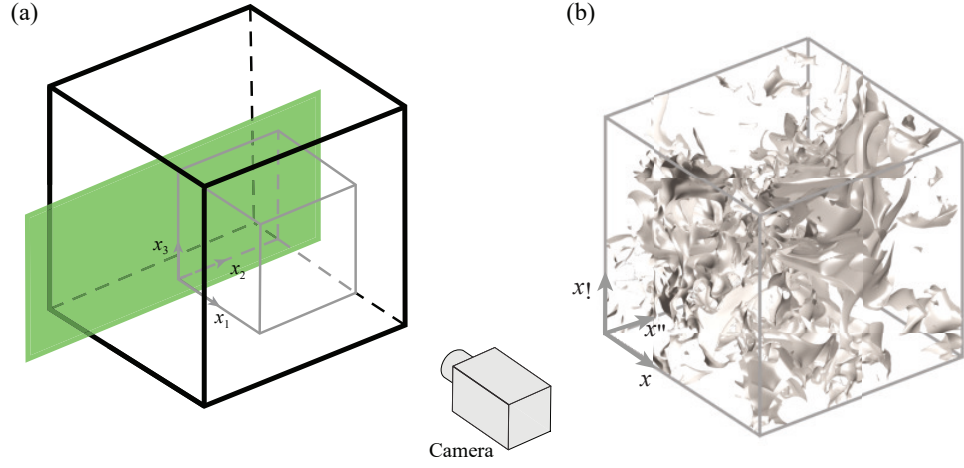


Fig. 3.2: (a) The illustration of the numerical experiment domain (gray box, $L \times L \times L$), part of the DNS domain (black box), where the green layer denotes a light sheet. The camera views the light sheet through the gray box. (b) An example of the isosurface of the refractive index field.

elements with equidistant grids at plane $x_1 = L$ defines the initial direction θ_0 of 10^4 rays. Evaluating 10^4 rays for each of the 10^5 tracers is enough for the simulation of the tracer-based velocimetry [135]. The simulations were carried out in a NVIDIA TITAN V GPU, which has 5120 cores and the memory of 11.26 GB. The simulation of 10^9 rays takes approximately 12 hours.

In this thesis, MATLAB script was developed following the Runge-Kutta algorithm of Sharma et al. [147] to trace each light ray in the refractive index field. In matrix form, the equation (3.1) reads

$$\frac{d^2 \mathbf{R}}{dT^2} = \mathbf{D}, \quad (3.9)$$

where $\mathbf{R} = (x_1, x_2, x_3)$ and $\mathbf{T} = n(\cos\theta_1, \cos\theta_2, \cos\theta_3)$ represent the position and the direction (with angle θ_i of a ray segment in reference to x_i), respectively, and $\mathbf{D} = n(\partial n/\partial x_1, \partial n/\partial x_2, \partial n/\partial x_3)$. The equation (3.9) is solved iteratively in sequence as follows,

$$\begin{aligned} [1] \quad \mathbf{A} &= \Delta\zeta \cdot \mathbf{D}(\mathbf{R}_j), \\ [2] \quad \mathbf{B} &= \Delta\zeta \cdot \mathbf{D}(\mathbf{R}_j + \Delta\zeta \mathbf{T}_j/2 + \Delta\zeta \mathbf{A})/8, \\ [3] \quad \mathbf{C} &= \Delta\zeta \cdot \mathbf{D}(\mathbf{R}_j + \Delta\zeta \mathbf{T}_j + \Delta\zeta \mathbf{B}/2), \\ [4] \quad \mathbf{R}_{j+1} &= \mathbf{R}_j + \Delta\zeta \cdot [\mathbf{T}_j + (\mathbf{A} + 2\mathbf{B})/6], \\ [5] \quad \mathbf{T}_{j+1} &= \mathbf{T}_j + (\mathbf{A} + 4\mathbf{B} + \mathbf{C})/6, \end{aligned} \quad (3.10)$$

where $\Delta\zeta$ is the simulation step size. For each light ray, equation (3.10) is numerically iterated from $\mathbf{R} = \mathbf{r}_0$ and $\mathbf{T}(n, \boldsymbol{\theta}_0)$ at $x_1 = 0$ to the final plane $x_1 = L$. In the iterations, $n(x_i)$ and $\nabla n(x_i)$ at the grids are available, elsewhere linear interpolation using neighboring eight vertices of a cubic volume was used to compute the sub-grid n and ∇n . The simulation step size was tested and $\Delta\zeta = 10^{-4}$ gave converged results. This code was verified by simulations of two standard cases where their analytical solutions are available. The verification simulations and convergence tests are detailed in the next Section 3.3.3.

To render tracer images, ray physical coordinates are projected to image coordinates. The intensity of a light ray, given by the initial direction $\boldsymbol{\theta}_0$ in the Mie scattering, is assumed to be unchanged along its path [16]. The grayscale of each pixel is obtained by summing up the intensity of the rays reaching each pixel. The resulting ‘image’ is then rescaled to a 10-bit dynamic range. A Gaussian filtering operation was performed to produce a tracer image to mimic the diffraction effect of the aperture [135]. A high image resolution of 8192^2 pixel² is used for resolving the small position change of the tracer images as a result of the inhomogeneous refractive index field. The size of tracer image in the non-distorted case (homogeneous refractive index field) is about 10 pixels (which corresponds to about 2-3 pixels in a 2000 pixels² imaging system in practice, which is a typical measurement condition). In a practical imaging system, particle images smaller than one pixel may give larger random error and lead to the known ‘peak locking’ issue (see Chapter 6 in Raffel et al. [134]), while too large tracer images may result in more tracer-tracer overlapping in the images.

In [135], an image of all tracers was rendered, and then algorithms were used to isolate each individual tracer for further analysis. Instead, in this thesis, an image of an individual tracer was rendered and analyzed, then iterations were done over all tracers. In this way, the influence of tracer-segment algorithms on the analysis was avoided, and only the effect of the refractive index field was examined. The truncation of the infinite number of rays in reality to a finite number for a tracer in a simulation produces an artificial effect to the image of a tracer, namely the scattered background noise resulted from the scattered ray destination positions in the image. Hence, a grayscale threshold

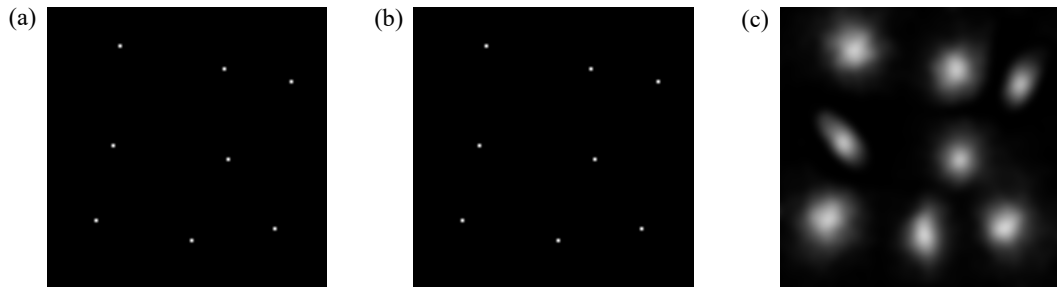


Fig. 3.3: Examples of rendered images of tracers: (a) tracer image rendered in the uniform index field; (b) image of the same tracers for the air flow (C1); (c) image of the same tracers for the water flow (C4).

is used to isolate a tracer from the background noise. For the air flow, the grayscale threshold is 100 for the 10-bit images, while for the water flow this threshold is 500 due to large scatter in high-resolution images. The examples of rendered tracer images are shown in figure 3.3, where the change of the tracer area is small in the air flow (C1), while in the water flow (C4) the tracers blur with large area changes, as visualized in figure 3.3(c).

The simulated measurement was carried out in the following order: The image of a tracer is rendered at a time t , after the ray tracing simulation is performed with the refractive index data which are also from time t . The tracer is then moved to a new position following the DNS velocity in a small time interval $\Delta t = 0.005 (L_0/U_0)$, where the two components of the DNS velocity (u_2 and u_3) are used. The ray tracing simulation of the tracer is performed with the refractive index data from time $t + \Delta t$, after which the image of the same tracer is rendered. When the rendered images of a tracer are available at multiple times, the tracer velocity and the acceleration are obtained following the equation (3.3) and (3.4) with the time interval $\Delta t = 0.005$.

3.3.3 Verification and convergence

In order to verify the code, two standard cases in which analytical solutions are available were simulated. In the first case, a graded-index lens that

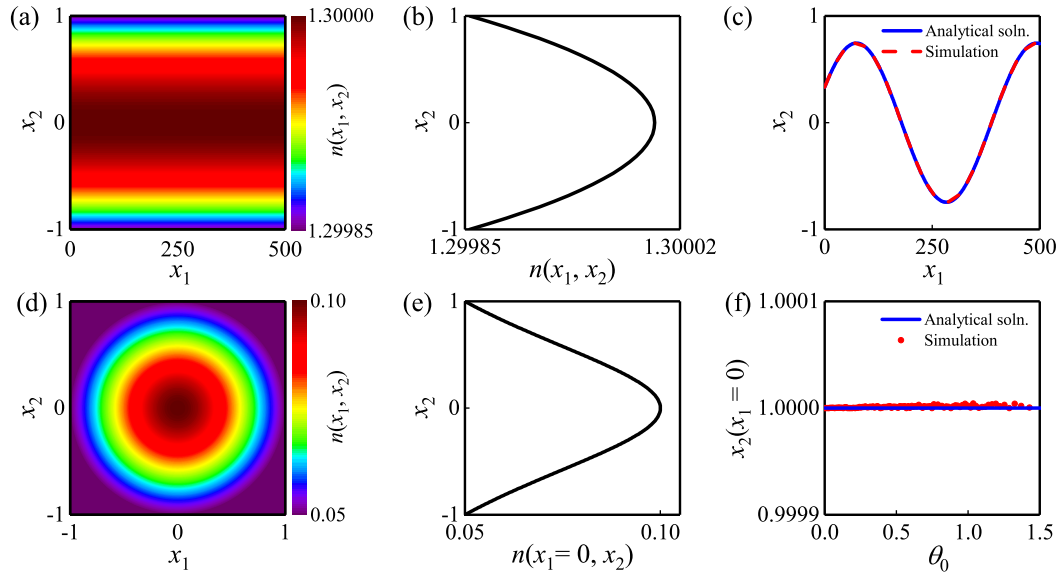


Fig. 3.4: (Color online) Validation of the code: trace rays in a graded-index lens (a)–(c) and a Maxwell’s fish-eye lens (d)–(f). (a) Contours of the refractive index field. (b) A profile of the refractive index. (c) The analytical solution and the simulation result. (d) Contours of the refractive index field. (e) The profile of the refractive index at $x_1 = 0$. (f) The analytical solution and simulation results. Rays are initialized at $(x_1, x_2) = (0, -1)$ with different incident angle θ_0 . The feature of the fish-eye lens gives the destination of the rays at $x_2|(x_1 = 0) = 1$ independent on θ_0 .

is often used in optical coupling assemblies was used as the medium. Its two-dimensional refractive index field is

$$n^2(x_1, x_2) = n_{\max}^2 (1 - 0.01^2 x_2^2), \quad (3.11)$$

where n_{\max} is the peak index (see figure 3.4a–b). The analytical solution of a light ray is

$$\begin{bmatrix} x_2 \\ \theta \end{bmatrix} = \begin{bmatrix} \cos(\alpha x_1) & (1/\alpha)\sin(\alpha x_1) \\ -\alpha\sin(\alpha x_1) & \cos(\alpha x_1) \end{bmatrix} \begin{bmatrix} x_{2,0} \\ \theta_0 \end{bmatrix}. \quad (3.12)$$

In figure 3.4(c) the simulated ray agrees well with the analytical solution, and the maximum difference on x_2 is up to 5×10^{-5} .

In the second case, the light ray in a Maxwell’s fish-eye lens, a special example in the family of Luneburg lenses, was simulated. The refractive index of the fish-eye lens is

$$n(x_1, x_2) = n_{\max}/[1 + (x_1^2 + x_2^2)], \quad (3.13)$$

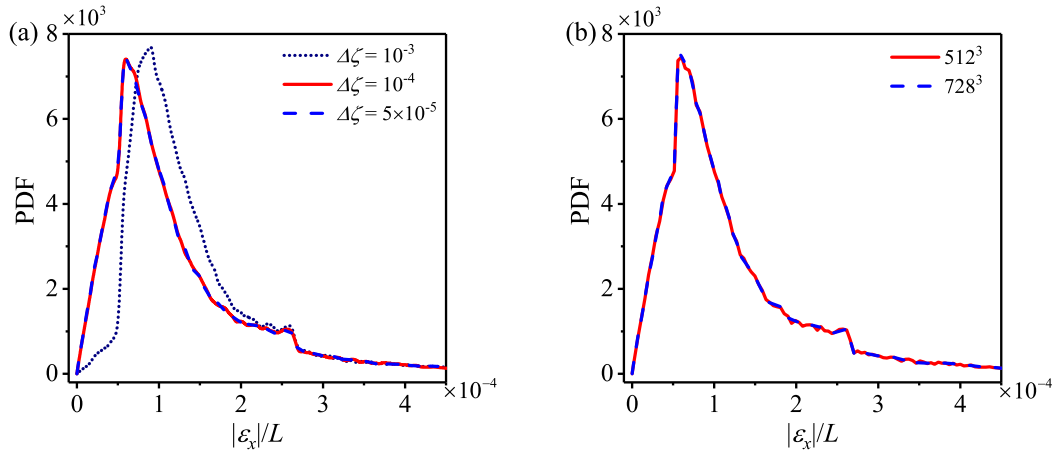


Fig. 3.5: PDF distributions of $|\epsilon_x|$ for the case C1 (air) with different simulation step sizes in Runge-Kutta method (a) and with different grid numbers (b).

as shown in figure 3.4(d)–(e). The mesh grid of the refractive index field has a number of 512^2 , whose refractive index also has an approximate range to the water flow case ($\Delta n_{\max} \approx 5 \times 10^{-2}$). In a fish-eye lens, a light ray leaving a point on the lens border ends up at a point on the opposite border. The start and the end points are at the same distance from the lens center [107]. Whether this unique characteristic can be reproduced is sensitive to the code precision, thus it is often used for code verification (e.g. in [135]). In figure 3.4(f), the light rays from $(x_1, x_2) = (0, -1)$ with different incidence angle θ_0 all end up at $(x_1, x_2) = (0, 1)$. The maximum difference on $x_2(x_1 = 0)$ is up to 2×10^{-6} .

The convergence tests on the simulation time step (in RK iterations) and grid numbers of the refractive index field were carried out. In figure 3.5, it showed that the PDF distribution of tracer position error in air flow. It was found that the statistical results with $\Delta t = 10^{-4}$ and $\Delta t = 5 \times 10^{-5}$ overlap with each other, suggesting that $\Delta t = 10^{-4}$ can give converged simulation. Regarding the grid numbers, the PDF of the results from grid number 512^3 and that from a finer mesh (728^3) of the refractive index field are collapsed, showing that the grid number 512^3 is sufficient. Thus, the time step $\Delta t = 10^{-4}$ and the mesh number (512^3) were employed in our simulations. Here, it should be noted that the original refractive index field with a fine mesh (1024^3) was downloaded from the JHU turbulence database [103] with their provided 6th order Lagrangian interpolation in space. But this refractive index field needs a large memory for the GPU card. Our available GPU cards hardly

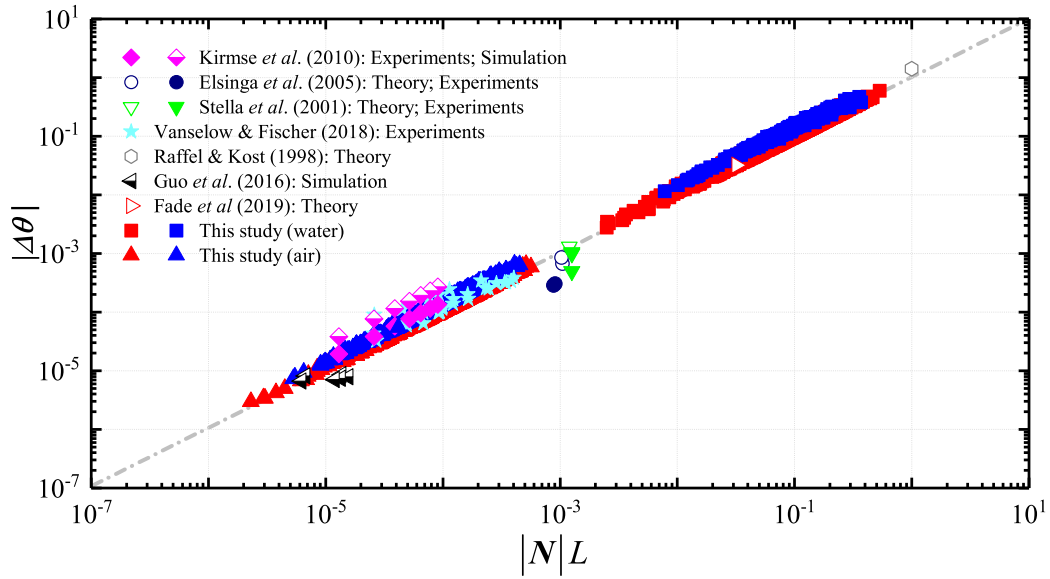


Fig. 3.6: Ray deflection $|\Delta\theta|$ against dimensionless spatial gradients of the refractive indices $|N|L$. For the data of previous studies, N was obtained by Δn_{\max} divided by n and by a characteristic length, and these three values were extracted from each corresponding reference with our best estimation. Δn_{\max} is listed in table 3.1. The data of $0 \leq |\theta_0| \leq 0.6$ are in blue symbols and those of $0.6 < |\theta_0| \leq 0.9$ are in red. Note that only 4000 data points are plotted to avoid oversizing the figure.

handle a so large refractive index field during the simulations. Thus, based on the fine refractive index field (1024^3 mesh), the interpolated refractive index field with a mesh (768^3) was used to test the convergence of the grid numbers.

3.4 Results of the mixing measurement

Five cases were investigated as summarized in table 3.2. Because air and water flow are commonly used in most studies, the results of these two cases are shown and discussed in more detail. The measurement errors are quantified over four variables: deflection of light rays, position errors of tracers in the image, velocity measurement errors and acceleration measurement errors.

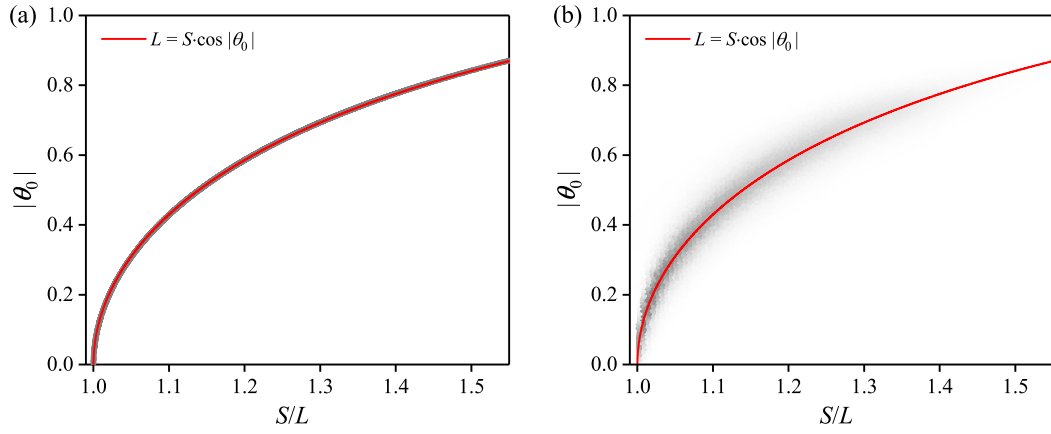


Fig. 3.7: The relationship between the length of the light trajectory S and initial incidence angle $|\theta_0|$: (a) air flow (C1) and (b) water flow (C4). The gray dots denote the sample points, and the grayscale is the two-dimensional probability density function of $|\theta_0|$ and S/L , where darker corresponds to larger value of PDF.

3.4.1 Light deflection

The light deflection $\Delta\theta = \theta_f - \theta_0$ can be written as $\Delta\theta = \int [\nabla n/n - (1/n) \cdot (dn/ds) \cdot (dr/ds)] ds$, when the integration is taken along the light trajectory with its length S in equation (3.1). It can be further written as

$$\Delta\theta = \mathbf{N} \cdot S, \quad \text{with} \quad \mathbf{N} = \left(\frac{\nabla n}{n} - \frac{1}{n} \frac{dn}{ds} \frac{d\mathbf{r}}{ds} \right)_{\mathbf{r}=\xi}, \quad (3.14)$$

according to *Lagrange mean value theorem* at a point ξ in the ray curve. Here \mathbf{N} is determined by the complex ray curve *inside* the flow, and it is difficult (or impossible) to obtain in the non-numerical experiments. The magnitude of the light deflection is $\log(|\Delta\theta|) = \log(|\mathbf{N}|S) = \log(|\mathbf{N}|L) + \log(S/L)$ (according to equation 3.14), where L refers the depth of photon path along the x_1 direction.

Figure 3.6 shows the light deflection obtained in the simulation and that extracted from previous studies, which are summarized in table 3.1. The light deflection is found to increase linearly with the spatial gradients of the refractive index field, in agreement with previous studies. The linear relation can be seen between $|\Delta\theta|$ and $|\mathbf{N}|L$ (in logarithmic-logarithmic axes) along a gray dash-dot line. The present data follow the $|\Delta\theta| - |\mathbf{N}|L$ trend, and shift as the incidence angle $|\theta_0|$ increases from 0 – 0.6 (red symbols) to 0.6 – 0.95

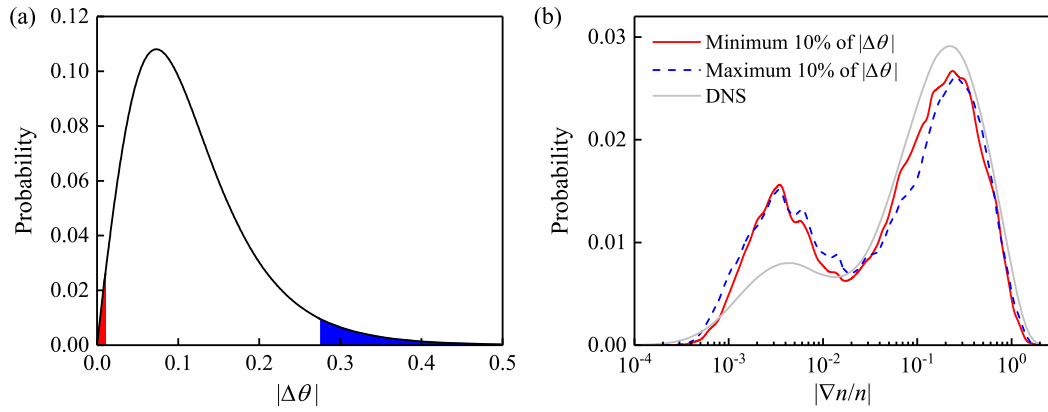


Fig. 3.8: (a) Probability distribution of ray deflection angles $|\Delta\theta|$ (in unit of rad), where the maximum 10% and the minimum 10% of the data are marked as blue and red, respectively. (b) Probability distribution of spatial gradients of the refractive index $|\nabla n/n|$ which the rays pass through, while the DNS data on all grids are shown as reference.

(the blue). Such a shift indicates the link of $|\theta_0|$ to S/L mentioned above. Figure 3.7 shows that S/L can be represented by $1/\cos|\theta_0|$, even for the case of the water flow (C4) where the refractive index difference is as large as 10^{-2} .

From equation 3.14, the cumulative deflection angle is decided by the integral of refractive index gradient. The relationship between deflection angle and refractive index distribution was also investigated. Hence, figure 3.8 demonstrates the PDF distribution of refractive index through which the large deflection angle and small deflection rays propagate. Compared to the original DNS refractive index distribution, the PDF distribution is similar. This means the final position of rays and deflection angles of rays are mainly dependent on the sequence (integral) of refractive index gradient along the paths rather than only gradient along path lengths.

3.4.2 Error of tracer position in images

The effect of the inhomogeneous refractive index field on the imaged tracers has two aspects: one is the shape/area change, another one is the position error of the imaged tracer.

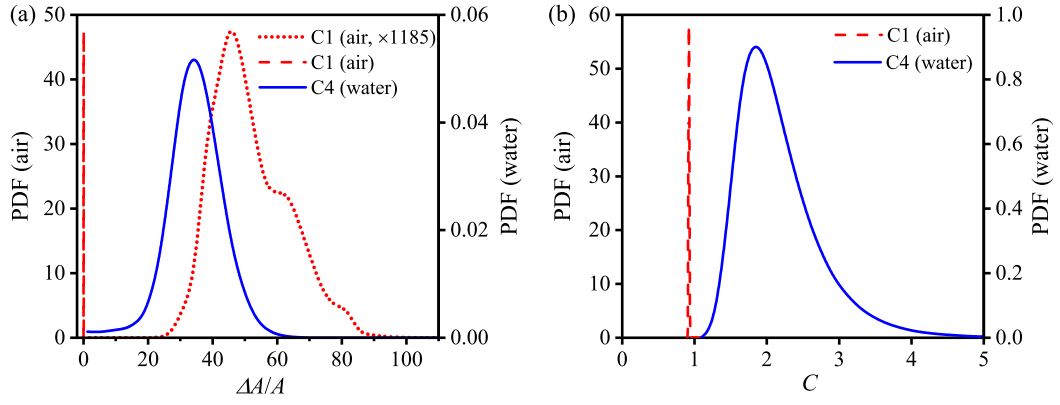


Fig. 3.9: (a) PDF distribution of change of tracer area ΔA , where A is the tracer area in a uniform refractive index field. The $\Delta A/A$ of air was amplified by $K_{\text{water}}\rho_{\text{water}}/(K_{\text{air}}\rho_{\text{air}}) \approx 1185$ to match the data range of the water for comparison, see the red dotted line. (b) PDF distribution of the circularity C of the imaged tracers.

The former is exemplified in figure 3.3. The tracer position is subjected to the deformation of the rendered tracer shape. Here the geometrical properties of the rendered tracer are discussed. The area change of an imaged tracer is $\Delta A = A' - A$ (in pixel^2), where A' denotes the area in an inhomogeneous refractive index field and A the case in a uniform index field. The shape of imaged tracers was quantified by the roundness of an imaged tracer, i.e., circularity $C = P^2/(4\pi A')$, where P is perimeter of the tracer. When $C \approx 1$, the tracer is a dot in the image, whereas the tracer is elongated if $C \gtrsim 1$ (see figure 3.3). In the air flow (C1), the tracer area change is small with a peak around 0.05, as visualized in figure 3.3(b). In the water flow (C4), $\Delta A/A$ is significant (with a peak around 38), and strong blurring of tracers can be seen in images. For the shape of imaged tracers, the effect of the refractive index in the air flow (C1) is trivial and imaged tracers are close to dots. However, in the water flow (C4), the tracers are strongly elongated to ellipses, given that C has a distribution with the peak around 2 and the maximum about 6. Regarding to the position error $|\epsilon_x|$, the probability density function (PDF) of $|\epsilon_x|$ is calculated. As shown in figure 3.10, PDF curves of five cases have similar shapes, and each curve has a peak. The peaks shift towards larger $|\epsilon_x|$ from case C0 to C4. The data at the PDF peaks are extracted and shown in the figure inset, and $|\epsilon_x|$ at the PDF peaks shows an increasing trend with $K_{\text{fluid}}\rho_{\text{fluid}}$. Specifically, for the air flow (C1), the magnitudes of position error are up to $\mathcal{O}(10^{-4}L)$, about 1/10 of the tracer diameter in the images.

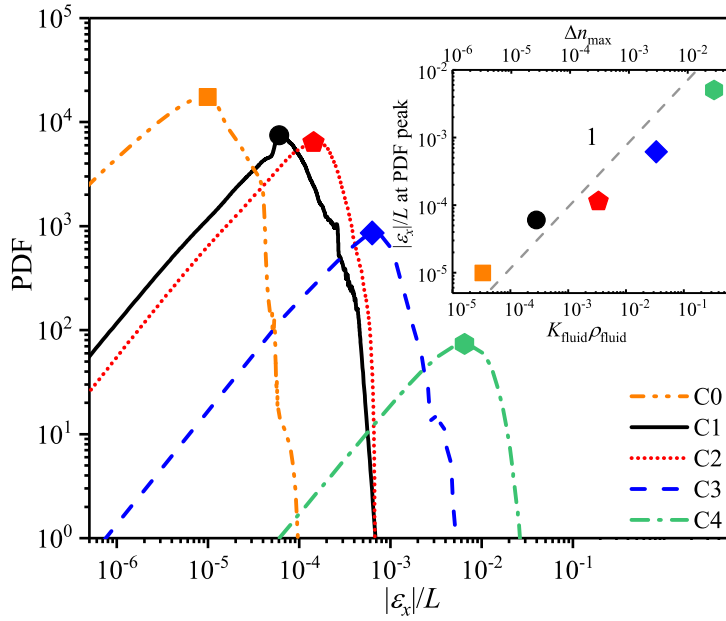


Fig. 3.10: PDF distribution of the magnitude of position error $|\epsilon_x|$ for all five cases in this study. The symbols mark the PDF peaks. The inset shows $|\epsilon_x|/L$ at the PDF peaks versus $K_{\text{fluid}}\rho_{\text{fluid}}$ (bottom horizontal axis) and Δn_{max} (top horizontal axis).

For the water flow (C4), the magnitudes of position error reach $\mathcal{O}(10^{-2}L)$, corresponding to $\mathcal{O}(10)$ of the diameter of the imaged tracers.

The ray deflection distance $\epsilon_r = \mathbf{r}' - \mathbf{r}_0$ (sketched in figure 3.1a) can be obtained from an integration to the equation (3.14). $|\epsilon_r|$ can be approximated to be $|Nl| \cdot S$ with a length l according to the *Lagrange mean value theorem*, and $|Nl|$ could be interpreted as the refractive index mismatch level along the light path. I found that $|\epsilon_r|$ depends on $|Nl|$ rather than $|N|$ nor l individually. The ray deflection $|\epsilon_r|$ shows strong dependence on $|Nl|$ and $|\theta_0|$ (see figure 3.11). Given that a tracer in the image is resulted from all the rays scattered from a tracer, the position error of the tracer $|\epsilon_x|$ is hence assumed to take the same form as $|\epsilon_r|$,

$$|\epsilon_x| \approx |\widetilde{Nl}| \cdot \widetilde{S}/L \cdot L, \quad (3.15)$$

where $\widetilde{(\cdot)}$ denotes an averaging operation over all \mathbf{r}' for one tracer (see figure 3.1b). As shown in figure 3.12, the tracer position error $|\epsilon_x|/L$ increases linearly with $|\widetilde{Nl}|$ along a dashed line, when $|\theta_0|$ is close to zero (reaching the paraxial assumption). When $|\theta_0|$ is increased, the slope of the curve is

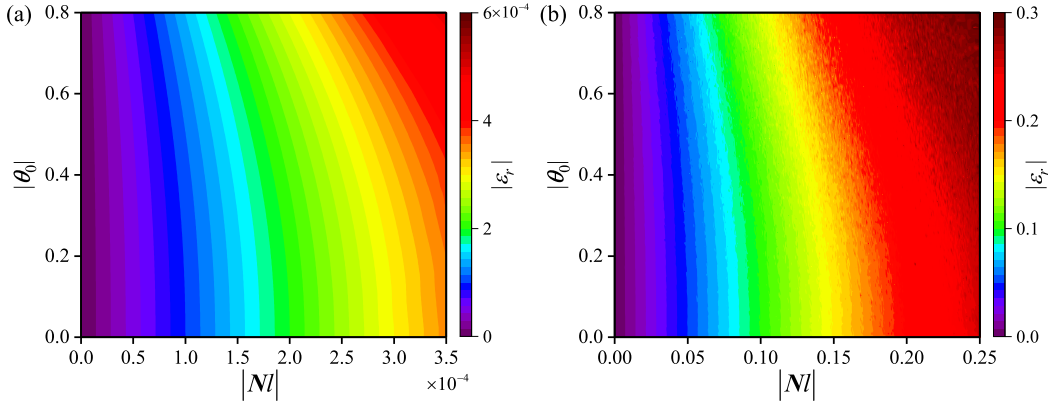


Fig. 3.11: The distribution of ray deflection distance $|\epsilon_r|$, relative difference of the refractive index $|Nl|$ and initial incidents $|\theta_0|$: (a) air and (b) water.

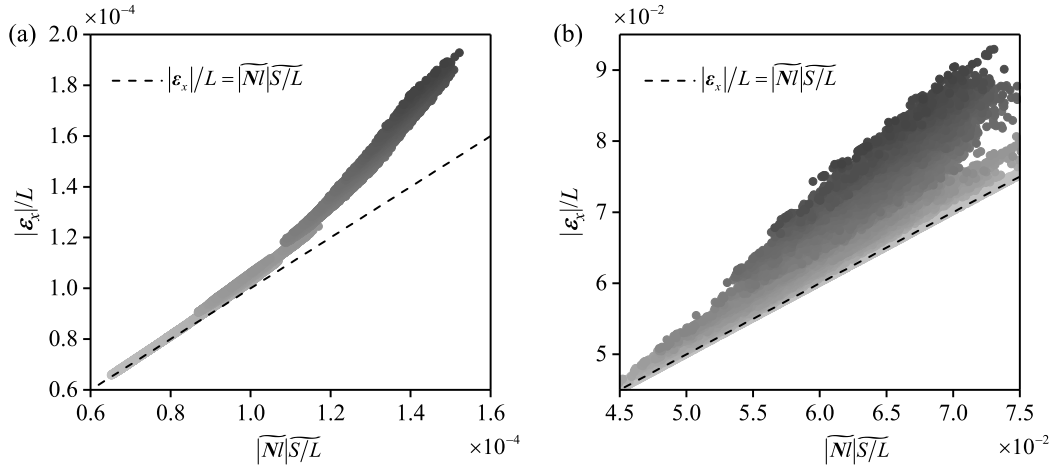


Fig. 3.12: Tracer position error $|\epsilon_x|$ against the relative difference of the refractive indices $|\widetilde{N}l|$: (a) air flow (C1) and (b) water flow (C4). The dots are grayed with the incidence angle $\widetilde{\theta}_0$, the larger $\widetilde{\theta}_0$ the darker dots.

increased. This suggests that $|\epsilon_x|/L \approx |\widetilde{N}l| \widetilde{S}/L \approx |\widetilde{N}l|/\cos|\widetilde{\theta}_0|$ (recall that $L \approx S \cdot \cos|\theta_0|$ shown in figure 3.7).

Based on the above analysis, the position error $|\epsilon_x|$ suggests the approximate origination from three aspects: (1) $|\widetilde{N}l|$, which can be referred to the relative difference of the refractive indices (mismatch level) along the light path; (2) $\widetilde{\theta}_0$, which can be approximately interpreted as the angle of a camera viewing the tracer; (3) L , the depth of the index field with which a camera views the tracers.

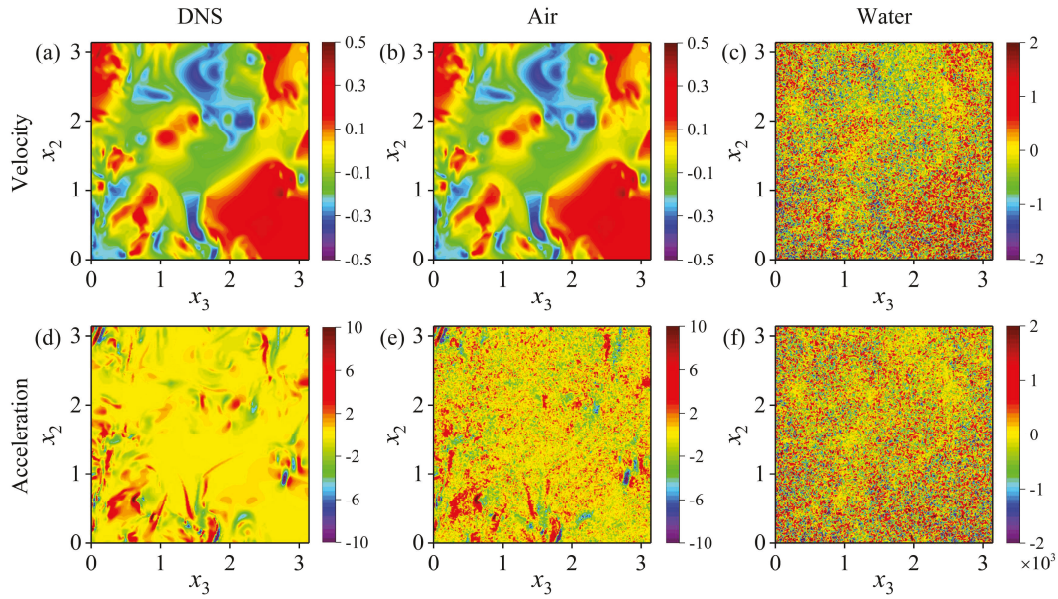


Fig. 3.13: Colormap of the flow velocity (u_3) and the acceleration (a_3) at time $11.4 (L_0/U_0)$ from the DNS (a,d), the air flow case (b, e) and the water flow case (c, f). The velocity and acceleration are made dimensionless with U_0 and U_0^2/L_0 , respectively, as introduced in Section 3.3.1.

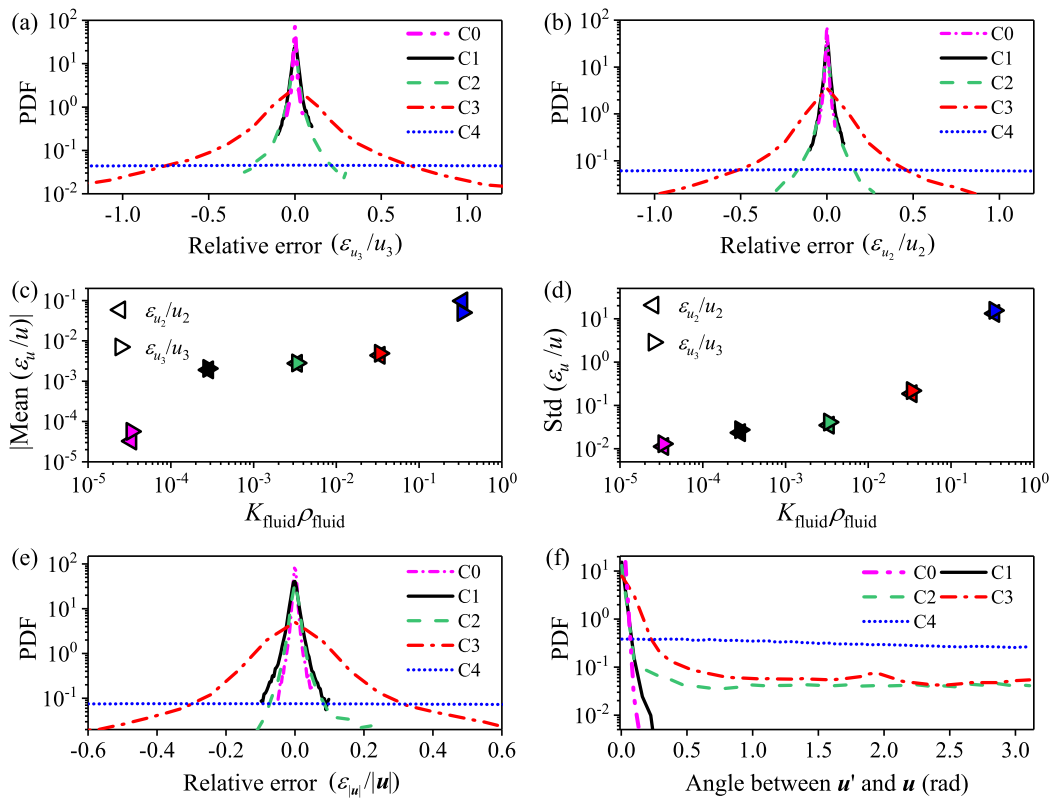


Fig. 3.14: PDF distribution of the relative velocity error ϵ_{u_3}/u_3 (a), ϵ_{u_2}/u_2 (b), the mean of ϵ_u/u (c), and the corresponding standard deviation (d), the magnitude of the relative error $\epsilon_{|u|}/|u|$ (e) and the angle between u' and u (f). In (c) and (d) the filled colors in symbols correspond to C0 and C4 as in (a).

3.4.3 Error of velocity measurement

The contours of the velocity component u_3 from the DNS and the simulated measurements for the case C1 and C4 at the same time instant are shown in figure 3.13(a–c) as examples of visualization. The DNS velocity \mathbf{u} is obtained from the cubic interpolation of the DNS data in the $x_2 - x_3$ plane, and it is taken as the true for reference. The effect of the interpolation scheme on the true value is negligibly small. The velocity contours between the DNS and the air flow (C1) are visually similar, while the velocity contours in the water flow (C4) are fragmented in small scales and contaminated with large errors. The velocity component u_2 has similar results (not shown).

To quantitatively assess the measurement error of the velocity, the PDF statistics is performed for u_3 and u_2 and their corresponding magnitude and vector direction, as shown in figure 3.14. The PDF of the relative velocity error ϵ_{u_3}/u_3 has a symmetric distribution with its peak close to zero. When $K_{\text{fluid}}\rho_{\text{fluid}}$ is increased, the PDF peak decreases together with broader PDF tails. The PDFs of ϵ_{u_2}/u_2 have similar distributions as ϵ_{u_3}/u_3 . The corresponding mean and standard deviation of ϵ_{u_3}/u_3 , taken as the *relative systematic measurement error* and *relative random measurement error*, respectively, are shown in panel (c) and (d). The systematic error increases from about 5×10^{-3} % to about 10 % as $K_{\text{fluid}}\rho_{\text{fluid}}$ is increased. The random error increases from 1 % to about 2000 % as $K_{\text{fluid}}\rho_{\text{fluid}}$ is increased. The ϵ_{u_2}/u_2 has nearly the same systematic and random errors as ϵ_{u_3}/u_3 . In addition to the statistics of the velocity components, the relative errors of the velocity magnitude is also examined, and the PDFs of $\epsilon_{|\mathbf{u}'|}/|\mathbf{u}'|$ have very similar distributions as the components (see panel (e)). The angle between \mathbf{u}' and \mathbf{u} is obtained by $\cos^{-1}[(\mathbf{u}' \cdot \mathbf{u})/(|\mathbf{u}'||\mathbf{u}|)]$, and its PDF has a peak at zero for C0. When $K_{\text{fluid}}\rho_{\text{fluid}}$ is increased, the PDF becomes flatter, especially for the water flow (C4), as shown in figure 3.14(f).

Regarding the commonly used fluids, air and water, the systematic and the random measurement error of the air flow (C1) is small to be approximately 0.2 % and about 2 %, respectively, and the flow direction is well measured (see figure 3.14f). Thus, the effect of the inhomogeneous refractive index might be tolerable (for the turbulent flow in this Chapter). For the water

flow (C4), the systematic error reaches 10 %, a noticeable level, while the random error reaches about 2000 % which demonstrates that the velocity measurement is completely contaminated, so that the measured velocity can be concluded to be questionable, at least for the turbulent flow considered in this Chapter. Note that $\Delta n_{\max} \sim 10^{-5}$ is around the minimum resolution of a portable refractometer, which can be used in refractive index matching techniques to reduce the measurement errors caused by the refractive index difference [181, 43, 7].

The measurement error of the velocity originates from the position error of the tracer due to the light deflection. Studying this error propagation chain, the Lagrangian velocity error is derived (with details in 6.1) and can be approximately ascribed to $\partial^2 n / \partial t \partial \mathbf{x}$ and $\mathbf{u} \partial^2 n / \partial \mathbf{x}^2$, and which the dominant is in variety of flows needs investigations in future. The latter term refers to the advection of the refractive index inhomogeneity, and the former term illustrates that the evolution rate of the refractive index field to the velocity field is a key factor for the velocity measurement error. This evolution rate is often flow dependent. When Taylor's frozen-flow hypothesis is approximately valid, $\partial n / \partial t \approx \mathbf{u} \cdot \partial n / \partial \mathbf{x}$, and the two error sources turn to be a single one, either $\partial^2 n / \partial t \partial \mathbf{x}$ or $\mathbf{u} \partial^2 n / \partial \mathbf{x}^2$. Note that Elsinga et al. [51] derived the PIV velocity measurement error in an Eulerian scheme, i.e.

$$\epsilon_u = [\nabla \epsilon_x(t)] \mathbf{u}(t) - [\nabla \mathbf{u}(t)] \epsilon_x(t), \quad (3.16)$$

where the first part is termed as 'the direct velocity error', whereas the second is termed as 'the contribution of the position error to the velocity error'. In their equation, the temporal evolution of the refractive index field is not explicitly given. However, the factors causing the velocity measurement error in Elsinga et al. [51] are consistent with our results, as shown in Appendix 6.1.

3.4.4 Error of acceleration measurement

The contours of the measured acceleration in the air flow (C1), shown in figure 3.13(e), are visually similar to the pattern of the DNS data (see figure 3.13d), although piecemeal 'noise' is evidenced. However, for the water

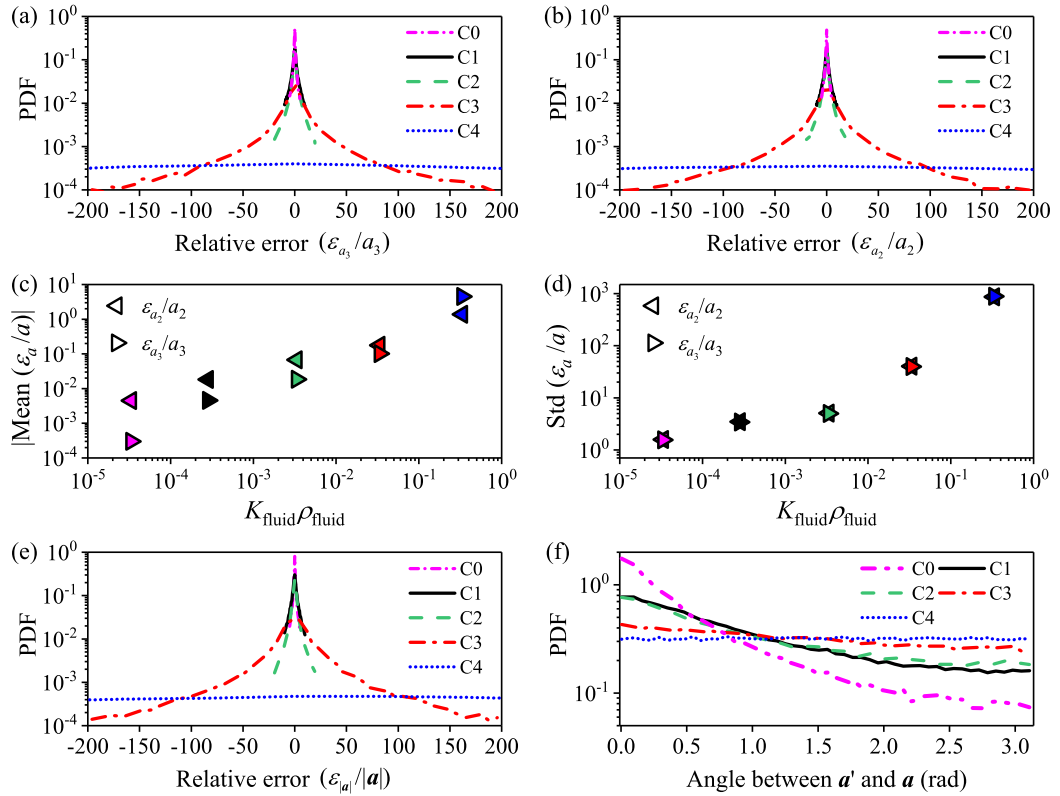


Fig. 3.15: PDF distribution of the relative velocity error ϵ_{a_3}/a_3 (a), ϵ_{a_2}/a_2 (b), the mean of ϵ_a/a (c) and the corresponding standard deviation (d), the magnitude of the relative error $\epsilon_{|a|}/|a|$ (e) and the angle between \mathbf{a}' and \mathbf{a} (f). In (c) and (d) the filled colors in symbols correspond to C0 and C4 as in (a).

case (C4), the contours are significantly contaminated, see figure 3.13(f). The PDF distributions of the relative acceleration error (ϵ_{a_3}/a_3) are symmetric with their peaks close to zero, as shown in figure 3.15(a). When $K_{\text{fluid}}\rho_{\text{fluid}}$ is increased, the distribution peak decreases and the width of the distribution tails becomes broader. The PDFs of ϵ_{a_2}/a_2 have similar distributions as ϵ_{a_3}/a_3 . The relative systematic and random errors of the acceleration measurements are evaluated. The systematic error, quantified by the mean of ϵ_a/a , increases from about 0.5 % to about 100 % for a_2 and from about 2×10^{-2} % to about 500 % for a_3 , respectively, as $K_{\text{fluid}}\rho_{\text{fluid}}$ increases. The random error, quantified by standard deviation of ϵ_a/a , is found to increase from about 100 % to about 10^5 % for both a_2 and a_3 as $K_{\text{fluid}}\rho_{\text{fluid}}$ increases. The PDFs of $\epsilon_{|\mathbf{a}'|}/|\mathbf{a}'|$ have very similar distributions as the components (see panel (e)). The angle between \mathbf{a}' and \mathbf{a} is shown in panel (f). When $K_{\text{fluid}}\rho_{\text{fluid}}$ is increased, the PDF becomes flatter, as shown in figure 3.15(f).

For the case of the air flow (C1), the systematic and the random error of the flow acceleration are about 1 % and 300 %, respectively. For the case of the water flow (C4), the systematic and the random error are about 500 % and 10^5 %, respectively. Following the same derivation method for the velocity measurement errors, we find that ϵ_a is ascribed to $\partial^2 n/\partial \mathbf{x} \partial t$, $\mathbf{u} \partial^2 n/\partial \mathbf{x}^2$, $(\partial \mathbf{u}/\partial t)(\partial^2 n/\partial \mathbf{x} \partial t)$ and $(\partial \mathbf{u}/\partial t)(\partial^2 n/\partial \mathbf{x}^2)$ (see details in Appendix 6.1).

In practice, measurements of flow acceleration are made in three dimensions [144]. In our study, we consider the tracers moving only in the two-dimensional plane ($x_1 = 0$) for simplicity. The statistics of two components of the accelerations may be different from those of three components, but the three-dimensional relative error of acceleration is expected to be on the same level of $\mathcal{O}(1)$ to $\mathcal{O}(10^3)$ for the range of $K_{\text{fluid}}\rho_{\text{fluid}}$ considered here. For the turbulent flow considered in this Chapter, the experimental measurements of the flow acceleration give unrealistic results, even when the maximum refractive index difference is about 10^{-5} . This finding is from this specific turbulent flow, but is expected to imply comparable measurement errors in other flows with similar maximum refractive index difference and similar turbulence levels.

3.4.5 Optical errors in the T-mixer

When the PLIF technology is employed to measure the concentration field in the present setup (see Section 2.2.3), the concentration of a fluorescence dye (e.g., Rhodamine 6G or Rhodamine B) usually is lower than $100 \mu\text{g}/\text{l}$ for a high-quality calibration [181, 34]. In this concentration range, the effects of the fluorescence dye concentration on the refractive index of the liquids are so small ($< \mathcal{O}(10^{-6})$) that the refractive index difference (smaller than case C0) is difficult to be detected by the present refractometer [3]. As estimated in this study (see figure 3.10), with the camera of 2000^2 pixel^2 resolution, the induced optical errors in images are even smaller than subpixel. Thus, the position error of mixing patterns in images has the subpixel level error and is even smaller, which is difficult to be distinguished with the noise of the illumination. The temperature difference mentioned in Section 2.3.5 is about 0.54 degrees between channel walls (see figure 2.20b). Through the Gladstone–Dale relation, the maximum refractive index difference is 6.68×10^{-5} , which results in the maximum tracer position errors of about 0.02 pixel with the employed camera configurations (roughly estimated by the results in figure 3.10 or [51]) for PIV results. This measurement error is smaller than subpixel. Meanwhile, during the experimental time, the Rayleigh number is $\mathcal{O}(10^5)$ and there is no strong convection. The thermal effect keeps steady and the refractive index field is also steady for a long time, which does not bring in a more complex influence on the velocity measurement error. Therefore, the measurements in the last Chapter are assumed to be trustworthy.

3.5 Summary and recommendations

Image quality is crucial for the measurement quality of tracer-based velocimetry techniques. When the refractive index field inside a flow is inhomogeneous, tracers in images are blurred and have errors in position, which leads to measurement errors of the flow velocity and the acceleration, respectively. This is particular an issue when the refractive index field is three-dimensional and temporally changes, as in turbulent flows.

To evaluate the measurement errors in such flows, the distribution of the index field of the flow must be taken into account. In this Chapter, ray tracing simulations were carried out to obtain light rays in a single-phase three-dimensional turbulent flow in a simulated experiment. The flow measurement error was investigated regarding every single tracer inside a three-dimensional index field. This field was obtained by converting the DNS density data of the turbulent flow, where two fluids in the same phase mix with each other. Five cases (C0 to C4) were investigated, with the maximum differences of the refractive indices ranging approximately from 10^{-6} to 10^{-2} .

The measurement errors influenced by the inhomogeneous refractive index field are quantified over four variables: deflection of light rays, position errors of tracers in the image, velocity measurement errors and acceleration measurement errors. The analysis of the ray tracing simulation data is in reference to the DNS data of the turbulent flow. The position error of a tracer is found to increase when either the non-dimensional refractive index difference (mismatching level) or the camera viewing angle is increased. This suggests that in preparation of a PTV measurement, the measurement can be refined by reducing the depth of the light rays through the flow field if possible, and/or by reducing the viewing angle of cameras towards the field-of-view.

Regarding the errors of velocity and acceleration measurements in the turbulent flow considered here, for the case of air flow, the relative systematic measurement error is about 0.2 % in velocity and about 1 % in acceleration, respectively, and this is tolerable (for the turbulent flow considered). The relative random measurement error is about 2 % in velocity and about 300 % in acceleration, respectively, i.e., noticeable larger than the systematic error. While for the water flow, the relative systematic error is about 10 % in velocity and about 500 % in acceleration, respectively. The relative random error is about 2000 % in velocity and about 10^5 % in acceleration, respectively. This clearly shows that, compared with the velocity measurement, the flow acceleration measurement in the water flow is significantly deteriorated to make the measurements untrustworthy (for the turbulent mixing flow considered). The errors of the velocity and the acceleration are found to be

associated with the spatial and spatio-temporal gradients of the refractive index. The latter is controlled by the ratio of velocity-scalar diffusion, whose effects are worth of investigation in the future.

The measurement errors in this work are studied in the framework of PTV. Since PTV and PIV share the same working principle, the findings here are expected to hold for the PIV measurements, which include an averaging effect among the tracer motions within an interrogation window [182]. The PLIF technology or other optical technologies based on the geometrical optics have a similar problem as well. In the mixing processes, if the liquids mix with a large refractive index difference, for example, water and ethanol, the refractive index difference is in the order of 3×10^{-2} (case C2 and C3), and the optical errors in images are in the order of 10 pixels with the camera of 2000^2 pixel² resolution, which should be considered when the optical measurements are implemented. The ray tracing simulation method could be applicable for this mixing process to evaluate the influence of the inhomogeneous refractive index field on the measurement error of PIV and PLIF and further revise the measurement results (e.g., [51]). On contrary, the optical errors in images can also be utilized to reconstruct the refractive index field (and density field through equation 3.8) by the BOS technique [158, 119], which provides a perspective and a method to understand the mixing evolution in time and space. When the refractive index difference is about 0.334 (case C4), an extreme case, namely air–water mixing, happens at the interface, which plays an important role in the river, lake and ocean mass transfer processes. In an analogy of the BOS technique, in the next Chapter, the refraction at the interface of these two-phase fluids is utilized to reconstruct the gas-liquid mixing interface combined with virtual displacements of markers.

A measurement method for the gas-liquid mixing interface

4.1 Gas-liquid interface measurements

Gas-liquid mixing occurs in the interface between water and air in open channels, rivers, as well as lakes and oceans. Transport across the interface is related to turbulent mixing and surface waves (e.g. wave slopes) near the interface [9, 13, 185, 95]. Jähne and Haußecker [80] summarized that short/long wind-driven waves enhance the mass transfer, but the detailed mechanisms for the enhancement are not fully understood and fundamental investigations in simple setups are needed. The large difference in the air and water refractive indexes brings difficulties in implementing optical techniques to measure the velocity (see Chapter 3) and the surface-wave motion. Many quantitative optical imaging measurement methods of the surface topography (surface height) have been developed and tested in laboratory experiments, because of their non-intrusive nature. They are summarized in the following.

One imaging methodology associates the topography of the free surface with light absorption in the liquid. Given that image magnification is independent of surface height, Jähne et al. [81] used a telecentric optical system to measure the surface height, which is a function of the light absorption rates from light-emitting diodes (LEDs) with red and near-infrared lights. Aureli et al. [6] used a camera with two charged-coupled devices (CCDs) including a monochrome near-infrared sensor in order to implement the surface measurements with the working principle of light absorption. PLIF with a laser sheet has also been used to capture the profiles of the free surface [47, 4]. A fast-scanning of a laser sheet can be used to obtain and reconstruct the surface topography in two dimensions [167]. The scanning needs to be fast enough so that the surface structure can be approximately assumed

to be frozen. Light reflection can also be used for surface measurements. For example, the slope of two-dimensional surfaces can be measured with a polarimeter by correlating the surface orientation with changes of light polarization [186]. This technique can be used not only in laboratory but also in rivers with unpolarized skylight or moon-glade [186, 173]. Alternatively, symbol patterns and fringe patterns are projected onto the surface, and the deformation of the patterns due to the surface topography can be exploited for the surface measurements [162, 31, 76]. The intensity of the light reflection is crucial for the measurement accuracy, and additives mixed with the liquid (water) are employed to improve the light reflection at the surface.

The refraction between air and water surface and its optical displacements can be utilized to reconstruct the surface topography. Kurata et al. [96] used a camera to capture a reference and a refraction image of a striped grating, which was placed below a shallow water channel. When the water surface had ripples, the imaged grating was virtually displaced with respect to the still, horizontal water surface, due to the changed light refraction. In their method, the topography of the free surface is obtained from the virtual displacements. The surface height can also be obtained provided that the height of a reference surface point is known. In their flow, there is a point where the surface height is nearly unchanged in time, and they used the height at this point as the reference height to reconstruct the surface depth from the topography data. Fouras et al. [57], Moisy et al. [115] and Ng et al. [118] further developed this method by replacing the grating with random dot patterns, so that optimized cross-correlation particle-image-velocimetry (PIV) algorithms can be used to compute the virtual displacements precisely. The advantages of refraction methods are the use of low-cost illumination, simple optical configuration and a single camera. Despite their simplicity and precision, a drawback of these methods is that a reference height is needed to reconstruct the height of the surface from the surface topography. In some situations, the liquid depth is not known and the method cannot be applied. Morris [116] and Gomit et al. [62] used two or more cameras to obtain stereoscopic views of the same pattern. They could directly obtain the topography and the height of the free surface by matching the surface orientation at each surface point from the measurements of multiple cameras [116] (see table 4.1). However, using multiple cameras raises the hardware

Tab. 4.1: A brief list of refraction methods for free surface measurements.

Ref.	Quantity of camera	Object & pattern	Illumination	Measurability of liquid height
[190]	1	Random colored blocks	Halogen light	Yes, with reference height
[35]	1	Random colored blocks	–	Yes, with reference height
[116]	2	Checkerboard	LED	Yes
[81]	1	Gridded dots	LED	Yes, with complex telecentric illumination
[57]	1	Random dots	LED	Yes, with reference height
[115]	1	Random dots	LED	Yes, with reference height
[62]	3	PIV tracers	Laser sheet	Yes
[6]	1	Random colored blocks	LED	Yes, with coupled RGB Bayer array and Monochrome sensor
[52]	1	Checkerboard	LED	Yes, with parametric surface model
[90]	2	Random dots	bichromatic LED	Yes, with reference height and telecentric lens

costs, results in more time-consuming calibration of the camera positions, and requires more computation power in the post-processing.

Here, I present an extension of the free-surface synthetic Schlieren (FS-SS) method of Moisy et al. [115], which allows to directly measure the topography and the height of the free liquid surface in laboratory experiments using a single camera, without neither reference height nor parametric models. In this Chapter, the working principle of this method is introduced. Two sets of experiments carried out to test the method are presented and accompanied by a detailed discussion.

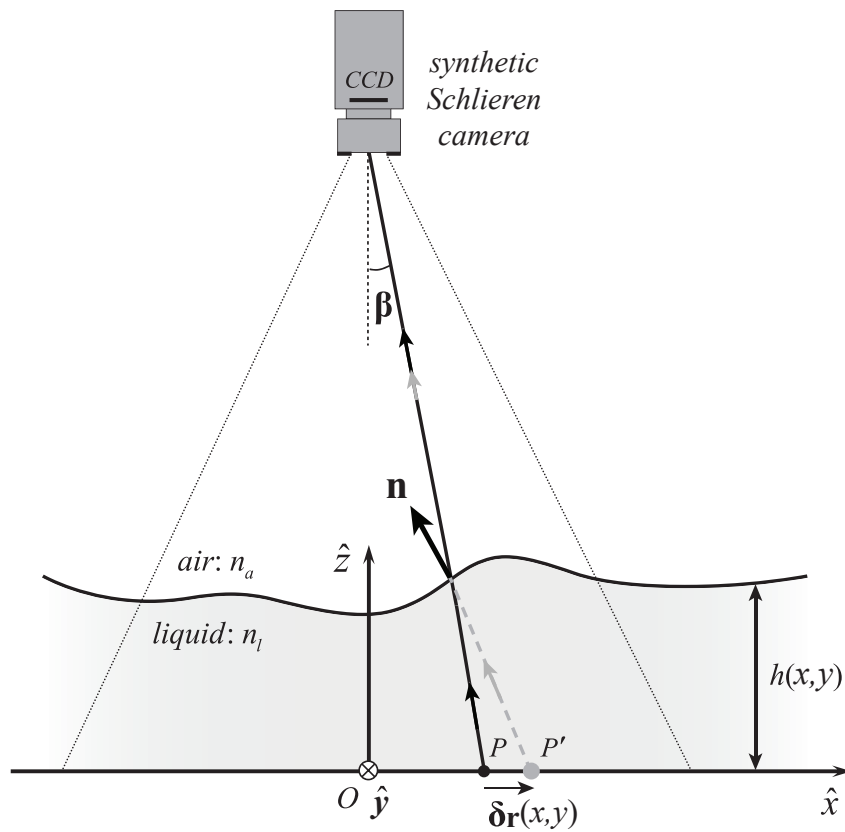


Fig. 4.1: Schematic of the working principle for measuring the topography and the height of free air-liquid surface $h(x, y)$, with a surface normal direction \mathbf{n} . $(\hat{x}, \hat{y}, \hat{z})$ and O denote the Cartesian coordinate system and the origin, respectively. The displacement from a point P to the point P' (due to the surface refraction) is $\delta \mathbf{r}$. β is the angle between the light (black line with an arrow) and the camera axis.

4.2 Methodology based on the refraction

The presented methodology exploits the light refraction at the air-liquid interface. A schematic of the working principle, based on the synthetic Schlieren method [115] and the background-oriented Schlieren method [133], is shown in figure 4.1. When there is no liquid, the incident light ray at a point P follows a straight trajectory (shown in black) toward the camera. When there is a liquid-air interface, the incident light ray at point P' follows the dashed gray trajectory toward the surface and then follows the same black trajectory after leaving the surface. The light refraction is governed by the Snell's law for refractive index of the liquid n_l and that of the gas n_a (in this study $n_l = 1.334$ and $n_a = 1$, corresponding to water and air). The displacement $\delta \mathbf{r}$ from the point P to the point P' depends on the liquid height $h(x, y)$, and its spatial gradients $\nabla h(x, y)$. In detail, this relationship can be derived from the sketch in figure 4.2, which gives

$$\left\{ \begin{array}{l} S'P = h \tan(\beta), \\ S'P' = h \tan(\beta + \theta), \\ \delta \mathbf{r} = S'P' - S'P, \\ \tan(\beta') = \nabla h, \\ \sin(\beta' - \beta - \theta) n_l = \sin(\beta' - \beta) n_a, \end{array} \right.$$

where the first four equations are obtained from geometry and the last one is from the Snell's law. Combining the above equations to eliminate θ gives the equation:

$$\delta \mathbf{r} = h \left[\tan \left(\tan^{-1}(\nabla h) + \sin^{-1}[(n_a/n_l) \cdot \sin(\beta - \tan^{-1}(\nabla h))] \right) - \tan(\beta) \right], \quad (4.1)$$

where $\beta = \beta_x(x, y)\hat{x} + \beta_y(x, y)\hat{y}$ denotes the angle of the camera viewing the point P . When the camera is set to satisfy the paraxial approximation, $\beta(x, y)$ is small so that $\tan(\beta) \approx \beta$. Similarly, $\tan(\nabla h) \approx \nabla h$ when ∇h is small, e.g. $\nabla h < 0.5$, see discussion in Section 4.4.5. Then equation (4.1) can be simplified to

$$\delta \mathbf{r} = h \cdot (1 - n_a/n_l) (\nabla h - \beta), \quad (4.2)$$

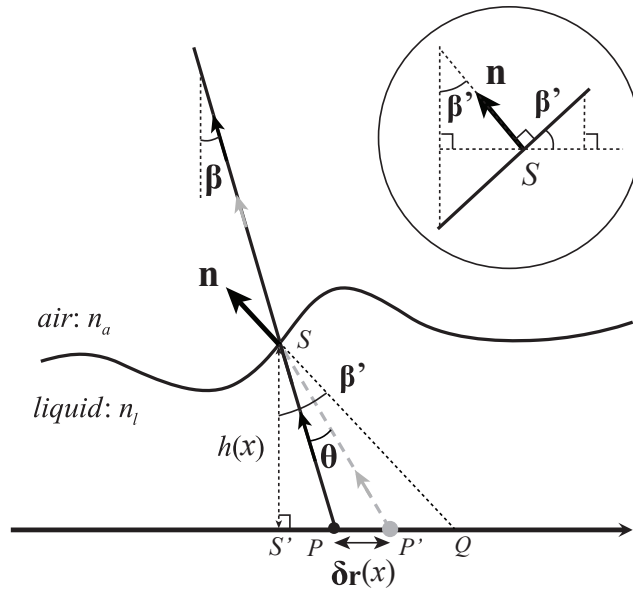


Fig. 4.2: Schematic of the derivation of working principle. The inset shows the zoom-in around the point S .

where $h(x, y)$ is the only unknown to be determined, provided that $\delta \mathbf{r}$ and β have been pre-computed, as explained in what follows.

The displacement $\delta \mathbf{r}(x, y)$ can be obtained by taking the cross-correlation operation over the reference and the refraction images of dot objects (see figure 4.3b, c). Image cross-correlation algorithms, as commonly used in two-dimensional PIV, are applied in this study. In this study, the multi-step algorithm is used with interrogation window $96 \times 96 \text{ pixel}^2$ at the initial step reducing to the window $24 \times 24 \text{ pixel}^2$ with 75% window overlap at the final step, an optimized setting in Lavisision Davis[©]. The interrogation window at the final step includes approximately 8 dots for accurate displacement tracking [134], given that the number of dots in each interrogation window between the paired images is approximately unchanged. In this chapter, the dot objects are printed (randomly distributed) on a transparent sheet. The random distribution of the dots helps the PIV correlation algorithm reduce fortuitous pattern coincidence and renders better accuracy [115]. We carefully designed the pattern, where the diameters of individual dots are approximately 5 to 6 pixels in images.

The camera viewing angles, $\beta(x, y) = \beta_x(x, y)\hat{x} + \beta_y(x, y)\hat{y}$, are determined by the spatial position of the camera to the object pattern (e.g. see figure 4.3a),

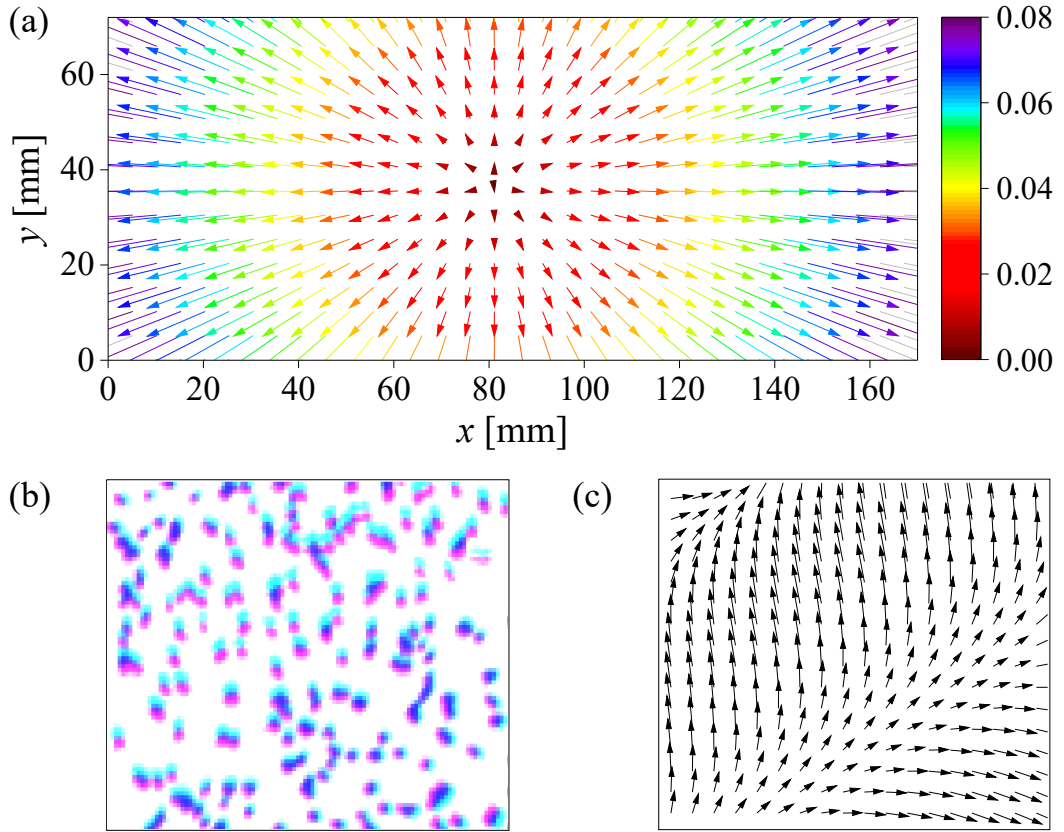


Fig. 4.3: (a) The vector map of $\beta(x,y)$ obtained in the calibration procedure, where the direction of a vector is given by β_x and β_y , and the color shows the magnitude $|\beta|$. Every other vector along each direction is shown for clarity. (b) A portion of dot pattern is shown: pink dots (tuned from black) are from a calibration image, while cyan dots (tuned from black) are from a measurement image of surface ripples, and the overlap is in blue. (c) The displacements $\delta \mathbf{r}$ (amplified 4 times in length for clarity) between the pink and the cyan dots in (b).

and can easily be obtained in a calibration procedure. For a leveled flat bottom and a still (flat) water surface (i.e. $\nabla h = 0$, known n_l), the surface height h_c can be measured with a caliper precisely. According to equation (4.2), $\beta(x,y) = -\delta \mathbf{r}_c(x,y)/[h_c(1 - n_a/n_l)]$ with $\delta \mathbf{r}_c(x,y)$ obtained from the cross-correlation operation. Note that the height h_c can be freely chosen and does not depend on the details of the experiments (e.g. water fill level) to be performed in the tank.

The $h(x,y)$ in equation (4.1) and (4.2) is solved by using the Matlab intrinsic function *fsolve* (Levenberg–Marquardt algorithm), which requires long computing time and large memory. To reduce the need of computation power and time, an Matlab code implementing the Newton–Raphson method

was scripted to solve the equation (4.2) (with reduction of the computation time by two orders of the magnitude). The gradient ∇h is discretized with central, second-order finite differences at interior grid points and with forward/backward second-order differences at the boundaries. The displacements $\delta\mathbf{r}(x,y)$ span $M \times N$ grid points, and at each grid point there are two components of $\delta\mathbf{r}$ and one h . This leads to a linear system including $2MN$ equations and MN unknowns. This over-determined linear system can be solved without imposed boundary conditions by Newton iterations from an initial guess (a positive constant) to the converged solution $h(x,y)$. Convergence is assumed if the maximum of the least-squared residual errors in the linear system drops below 10^{-5} .

Note that $\delta\mathbf{r}$ is measured with respect to the point P in figure 4.1, whereas the coordinates of the intersection (surface) point for the solved h differ from P . The coordinates of the solved $h(x,y)$ thus need to be remapped according to $(x,y)^* = (x,y) - h(x,y)\tan[\beta(x,y)]$.

4.3 Applications in air-water surface

In this section, two sets of experiments are presented. In the first one, liquid ripples are generated, for which the spatially averaged surface height is approximately constant. The second one is the dam-break problem (lock-exchange), for which the averaged height changes in time.

4.3.1 Liquid ripples

A tank was manufactured with transparent acrylic plates and had dimensions $1000 \times 150 \times 350 \text{ mm}^3$ in length, width and height. A random dot pattern of $200 \text{ mm} \times 120 \text{ mm}$ was printed on an overhead transparency (thickness of 0.16 mm) with a printer (Ricoh MP C3504). The dot pattern was glued to the inner flat bottom of the tank. A white LED with a light diffuser was applied to illuminate the dot pattern from the bottom of the tank, while a camera (Phantom VEO 640L equipped with a Zeiss lens of focal length 100 mm) in resolution $2560 \times 1600 \text{ pixel}^2$ was placed approximately 1 meter above the

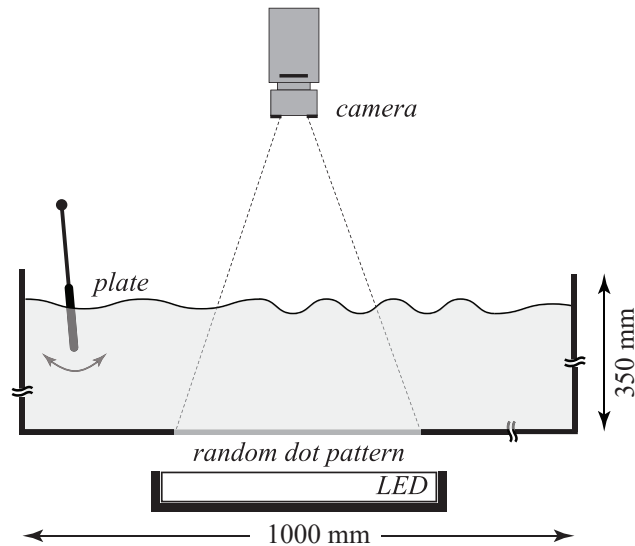


Fig. 4.4: Schematic of measuring topography and height of liquid ripples in a tank. The dimensions are not in scale.

pattern. A plate was employed to flap back and forth to generate surface ripples (see figure 4.4).

The experiments were carried out in the following order. The tank bottom was leveled; An image was captured as the reference image I_0 when there was no water in the tank; The water was filled into the tank to a height of 20 ± 0.1 mm which was measured by a caliper, and an image I_{h_0} was captured when the water surface was still. When the water ripples were generated, a series of images $I(t)$ was recorded.

4.3.1.1 Measurement validation

When the images $I(t)$ are correlated with the image I_0 to get $\delta\mathbf{r}(x, y, t)$, the equation (4.1) is solved to obtain $h(x, y, t)$ with the present method. For comparison, when the images $I(t)$ are correlated with the image I_{h_0} to get the displacements, $h(x, y, t)$ can be obtained with the FS-SS method [115]. The script of FS-SS method of Moisy et al. [115] was downloaded from their website and compared with our script of the FS-SS method to confirm that I understand their method correctly. In their script, the solution of the topographic height at the bottom left point of the computation domain is set to be zero, then the summation of the solved topographic height and the reference height gives the surface height.

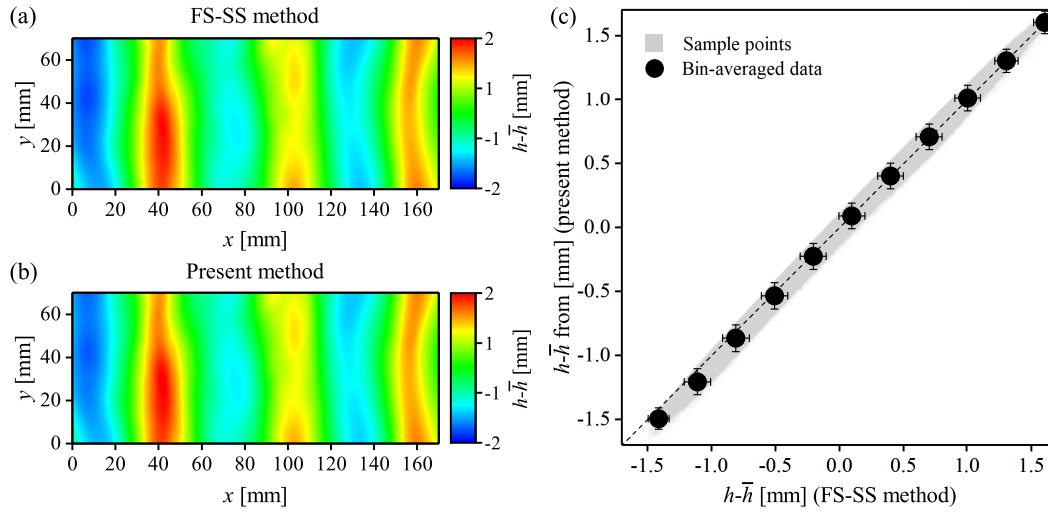


Fig. 4.5: The contours of topography from the FS-SS method (a) and from our method (b). (c) Comparison of $h - \bar{h}$ between present method and FS-SS method in experiments of dynamic ripples, where the gray squares denote individual data in space. A black dot shows the average of the individual points in a bin with the size of 0.3 mm, and an error bar shows the standard deviation of the data in the bin.

A snapshot of the surface ripples measured with our method is shown in figure 4.5(b), and it is visually in good agreement with the result of the FS-SS method shown in (a). This comparison is performed on the surface topography by removing the spatially averaged height $\bar{h}(t)$ from $h(t)$. The particular consideration behind this comparison is that, although the reference height h_0 is constant, the averaged height within the field-of-view measurements may vary temporally, which may break the fundamental assumption of the FS-SS method [115]. About 8,000,000 individual spatial points of $h(x, y) - \bar{h}(x, y)$ from 200 temporal snapshots are shown as the gray squares in figure 4.5(c), where a black dot shows the bin-averaged value of the individual points. Good quantitative agreement between the two methods is obtained.

The measurements for water flat surfaces with different heights are also examined and shown in figure 4.7. The calibration viewing angles $\beta(x, y)$ are obtained when the flat surface is 20 mm height. Subsequently, the calibration angles are used to reconstruct the flat surface with 10 mm height. The mean relative difference is about 0.5%, and the standard deviation is about 0.03%. It is observed that the large difference in the reconstructed surface occurs in the border of the measured region. The reason might result from the equation 4.2, where the present algorithm ascribes the measurement noise

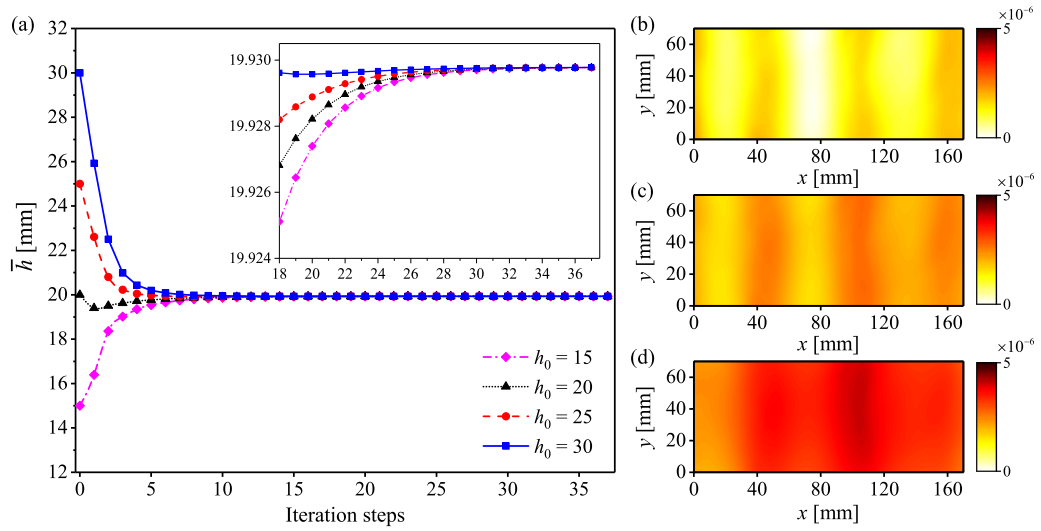


Fig. 4.6: The effects of initial guesses in Newton method on $h(x, y)$ in solution. (a) The mean height \bar{h} resulted from initial guesses $h_0 = 15, 20, 25, 30$ against iteration steps, where the inset shows a zoom for iteration steps larger than 18. (b–d) The contours of topography differences, $h(x, y, h_0 = 30) - h(x, y, h_0 = 20)$, $h(x, y, h_0 = 25) - h(x, y, h_0 = 20)$ and $h(x, y, h_0 = 15) - h(x, y, h_0 = 20)$, respectively.

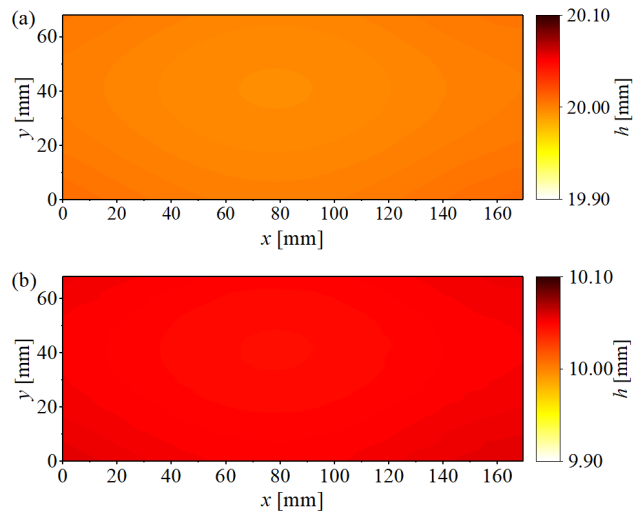


Fig. 4.7: The different flat surfaces with the same calibration viewing angles, $\beta(x, y)$. (a) The contour of the 10 mm surface height. (b) The contour of the 20 mm surface height.

in calibration viewing angles $\beta(x, y)$ to the ∇h . Thus, the reconstructed flat surface has a slight gradient close to the border of x and y . Overall, the present method can as well reconstruct the flat surfaces with a high accuracy but with careful calibration of camera viewing angles.

4.3.1.2 Effect of initial guesses

For an arbitrary initial guess, Newton-Raphson method can be result in divergence, or convergence to a far-away root [5]. Thus, the effect of initial guesses for the Newton-Raphson method on the computed $h(x, y)$ is shown in figure 4.6(a). For the same snapshot shown in figure 4.5(b), the spatially averaged heights \bar{h} computed from initial guesses $h_0(x, y) = 15, 20, 25, 30$ converge to the same value $\bar{h} \approx 19.93$ (see the inset). The contours of the topographic difference on $h(x, y)$ between the result with $h_0 = 20$ (shown in figure 4.5b) and those with other initial guesses are shown in figure 4.6 (b–d), where the difference is only about 10^{-6} . This shows that the present method does not depend on different initial guesses. When the initial guesses are meaningful, i.e. $h_0 > 0$, the present method does not have multi-solution issues as reported in Gomit et al. [62]. In practice, it is suggested to take $h_0(x, y)$ slightly larger than the maximum height of the surface from *a-priori* knowledge of the flow.

4.3.2 Dam-break flows

A dam-break problem involves a liquid current propagating downstream with the averaged height temporally changing. The experiments of the dam-break problem introduced in this section demonstrate that with the method introduced in this Chapter, flows with temporally evolving averaged height can be measured.

The experiments of the dam-break problem were carried out in a lock-exchange setup as sketched in figure 4.8(a). The tank is the same as used in the experiments of the liquid ripples. The experimental procedure is as follows. Water was filled into the locked portion of the tank only (the left side of the gate) to the height marked by a dashed line (45 mm in height);

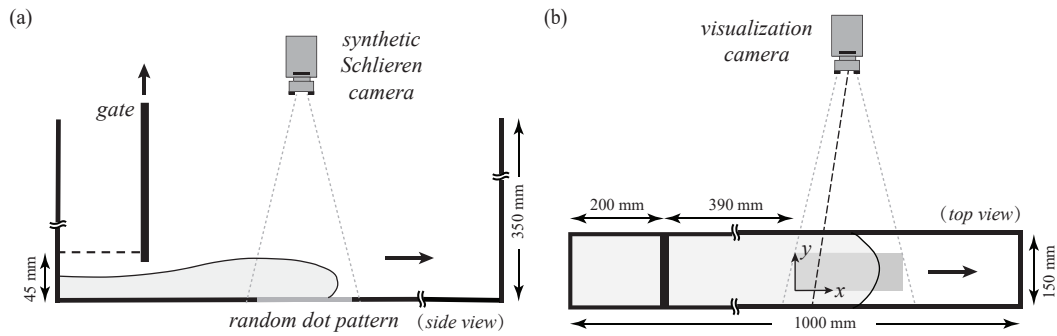


Fig. 4.8: (a) Side view schematic of a lock-exchange experimental setup for propagation of current fronts in a dam-break flow. The camera and illumination systems are the same as in figure 4.4. (b) Top-view schematic of visualization measurements. The thick black arrow indicates the flow direction, and the gray rectangular marks the area where $h(x, y)$ is measured. The dot lines enclose the field-of-view of the visualization camera, and the dash line marks the perspective view of the camera. The dimensions are not in scale.

The gate was rapidly, manually moved away vertically, and the water flowed into the right side of the gate driven by gravity, thereby forming a dynamical current.

The dot pattern was attached to the inner bottom of the tank, while a camera was placed approximately 1.5 m above the bottom (see figure 4.8a). The details of the camera-illumination system are given in Section 4.3.1. An example of the current body, the surface height upstream of the current front is shown in figure 4.9(a), where large spatial variations of the current heights can be observed. In time, the averaged current height \bar{h} changes by 3 mm in a short time interval (300 ms). As consequence, the FS-SS method is inapplicable in this flow condition.

4.3.2.1 Measurement validation

For validation purposes, a visualization system was additionally set up to capture the height profile of the current at the same time. The visualization camera (also a Phantom VEO 640L) was placed approximately 0.7 m away from a sidewall of the tank. A white paper was attached outside another sidewall of the tank to produce an approximately uniform background. Every

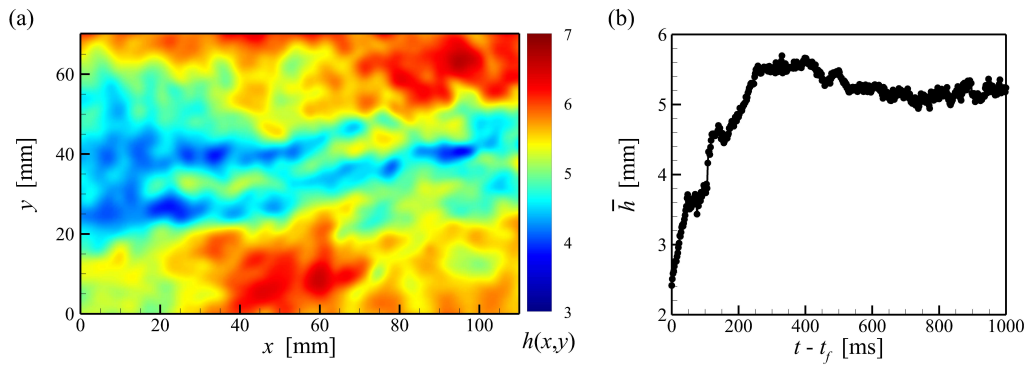


Fig. 4.9: (a) Contours of a sample $h(x,y)$ of the current body at $t - t_f = 234$ ms. (b) Time series of \bar{h} for the current body, where $t_f (= 152$ ms) is time duration of the current front passing the measurement domain. The gate is opened at $t \approx -40$ ms.

liter of water was premixed with 18 ml ink to increase the contrast of the imaged current to the background. The visualization was with illumination from the same LED as the synthetic Schlieren measurement. This visualization measurement approximately captures the surface height averaged in the y direction (see details below). The two cameras were synchronized and the sampling rate of the measurements was 500 frames per second. The measurement domain of the free surface was 110×70 mm in streamwise and spanwise direction, respectively. The upstream border of the measurement domain was about 390 mm downstream of the gate.

The height profile of the current body was obtained from the visualization measurements as follows. An image of the standard deviation (at each pixel) (see figure 4.10a) and an image of the averaged background were obtained from the background images captured before the experiments (i.e. without liquid in the measurement region). A visualization image of the current body is shown in figure 4.10(b). For the visualization image with removal of the averaged background image, if the absolute value at the pixel is larger than three times of the standard deviation at the pixel, it indicates that water flows over the pixelwise region, and the pixel is marked as black (see figure 4.10c). Similarly, if the absolute value at the pixel is smaller than three times of the standard deviation at the pixel, no water flow is expected and the pixel is marked as white (see figure 4.10c). The height profile of the current is

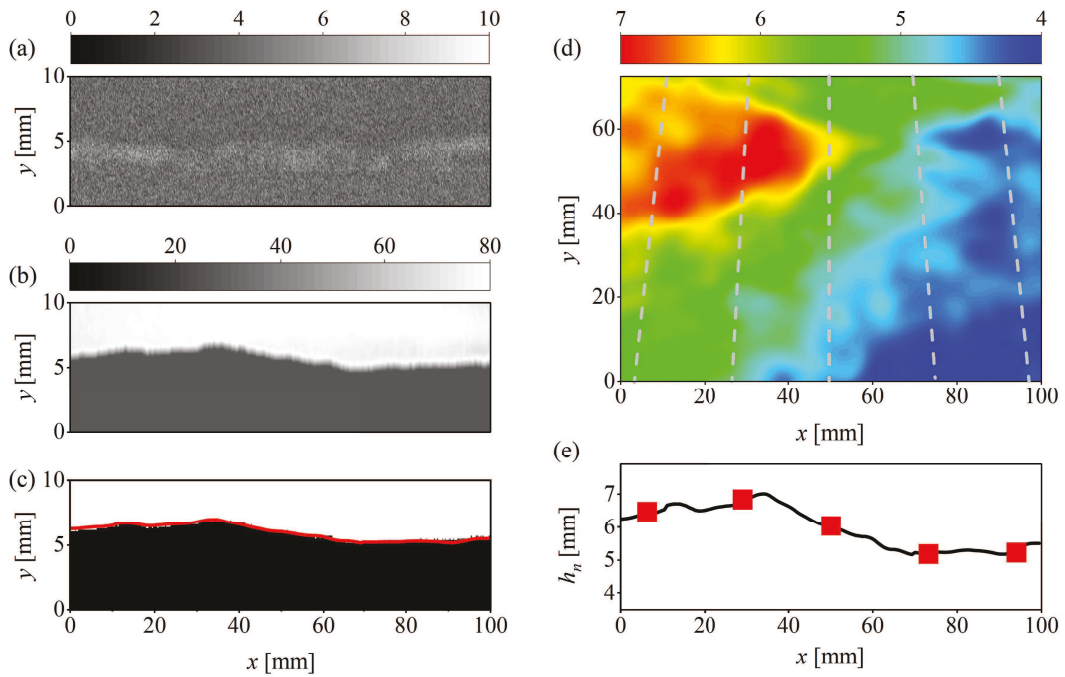


Fig. 4.10: Illustration of the image processing in the visualization measurement: (a) The image of the standard deviation of the background images; (b) A sample of visualization image; (c) The tuned image with marking the pixel with grayscale larger (or smaller) than three times of the standard deviation as black (or white), where a red line marks the height profile. Illustration of obtaining $h_n(x)$ (e) from $h(x,y)$ (d), where dashed lines indicate the perspective direction and five red squares denote the data from the five dashed lines.

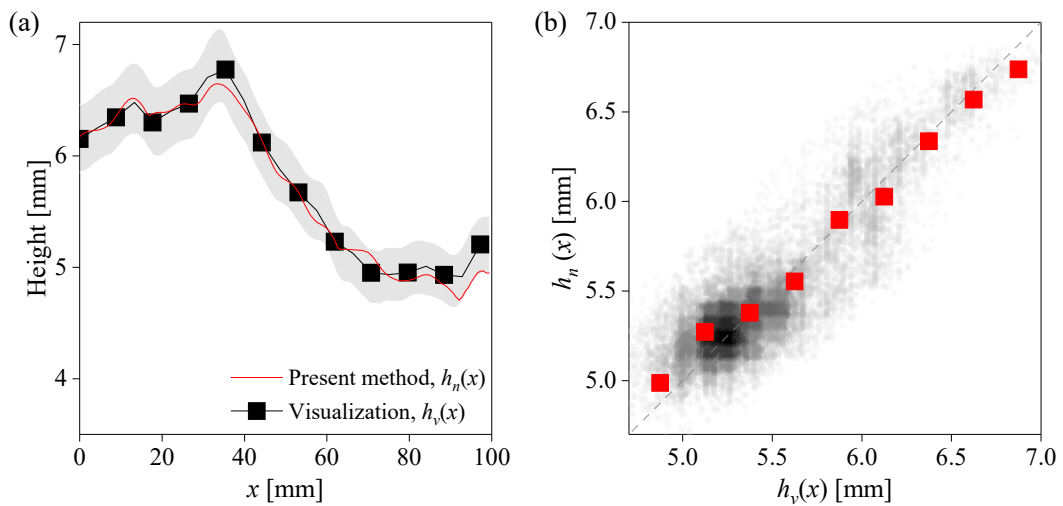


Fig. 4.11: Comparison of streamwise profiles of current body between the visualization and present method. (a) The streamwise profiles $h_v(x)$ (visualization) and $h_n(x)$ (present method) along the streamwise direction x . Gray band show the error bar of visualization measurement. (b) $h_n(x)$ versus $h_v(x)$, where individual data are shown in points and the grayscale level indicates the probability density function (pdf) (the darker the larger pdf), and red squares show the bin-averaged data.

given by the borders between the white and the black regions, then a 3-point moving average operation was used to smooth the profile to give $h_v(x)$ for the visualization measurements (see figure 4.10c).

The visualization camera has a perspective view of the flow, and a point of the height profile approximately corresponds to the maximum height along a perspective line (see e.g. the dash line in figure 4.8b). Thus, for better comparison with the height profile of the visualization measurement, $h(x, y)$ from the synthetic Schlieren method is post-processed. 100 points are defined with equidistance in the streamwise length of the field-of-view of the visualization camera, and they are connected to the position point of the visualization camera to define 100 perspective lines (see examples of 5 perspective lines, the dashed lines in figure 4.10d). The surface height $h(x, y)$ is interpolated along the 100 perspective lines, and the maximum value along each perspective line is obtained to give $h_n(x)$.

In figure 4.11(a) $h_n(x)$ and $h_v(x)$ are then compared, and they approximately collapse. About 24,000 points of the current profiles from about 180 snapshots are shown as gray dots in figure 4.11(b), where the red squares show the bin-averaged data. The two measurement results agree with small differences, which are mainly from two aspects: (1) The data of two measurements are from different sizes of the measurement domain. Although a black mask was used to block the area outside the gray rectangle in figure 4.8(b), the perspective illumination made the visualization measurement domain slightly larger than the measurement domain from the present method. (2) The visualization measurements are affected by the light reflection at the free surface and the spatially inhomogeneous illumination intensity which varies in time. Consequently, the current profiles from the visualization measurements are expected to have larger uncertainties.

4.3.2.2 Dynamics of the current front

The sharp fronts where the height changes abruptly ($\nabla h \gg 1$) in a short streamwise distance (see figure 4.12a) results in an ill-conditioned Jacobian matrix of the Newton-Raphson method. This leads to height errors at the downstream region of the front edge, where the height should be zero. We

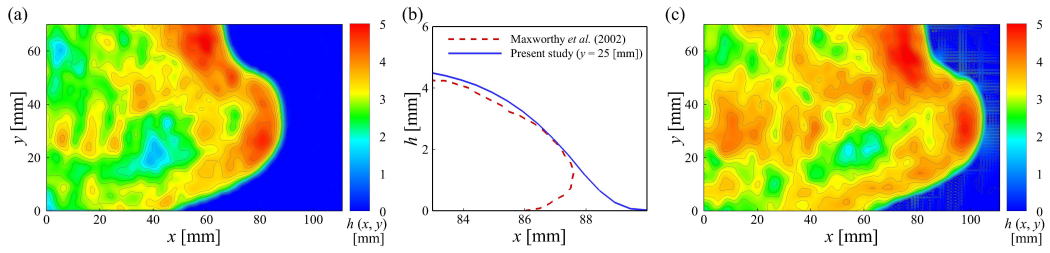


Fig. 4.12: (a) Contours of a sample of the current front with no numerical noise. (b) The height profile of the current front, where the blue solid line shows the profile at $y = 25$ mm in (a). The red dashed line shows a typical profile of a gravity current, which is extracted from the top panel of figure 4 in Maxworthy et al. [108], and the values are adjusted to shown in the same figure. (c) Contours of a sample of the current front with spike-like numerical noise downstream of the front.

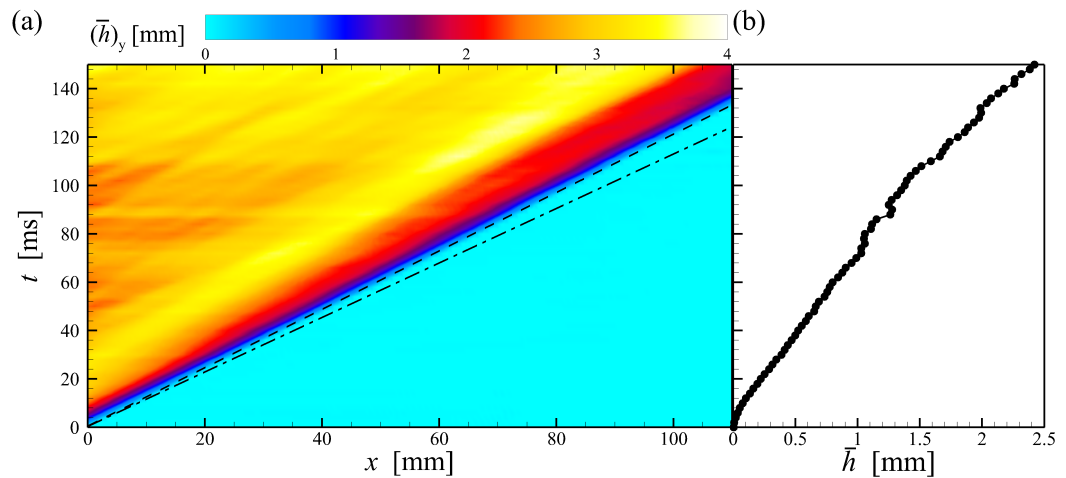


Fig. 4.13: (a) Spatio-temporal diagram of the current fronts, where the color indicates the $h(x,y)$ averaged over y , $(\bar{h})_y(x) = \sum_{i=1}^N h(x, y_i)/N$. The dash line indicates the front speed in our experiments. The front speed of Lowe et al. [105] is nearly the same as our experiments and is also denoted by this dash line. The dash-dot line indicates the front speed of Adegok et al. [1]. (b) The corresponding spatial averaged height $\bar{h}(t)$, in sharing the same axis t .

found that imposing a Dirichlet boundary condition at the downstream border of the computation domain (i.e. $h(\max(x), y) = 0$) can remedy this issue. In addition, occasionally in some snapshots, downstream of the fronts, there are spike-like structures possibly given by numerical noise (height of about 0.5 mm, see figure 4.12b), the cause of which is unclear. The dynamics of the current front (after removing the noise downstream of the front) and the body can be seen through this link (<https://link.springer.com/article/10.1007/s00348-021-03326-0>).

In figure 4.12(a), a region of large height $h \approx 5$ mm can be seen close to the front, downstream of which the height decreases to about 3 mm with large spatial fluctuations. The experiments agree with the simulations of Shin et al. [148] and Borden and Meiburg [15]. However, a difference on the structures at the front interface can be observed (as expected) in figure 4.12(b). This difference is due to the breakdown of the working principle in this region (see the discussion in Section 4.4.4). The spatio-temporal diagram of the current front is shown in figure 4.13(a). The dash line marks the position of the current front at times, and a constant propagation speed can be seen. The front speed in our experiment is approximately 0.82 m/s. This agrees well with the result of Lowe et al. [105] (about 0.83 m/s) and Adegok et al. [1], Lauber and Hager [98] (about 0.9 m/s). In the measurement domain, the averaged height changes in time, i.e., it increases from 0 to approximately 2.4 mm (see figure 4.13b).

4.4 Discussion of the method

Equation (4.2) has a simple form, and can be solved fast for a case using our Matlab code. This is ideal for performing the uncertainty and error analysis, as well as deriving the critical condition when the working principle is broken, thus equation (4.2) is used for solving the surface height in this section.

4.4.1 Measurement uncertainty

The measurement uncertainties of the height surface stem from those of the displacement $\delta\mathbf{r}$ and the calibrated angle β , as well as the refractive indices n_a and n_l .

For the uncertainty of the displacement, the presented method relies on computing the displacements of dots of a pattern via a cross-correlation method. In this Chapter, the configuration of the interrogation windows of size decreasing down to 24×24 pixel² with 75% overlap (a suggested setting in Lavisio Davis[©]), and a sub-pixel Gaussian interpolation was used [134]. The uncertainty is expected to be around 0.1 pixel and smaller, because the random dot pattern was generated to satisfy an optimal PIV condition [115]. In the present problem, the uncertainty on each component of displacements of an instantaneous sample is up to about 0.05 pixel (from Lavisio Davis[©], see Wieneke [180]). To investigate the uncertainty of the cross-correlation method on the measured surface height, the uncertainty propagation in a linear system cannot be applied to the equation (4.1) (or 4.2). Instead, random noise was added to two components of displacement fields to evaluate the uncertainty. Two types of noises were examined: Gaussian distribution with a mean of 0.1 pixel and a standard deviation of 0.05 pixel, where signs (+ or -) of the values are randomly chosen; white noise (ranging from -0.15 pixel and 0.15 pixel). The contaminated displacements were used to calculate the surface height $\hat{h}(x, y)$, and the resulted difference is $\hat{h}(x, y) - h(x, y)$. This procedure was repeated 100 (Gaussian) +100 (white) times, and for each time the noise was randomly generated.

The uncertainty of the calibration angle $\Delta\beta$ can be obtained from uncertainty propagation as

$$\Delta\beta = \sqrt{\left(\frac{\partial\beta}{\partial\delta\mathbf{r}_c} \cdot \Delta\delta\mathbf{r}_c\right)^2 + \left(\frac{\partial\beta}{\partial h_c} \cdot \Delta h_c\right)^2 + \left(\frac{\partial\beta}{\partial n_a} \cdot \Delta n_a\right)^2 + \left(\frac{\partial\beta}{\partial n_l} \cdot \Delta n_l\right)^2}. \quad (4.3)$$

Here $\Delta(\cdot)$ refers the uncertainty of a quantity, i.e. $\Delta\delta\mathbf{r}_c = 0.1$ pixel ($\approx 8 \times 10^{-3}$ mm in the setup), $\Delta h_c = 0.01$ mm, $\Delta n_a = \Delta n_l = 5 \times 10^{-5}$ are considered. For the calibration data shown in figure 4.3, the mean and the standard

deviation of $\Delta\beta$ are about 10^{-4} and 3×10^{-4} , respectively, taken statistics from the spatial distribution of $\delta\mathbf{r}_c$. For the configuration used in this study, the dominant term contributing to $\Delta\beta$ (approximately 90%) is from $(\partial\beta/\partial\delta\mathbf{r}_c)^2(\Delta\delta\mathbf{r}_c)^2 = (-1/[h_c(1 - n_a/n_l)])^2(\Delta\delta\mathbf{r}_c)^2$. Following the same procedure above, the Gaussian and the white random noises are imposed on β and repeated 100 times for each type of noise, to obtain the uncertainty of the surface height. The uncertainty of the refractive indices are evaluated by using 5 values for each of n_a and n_l (within the uncertainty bounds) to examine their influence on the solved surface height.

The above analysis was implemented on the data shown in figure 4.5(b) and a case with analytical solution, which was numerically generated in equation (4.2) with $h = 0.5 \sin(0.1x + 0.08y) + 10$ (simulating ripple stripes). For the former case, the relative uncertainty of h resulted from that of $\delta\mathbf{r}$, which is obtained from 100 noise samples, is approximately 0.2 % in average (and a standard deviation of 1.2 %) for the Gaussian noise, and 0.1 % in average (and a standard deviation of 0.9 %) for the white noise. The mean relative uncertainty of h from that of β is approximately 3.0 % and 1.4 % for the Gaussian and the white noises, respectively, and their corresponding standard deviation is approximately 0.3 % and 0.1 %, respectively. For the considered values, the mean relative uncertainty of h from that of n_a and n_l is approximately 10^{-5} % . For the latter case, the mean relative error of h from that of $\delta\mathbf{r}$ is -0.3 % (and a standard deviation of 2.0 %) and nearly zero (and a standard deviation of 1.4 %) for the Gaussian and white noises, respectively. The mean relative uncertainty of h from that of β is approximately 4.1 % and 2.2 % for the Gaussian and the white noises, respectively, and their corresponding standard deviations approximate 0.5 % and 0.3 %, respectively. The mean relative uncertainty of h from that of n_a and n_l is approximately 10^{-4} % for the considered values.

For the results above, the overall uncertainty of the surface height seems to be from that of β . However, if in the calibration h_c is doubled, the dominant contribution term to $\Delta\beta$ is approximately reduced half, and the corresponding uncertainty of the surface height is approximately 1/3 of the original value. An even larger h_c is expected to further reduce the influence of $\Delta\beta$ to the measured surface height. In summary, the uncertainty of the

Tab. 4.2: The averaged surface height \bar{h} computed from the displacements including the camera vibration $\delta\mathbf{r} + \delta\mathbf{r}_{\text{vibration}}$ for the measurement sample of \bar{h} from the experiments of liquid ripples, and $\delta\mathbf{r}_{\text{vibration}}(x, y) = c_r y + c_t$.

c_t	$c_r \times 10^{-4}$						
	-3	-2	-1	0	1	2	3
-0.20	10.28	9.92	9.63	9.48	9.54	9.82	10.26
-0.15	10.00	9.67	9.47	9.45	9.67	10.07	10.58
-0.10	9.74	9.49	9.40	9.55	9.90	10.39	10.93
-0.05	9.53	9.39	9.46	9.75	10.21	10.74	11.29
0.00	9.41	9.40	9.63	10.05	10.56	11.10	11.68
0.05	9.39	9.54	9.90	10.39	10.92	11.47	12.00
0.10	9.49	9.79	10.23	10.76	11.30	11.84	12.36
0.15	9.70	10.10	10.60	11.13	11.67	12.19	12.70
0.20	9.99	10.45	10.97	11.51	12.03	12.54	13.04

measured surface height is approximately 3 % for this method, and it is determined by the uncertainty of the displacement, which is given by the uncertainty of the correlation algorithm.

4.4.2 Effect of camera vibration

The measurements using our method are sensitive to camera vibration. In our preliminary set-up, the camera vibration was particularly evident and it was possibly from the cooling fan of the high-speed camera, as reported elsewhere [115], or the vibration of the supporting profiles for the camera. The vibration produced approximately 0.2 pixel in images of a still target, and the vibration was mainly along y direction in the images. To evaluate the effect of the camera vibration on surface height, a noise taking the form $\delta\mathbf{r}_{\text{vibration}}(x, y) = c_r \cdot y + c_t$ is employed to mimic rotation (c_r) and translation (c_t) of the camera in vibration. $\delta\mathbf{r}_{\text{vibration}}$ is then added to the measured $\delta\mathbf{r}$ to compute $h(x, y)$. The combination of $-3 \times 10^{-4} \leq c_r \leq 3 \times 10^{-4}$ and $-0.2 \leq c_t \leq 0.2$ (in pixel) gives vibration displacement up to 0.4 (pixel). Taking a measurement sample of $\bar{h} \approx 10$ as an example (as seen in table 4.2), the mean height ranges from 9.3 to 13, producing the relative error up to approximately 30 % (see table 4.3).

Tab. 4.3: The relative errors (%) of $\bar{h}(x, y)$ referring to the case $c_r = 0$ and $c_t = 0$ in table 4.2.

c_t	$c_r \times 10^{-4}$						
	-3	-2	-14	0	1	2	3
-0.20	2.33	-1.28	-4.15	-5.63	-5.06	-2.28	2.10
-0.15	-0.51	-3.72	-5.77	-5.91	-3.76	0.25	5.29
-0.10	-3.05	-5.58	-6.42	-4.97	-1.43	3.40	8.75
-0.05	-5.10	-6.56	-5.86	-2.90	1.62	6.88	12.34
0.00	-6.37	-6.40	-4.12	0.00	5.08	10.51	15.94
0.05	-6.57	-5.02	-1.42	3.41	8.74	14.17	19.51
0.10	-5.57	-2.59	1.88	7.06	12.45	17.81	23.02
0.15	-3.47	0.54	5.49	10.79	16.14	21.38	26.46
0.20	-0.57	4.06	9.22	14.52	19.76	24.87	29.81

Particular care is therefore necessary to stabilize the camera against vibrations. If the vibration remains intolerable, measuring the vibration simultaneously with the surface height is necessary. For instance, the border or the corner region in the field-of-view of a camera can be used to record still objects without any light refraction, while the center region of the frame can be used to measure the marker displacements for the surface height. The shifts of the still targets can be then taken for evaluation of the camera vibration, e.g. through a two-dimensional linear interpolation (with assumed form $\delta \mathbf{r}_{\text{vibration}}(x, y) = c_r \cdot y + c_t$). The $\delta \mathbf{r}_{\text{vibration}}(x, y)$ needs to be removed from $\delta \mathbf{r}(x, y)$ before the Newton-Raphson computation.

The vibrations can also be decomposed to the motions within the camera sensor plane and the ones along the optical axis. The former brings in spatially uniform displacement to $\delta \mathbf{r}$. The latter gives changes to the displacement field which is associated with the focal length of the camera lens, and it affects the mean surface height more rather than the surface topography (i.e. ∇h). For a small vibration (ϵ_{l_0}) of a camera along the optical axis, the magnitude of the measurement error of the surface height at a point \mathbf{x} equals $|\delta \mathbf{r}(\mathbf{x}) \cdot \epsilon_{l_0} / (1 - n_a/n_l) / (\nabla h \cdot l_o - \mathbf{x})|$, after ignoring the high-order small-magnitude terms. Here l_o is the object distance of the camera. Given the trivial influence of the vibration on ∇h , the magnitude of the measurement error of the surface height is reduced as l_o is increased if the magnification of the displacement is kept the same. This implies that, if keeping the measurement field-of-view and imaging magnification the same, a camera

Tab. 4.4: The effect of interrogation window size on the surface height and topography of the snapshot in figure 4.5(c).

Interrogation window [pixel ²]	$\max(h) - \min(h)$ [mm]	$\max(\nabla h)$ [1/mm]	\bar{h} [mm]
24 × 24 (0 % overlap)	0.921	0.165	9.666
48 × 48 (0 % overlap)	0.882	0.116	10.214
96 × 96 (0 % overlap)	0.852	0.063	10.189

lens with a longer focal length (used with longer object distance) is preferred to reduce the influence of the vibrations.

4.4.3 Effect of resolution

The spatial resolution of the displacement $\delta r(x, y)$ plays a key role for measurements of $h(x, y)$. The dynamic range of surface topography wavelengths is determined approximately by the dynamic range of δr . To examine the effect of resolution, a pair of images was processed with the interrogation window size of 24² pixels² up to 96² pixels² and 0 % overlap was used. As shown in table 4.4, as the resolution is decreased (increase of window size), the topographic structures are smoother and more flat, given by the decrease of $\max(|\nabla h|)$ and the decrease of $\max(h) - \min(h)$, respectively, and the averaged height is correspondingly changed.

The two-dimensional power spectrum was calculated for $h(x, y) - \bar{h}$ to examine the fluctuations of the heights, and the radially averaged power spectrum is shown in figure 4.14(a). The curve of 48² nearly collapses with that of 24² for moderate and large topography structures (see b and c). For an interrogation window of 96² pixels², the spectra curve deviates that of 24², while the noticeable difference on the surface topography can be seen in (b) and (d).

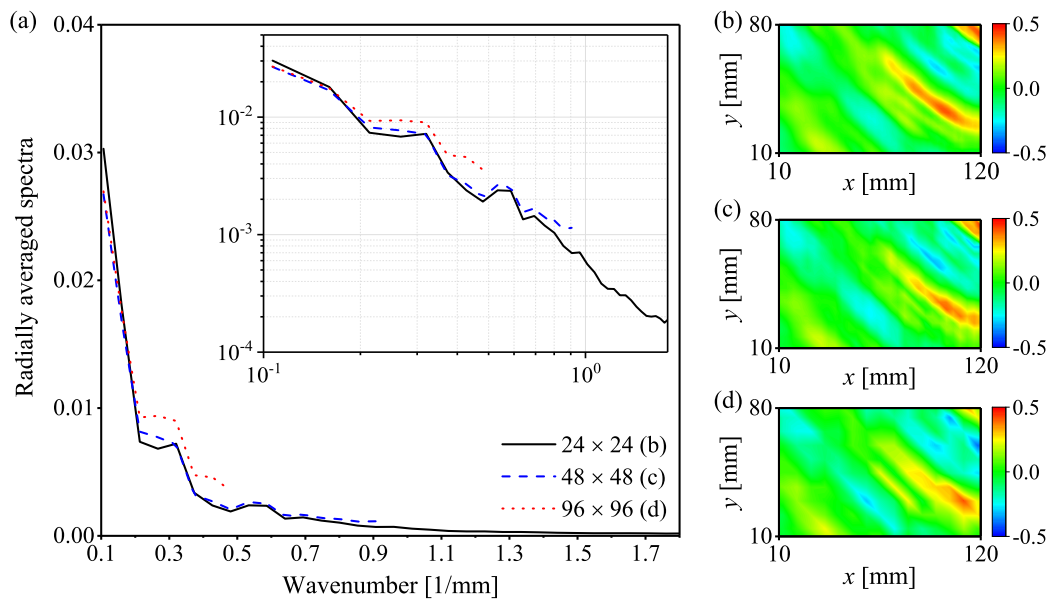


Fig. 4.14: (a) Radially averaged spectra of $h(x, y) - \bar{h}$ for three interrogation window sizes. The inset shows the same data in logarithm-logarithm axes. (b–d) Contours of the same region obtained with interrogation window 24^2 , 48^2 and 96^2 pixels², respectively.

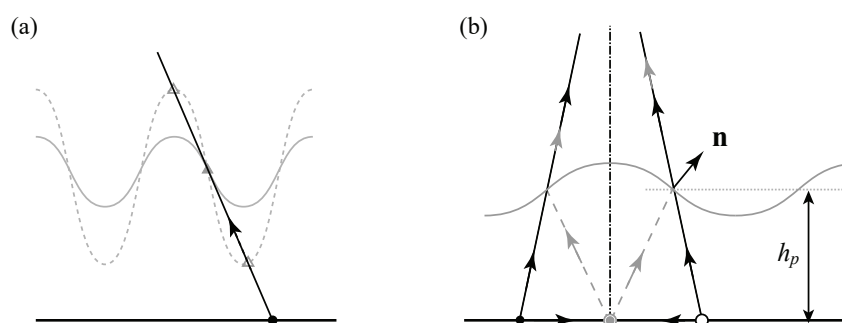


Fig. 4.15: The illustration of breakdown condition of the working principle: (a) Large oscillation amplitude of surface wave, where the light ray is refracted more than once as marked by hollow triangles. (b) Critical condition for formation of caustics.

4.4.4 Breakdown condition of the working principle

In the present method, the governing equation is physically correct provided that the light is refracted *once* on the air-liquid interface. The working principle of the present method is violated when a light ray is refracted more than once or caustics are formed. The critical condition for the former case can be depicted: For a given cosinusoidal plane wave $h(x) = h_p + \eta_0 \cos(2\pi x/\lambda)$ with wavelength λ and amplitude η_0 , the critical wave amplitude is $\eta_c = \lambda[1/4 - \beta_x/(2\pi)]$. At the same wavelength, when $\eta_0 > \eta_c$, light ray may be refracted more than once, see the dashed line in figure 4.15(a). For the snapshot in figure 4.5(c), $\lambda \approx 60$ (mm) and $\beta_x \approx 0.08$ (rad) give $\eta_c \approx 15$ (mm) $>$ 4 (mm), and rays are refracted only once at the surface. The formation condition of the caustics depends on the viewing angle and the curvature of the surface [62]. Taking the same cosinusoidal plane wave as an example, substituting $h(x, y) = h_p + \eta_0 \cos(2\pi x/\lambda)$ into the equation 4.2 with $\delta r(\lambda/4) \approx h_p \beta_x + \lambda/4$, the critical height is $h_{p,c} = \lambda^2/[8\pi\eta_0(1 - n_a/n_l)]$ taken the minimum of h_p . When $h_p < h_{p,c}$, no caustics is expected to be formed. However, for the very front of the current in the dam-break flow, the light rays are refracted more than once.

An *a posteriori* method was introduced in [115] to evaluate the formation of the caustics. When the largest extensional strain of the displacement field is smaller than one, no formation of caustics is expected. This *a posteriori* method is used to examine all snapshots in this study. For instance, the maximum eigenvalue for the snapshot in figure 4.5(c) is 0.193 ($<$ 1) and 0.025 ($<$ 0.15) [115].

4.4.5 The effect of linearizing the governing equation

Equation (4.2) is obtained by linearizing the governing equation (4.1), e.g., taking $\tan \nabla h \approx \nabla h$ and $\tan \beta \approx \beta$, by truncating the second and higher order terms in their respective Taylor expansion. For example, at $\nabla h = 0.5$,

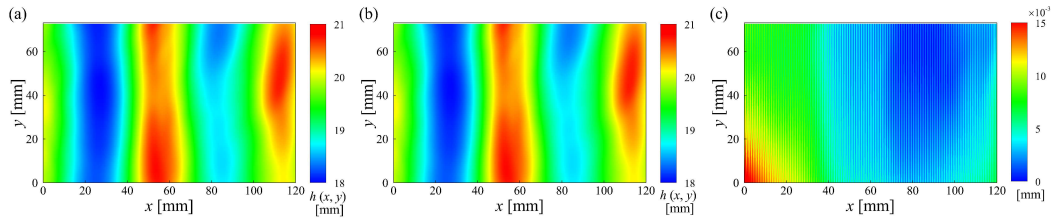


Fig. 4.16: Contours of a sample of the surface ripples (the same snapshot as in figure 4.5 which is obtained by solving (a) the linearized equation (4.2), (b) equation (4.1) and (c) their difference.

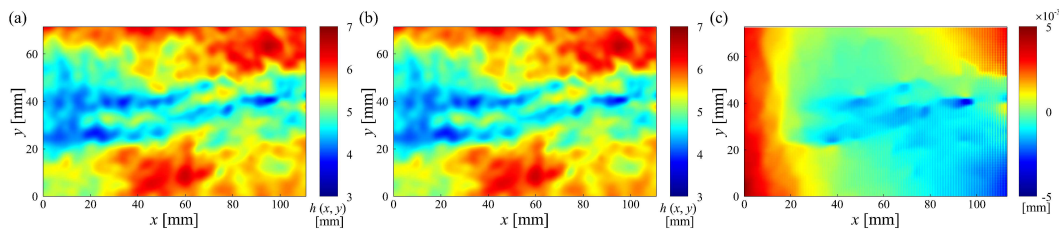


Fig. 4.17: Contours of a sample of the current body (the same snapshot as in figure 4.9) obtained by solving (a) the linearized equation (4.2) and (b) equation (4.1) and (c) their difference.

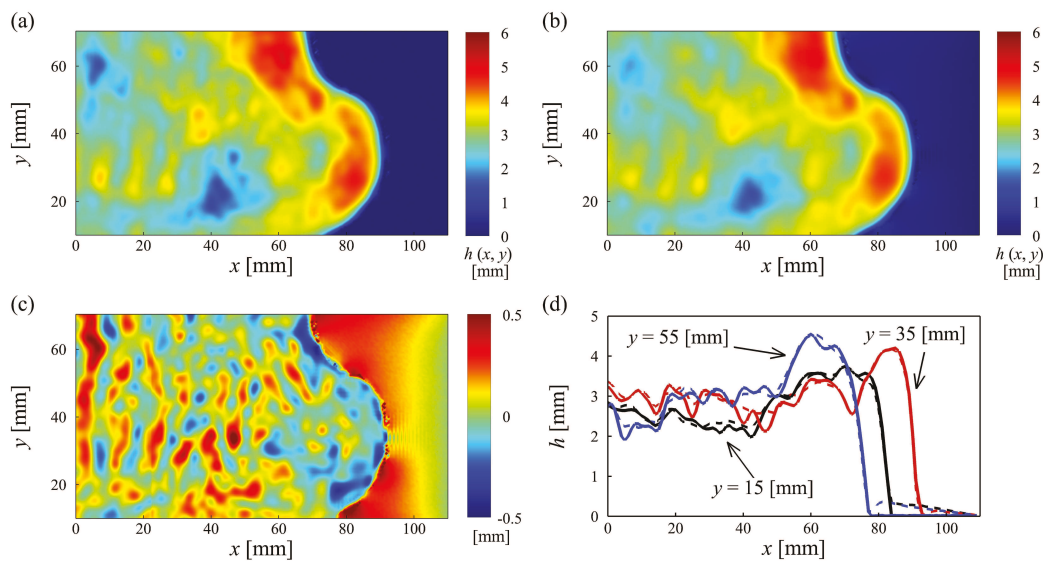


Fig. 4.18: Contours of a sample of the current body (the same snapshot as in figure 4.12) obtained by solving (a) the linearized equation (4.2) and (b) equation (4.1) and (c) their difference. (d) Three height profiles chosen from (a) (solid lines) and (b) (dashed lines) at $y = 15$ mm, 35 mm and 55 mm.

$\tan(\nabla h) \approx 0.5463$ and the relative difference is about 8%. The influence of the approximation on the solution is examined in the following.

For the snapshot of the surface ripples shown in figure 4.5(b), the solution of the equation (4.2) and the equation (4.1) is shown in figure 4.16(a) and (b), respectively. The difference between (a) and (b) is shown in (c). The mean relative difference is about 0.02 %, and the standard deviation is also about 0.02 %. For the snapshot of the current body shown in figure 4.9(a), the solution of the equation (4.2) and the equation (4.1) is shown in figure 4.17(a) and (b), respectively. The difference between (a) and (b) is shown in (c). The mean relative difference is about 10^{-3} % and the standard deviation is about 0.1 %.

For the snapshot of the current front shown in figure 4.12(a), the solution of equation (4.2) and equation (4.1) have visual differences (see figure 4.18a and b). The difference between the two solutions, as shown in (c), gives the mean relative difference about 12 % and the standard deviation of about 30 %. Such difference is expected, since in the front $\nabla h \gg 1$ which violates the linearization approximation. Examination of the height profiles shows that the difference also exists downstream of the front (see figure 4.18d). Although the same Dirichlet boundary condition was employed for both solvers, the noise at downstream of the front for the equation (4.1) remains noticeable, whereas that for the linearized equation is nearly removed.

The linearized equation is accurate for $\nabla h < 1$, whereas for $\nabla h \gg 1$ (the current front), solving equation (4.1) is expected to give better results. However, downstream of the front there is noticeable noise albeit the Dirichlet boundary condition is imposed. In consideration that solving equation (4.1) takes much more computation power, the linearized equation is therefore preferred.

4.5 Summary and potential applications

In this Chapter, a single-camera synthetic Schlieren method was introduced to measure the topography and height of dynamic free surface. In this method,

displacements of the dot patterns are attributed to both the surface height and its spatial gradients, while the reference height is not required. This method is thus applicable to flows with spatially averaged height evolving in time. The dot displacements are obtained by the cross-correlation operation, while calibration is carried out to obtain the viewing angle of a camera toward the pattern object. The surface height, the only unknown in the governing equation, can be solved via a Newton-Raphson method with a proper initial guess.

Two experiments were carried out to demonstrate the present method. In the experiments of surface ripples, the spatial averaged height is nearly constant. No particular treatment is performed on the boundary conditions at the borders of the computation domain. The measurement results of the present method and those of the FS-SS method of Moisy et al. [115] agree well. In another experiment, the averaged height of the current in a dam-break problem changes with time. For the current front, a Dirichlet boundary condition is applied to the downstream boundary condition of the computation domain to amend the ill-conditioned Jacobian matrix in the Newton-Raphson solver (possibly due to the sharp current front). The Dirichlet condition is not necessary for the current body, but only when the front passes the measurement section.

The measurement uncertainty was analyzed and it was found that the uncertainty of the measured surface height (approximately 3 % in this study) is dominated by the uncertainty of the displacements obtained using the correlation algorithm. In addition, the presented method is still susceptible to some limitations, when the working principle can be satisfied. Specifically, the measurement results are sensitive to the camera vibrations, a problem also reported in the FS-SS method. The vibrations change the spatial relation between the camera and the dot pattern, consequently the solutions are affected particularly on the averaged surface height. Thus, particular care is required to improve the stability of the camera as well as other components of the experimental setup. When further improvement on the setup stability is impossible, a camera with a lens of long focal length is suggested while keeping the same field-of-view being viewed, the solution is found to be less sensitive to the vibrations in our practical tests. An alternative suggested

solution is to take the measurements of free surface using a portion of the camera sensor, in the meanwhile use the other portion of the sensor to record the still object which is not affected by light refraction on imaging.

The synthetic Schlieren method introduced in this Chapter is developed based on the Snell's law. It is a promising tool to investigate a mixing case, namely the air-water exchange process, during which the gas exchange velocity is a crucial parameter and mainly related to the water-side near-surface turbulence, surface waves and mixing [80]. But because of two-phase flows with a large refractive index difference, this air-water interface increases the difficulties of simultaneously measuring the turbulent velocity field near the surface and surface wave structures to study the gas exchange velocity through optical technologies. Some studies need a special PIV technology to study this kind of problem (e.g., interfacial PIV [163]). The developed synthetic Schlieren method is applicable for the surface topography measurement and provides detailed studies for the relationship among gas exchange velocity, surface topographic structures and surface turbulence [121, 140], especially in shallow streams and rivers where the surface turbulence yielded by water flow and bed roughness is the dominant driver of gas exchange [165]. In this type of experiment and analogies, the bed roughness could be regarded as the reference pattern, and this synthetic Schlieren method is expected to be used in an in-situ investigation for contributing to understanding and modelling of gas exchange.

Conclusion

Fluid mixing is a fundamental, multi-scale process in chemical engineering and oceanography. Optical measurement techniques (e.g., PLIF and PIV) have been successfully applied to experimentally investigate miscible liquid-liquid mixing, especially in passive scalar mixing, e.g., [112, 38, 168]. However, because of the limited spatial resolution of the measurement techniques, the turbulent small-scale mixing remains challenging for experiments despite that previous theoretical and numerical studies have achieved notable progress [21, 20, 30, 10, 152, 79, 44]. A further difficulty exists in active fluid mixing. When fluids of different densities, such as water and ethanol are mixed, the optical distortion due to the spatio-temporally varying refractive index field poses substantial contamination to optical measurements for the small-scale fluctuations in turbulence [123, 86]. Furthermore, the experimental characterization of the mixing process of two-phase immiscible (or weakly soluble) fluids is equally challenging, because of the large refractive index difference between the two fluids. Gas-liquid mixing is a typical case. Investigating the topography structures of the gas-liquid interface is helpful to understanding the scalar transfer and mixing across the interface [80, 184, 185, 163]. This thesis focuses on optical measurement techniques to experimentally investigate miscible liquid-liquid mixing and gas-liquid mixing. Its main results are summarized in what follows.

5.1 Main results and summary

5.1.1 Mixing in the T-mixer

In order to study the passive scalar mixing characteristics (especially of the small-scale mixing), a T-mixer was designed with a height, H , of 40 millimetres to enable accurate measurements of small-scale mixing with optical

techniques. A high-resolution PLIF technique was employed in proof-of-concept experiments in a T-junction, which indicate that measuring the full viscous-convective range is possible. Furthermore, for comparisons with numerical simulations, long inlet channels were designed to ensure fully developed inflows and achieve accurate boundary conditions. The fully developed laminar flows were examined and the flow regimes (e.g., the engulfment and the unsteady symmetric regimes) for different Reynolds numbers were characterized with PIV measurements, which were cross-validated with numerical simulations through the Strouhal numbers. In addition, it was found that during the T-mixer experiments, the temperatures of room and water were slight different and thermal effects affected the fully developed laminar flow and T-mixer flow regimes. The resulting density difference could also possibly causes an optical measurement error in images when PIV and PLIF techniques are employed. However the subsequent investigation of the optical measurement error in the inhomogeneous refractive index field demonstrated that the maximum measurement displacement errors are expected to be of about 0.02 pixels with the employed configurations. Thus, the PIV and PLIF measurements are trustworthy. In conclusion, the T-mixer setup can achieve the inlets with fully developed laminar flows when $Re \leq 1100$ and repeat the flow regimes in previous numerical and experimental studies. The setup is expected to be used to investigate small-scale mixing in the future, once the thermal effects are mitigated.

5.1.2 Optical errors in turbulent mixing

When fluids of different densities, such as water and ethanol are mixed, optical experimental investigations are difficult to implement because of the resulting optical distortion. To estimate the optical measurement error in the mixing process, a ray tracing method was used in a miscible two-fluid turbulent flow. The latter was simulated by DNS and downloaded from Johns Hopkins Turbulence Databases [103, 102]. The measurement errors were studied in the framework of PTV for only studying the effects of the spatio-temporal refractive index field. The measurement errors influenced by the inhomogeneous refractive index field were quantified over four variables: deflection of light rays, position errors of tracers in the image, velocity

measurement errors and acceleration measurement errors. It was found that the measurement errors increase with the increase of the refractive index difference. When the liquids mix with a large refractive index difference, for example, water and ethanol, the optical errors prevail and the optical measurements might be impossible. The results suggest that in preparation of a PTV measurement, the measurement can be refined by reducing the depth of the light rays through the flow field if possible, and/or by reducing the viewing angle of cameras towards the field-of-view. The errors of the velocity and the acceleration are found to be associated with the spatial and spatio-temporal gradients of the refractive index. The latter is controlled by the ratio of velocity-scalar diffusion. Since PTV, PIV, PLIF and other optical flow measurement techniques share the same working principles based on geometric optics, the findings here are also assumed to be applicable to evaluate the influence of the inhomogeneous refractive index field on the measurement errors during the mixing.

5.1.3 Surface wave measurements

Gas transport and mixing can happen in the air-water interface in open channels, rivers, as well as lakes and oceans. The drastic difference in the refractive index of air and water brings difficulties in implementing optical techniques, but can be utilized to reconstruct the surface waves. It has been reported that the surface waves are related to the turbulent mass transfer and mixing across the air-water interface [184, 185]. Learning from the ray tracing simulation, a free-surface measurement method that is promising for understanding the mixing and mass/heat transfer at the air-water interface is introduced and demonstrated. Two experiments were carried out to verify the present method and it was found that the relative uncertainty of the measured surface height is approximately 3 %. The free-surface method in this thesis is expected to be applicable for surface topography measurements and provide detailed studies on the relationship among gas exchange velocity, surface topographic structures and surface turbulence.

5.2 Open questions and future studies

As demonstrated in Chapter 2, the inflow conditions of the T-mixer can guarantee to have a fully developed laminar flow. It is beneficial to compare the velocity field with DNS results and further understand the turbulent mixing and fluid instabilities in T-mixers with moderate and high Reynolds numbers. Through the aforementioned experimental technique (i.e., PIV and PLIF), it may be possible to achieve a qualitative and quantitative understanding of small-scale mixing. More importantly, the scaling of mixing down to the Batchelor scale can be experimentally measured without Taylor frozen hypothesis. Besides, Schikarski and Avila [141] indicated that a T-mixer is a novel system to investigate decaying turbulence in wall-bounded flows. At the center line of the mixing channel, turbulence is isotropic. The decay of turbulent kinetic energy and passive scalar variance follow strictly a power law with a Reynolds number independent exponent, respectively. These exponent values agree with those found by homogeneous isotropic turbulence experiment [153], theoretical work [149] and simulation [22]. Thus, the T-mixer developed in this thesis offers a chance to investigate the influence of the evolving anisotropy apart from the center line on the decay process, and as well study how the passive scalar fluctuates and decays along the channel by experiments.

The ray tracing simulation is a useful tool to evaluate the measurement error due to the inhomogeneous refractive index field and further revise the measurement results. Combined with the background-oriented schlieren (BOS) technique, the optical measurement errors in images can be used to reconstruct the density field, which provides a perspective and a method to understand the mixing evolution of active scalars in time and space. On the other hand, in the PTV numerical experiment of the turbulent flow, the errors of the velocity and the acceleration are found to be associated with the spatial and spatio-temporal gradients of the refractive index. The effects of the velocity and scalar diffusion on the refractive index gradients are also worth of investigation in the future.

The developed synthetic Schlieren method is applicable for surface topography measurements. The footprint (i.e. topographic structures) on the free surface is essential to retrieve the characteristics of turbulence below the surface or the characteristics of air motion above the surface [140, 70]. Simultaneous measurements of the surface waves, gas concentration change and turbulence under the water can facilitate an understanding of the interaction among gas exchange velocity, surface topographic structures and turbulence underneath the interface and further model this process. At the same time, extending this synthetic Schlieren method to actual shallow streams and rivers is helpful to understand the dynamics of the shallow flow and the mixing processes in nature.

Appendix

6.1 Sources of measurement errors

In Chapter 3, the statistical properties of the velocity and acceleration error are shown. Here, the sources of measurement errors are analyzed. In order to locate the sources of the velocity error, evaluating equation (3.6) with equation (3.3) and equation (3.15) (as well as approximating $\epsilon_x \approx \mathcal{N}L$, where \mathcal{N} takes the place of $|\widetilde{N}l| \cdot \widetilde{S}/L$ for simplicity) leads to

$$\begin{aligned}
 \epsilon_u &\approx [\mathbf{x}'(t + \Delta t) - \mathbf{x}'(t) - \mathbf{x}(t + \Delta t) + \mathbf{x}(t)]/\Delta t & (6.1) \\
 &= [\mathbf{x}'(t + \Delta t) - \mathbf{x}(t + \Delta t)]/\Delta t - [\mathbf{x}'(t) - \mathbf{x}(t)]/\Delta t \\
 &\approx \{\mathcal{N}[\mathbf{x}(t + \Delta t), t + \Delta t] - \mathcal{N}[\mathbf{x}(t), t]\}L/\Delta t \\
 &= \underbrace{\{\mathcal{N}[\mathbf{x}(t + \Delta t), t + \Delta t] - \mathcal{N}[\mathbf{x}(t + \Delta t), t]\}L/\Delta t}_{L \cdot \partial \mathcal{N}[\mathbf{x}(t + \Delta t)]/\partial t} \sim L^2 \cdot \partial^2 n / \partial t \partial \mathbf{x} \\
 &\quad + \underbrace{\{\mathcal{N}[\mathbf{x}(t + \Delta t), t] - \mathcal{N}[\mathbf{x}(t), t]\}L/\Delta t}_{L \cdot \partial \mathbf{x} / \partial t \cdot \partial \mathcal{N}(t) / \partial \mathbf{x}} \sim \mathbf{u}L^2 \cdot \partial^2 n / \partial \mathbf{x}^2.
 \end{aligned}$$

For the approximation (under the curly bracket), \mathcal{N} (quantifying the refractive index mismatching level, and having the same unit as the refractive index) is approximated by $L \cdot \partial n / \partial \mathbf{x}$.

For detailed consideration of the velocity measurement error derived in Elsinga et al. [51], the equation (3.16) is repeated here for convenience,

$$\epsilon_u = [\nabla \epsilon_x(t)]\mathbf{u}(t) - [\nabla \mathbf{u}(t)]\epsilon_x(t).$$

The first term can be approximated as

$$[\nabla \epsilon_x(t)]\mathbf{u}(t) \approx [L \cdot \partial \mathcal{N} / \partial \mathbf{x}] \cdot \mathbf{u} \sim \mathbf{u}L^2 \cdot \partial^2 n / \partial \mathbf{x}^2, \quad (6.2)$$

with $\epsilon_x \approx \mathcal{N}L \sim L^2 \cdot \partial n / \partial \mathbf{x}$ as used above. The second term can be rewritten with taking $\mathbf{u} = \partial \mathbf{x} / \partial t = (\partial \mathbf{x} / \partial n) \cdot (\partial n / \partial t)$,

$$\begin{aligned} [\nabla \mathbf{u}(t)] \cdot \epsilon_x(t) &= \partial \mathbf{u} / \partial \mathbf{x} \cdot \epsilon_x = \partial [(\partial n / \partial t) \cdot (\partial \mathbf{x} / \partial n)] / \partial \mathbf{x} \cdot \epsilon_x \\ &\approx \partial [\partial \mathbf{x} / \partial n] / \partial \mathbf{x} \cdot (\partial n / \partial t) \cdot \mathcal{N}L + \partial [\partial n / \partial t] / \partial \mathbf{x} \cdot (\partial \mathbf{x} / \partial n) \cdot \mathcal{N}L. \end{aligned} \quad (6.3)$$

With $\mathcal{N} \sim L \cdot \partial n / \partial \mathbf{x}$, the first term on the right-hand side of equation (6.3) is approximated as $-L^2 \cdot \partial^2 n / \partial \mathbf{x}^2 \cdot (\partial n / \partial t) / (\partial n / \partial \mathbf{x})$, which is $-\mathbf{u}L^2 \cdot \partial^2 n / \partial \mathbf{x}^2$, while the second term on the right-hand side of equation (6.3) is approximated as $L^2 \cdot \partial^2 n / \partial t \partial \mathbf{x}$. In a short summary, the above approximation shows that the velocity measurement error obtained in Elsinga et al. [51], formulated in equation (3.16), is also associated with $\partial^2 n / \partial t \partial \mathbf{x}$ and $\mathbf{u} \partial^2 n / \partial \mathbf{x}^2$, the same as the finding in this thesis.

The effect of the velocity and the refractive index fields on the measurement error of flow acceleration can be approximated as follows,

$$\begin{aligned} \epsilon_a &= \mathbf{a}' - \mathbf{a} \\ &= \partial \mathbf{u}' / \partial t + (\mathbf{u}' \cdot \nabla) \mathbf{u}' - \partial \mathbf{u} / \partial t - (\mathbf{u} \cdot \nabla) \mathbf{u} \\ &= \underbrace{\partial \mathbf{u}' / \partial t - \partial \mathbf{u} / \partial t}_{\epsilon_{a,I}} + \underbrace{(\mathbf{u}' \cdot \nabla) \mathbf{u}' - (\mathbf{u} \cdot \nabla) \mathbf{u}}_{\epsilon_{a,II}} \end{aligned} \quad (6.4)$$

$$\begin{aligned} \epsilon_{a,I} &\approx (1/\Delta t)^2 [\mathbf{x}'(t+2\Delta t) - 2\mathbf{x}'(t+\Delta t) + \mathbf{x}'(t)] \\ &\quad - (1/\Delta t)^2 [\mathbf{x}(t+2\Delta t) - 2\mathbf{x}(t+\Delta t) + \mathbf{x}(t)] \\ &\approx \underbrace{(1/\Delta t) \{ \mathcal{N}[\mathbf{x}(t+2\Delta t), t+2\Delta t] - \mathcal{N}[\mathbf{x}(t+2\Delta t), t+\Delta t] \}}_{L \cdot \partial \mathcal{N}[\mathbf{x}(t+2\Delta t)] / \partial t \sim L^2 \cdot \partial^2 n / \partial t \partial \mathbf{x}} \cdot L / \Delta t \\ &\quad + \underbrace{(1/\Delta t) \{ \mathcal{N}[\mathbf{x}(t+2\Delta t), t+\Delta t] - \mathcal{N}[\mathbf{x}(t+\Delta t), t+\Delta t] \}}_{\mathbf{u}(t+\Delta t)L \cdot \partial \mathcal{N}(t+\Delta t) / \partial \mathbf{x} \sim \mathbf{u}L^2 \cdot \partial^2 n / \partial \mathbf{x}^2} \cdot L / \Delta t \\ &\quad - \underbrace{(1/\Delta t) \{ \mathcal{N}[\mathbf{x}(t+\Delta t), t+\Delta t] - \mathcal{N}[\mathbf{x}(t+\Delta t), t] \}}_{L \cdot \partial \mathcal{N}[\mathbf{x}(t+\Delta t)] / \partial t \sim L^2 \cdot \partial^2 n / \partial t \partial \mathbf{x}} \cdot L / \Delta t \\ &\quad - \underbrace{(1/\Delta t) \{ \mathcal{N}[\mathbf{x}(t+\Delta t), t] - \mathcal{N}[\mathbf{x}(t), t] \}}_{\mathbf{u}(t)L \cdot \partial \mathcal{N}[\mathbf{x}(t+\Delta t)] / \partial \mathbf{x} \sim \mathbf{u}L^2 \cdot \partial^2 n / \partial \mathbf{x}^2} \cdot L / \Delta t \\ &\sim \partial^2 n / \partial t \partial \mathbf{x} \quad \& \quad \mathbf{u} \partial^2 n / \partial \mathbf{x}^2 \end{aligned}$$

$$\begin{aligned}
\epsilon_{a,II} &\approx (1/\Delta t)^2(1/\Delta \mathbf{x})[\mathbf{x}'(t+\Delta t) - \mathbf{x}'(t)][\mathbf{x}'(t+2\Delta t) - 2\mathbf{x}'(t+\Delta t) + \mathbf{x}'(t)] \\
&\quad - (1/\Delta t)^2(1/\Delta \mathbf{x})[\mathbf{x}(t+\Delta t) - \mathbf{x}(t)][\mathbf{x}(t+2\Delta t) - 2\mathbf{x}(t+\Delta t) + \mathbf{x}(t)] \\
&\approx (1/\Delta t)^2(1/\Delta \mathbf{x})[\mathbf{x}'(t+\Delta t) - \mathbf{x}'(t)][\mathbf{x}'(t+2\Delta t) - 2\mathbf{x}'(t+\Delta t) + \mathbf{x}'(t)] \\
&\quad - (1/\Delta t)^2(1/\Delta \mathbf{x})[\mathbf{x}'(t+\Delta t) - \mathbf{x}'(t)][\mathbf{x}(t+2\Delta t) - 2\mathbf{x}(t+\Delta t) + \mathbf{x}(t)] \\
&\quad + (1/\Delta t)^2(1/\Delta \mathbf{x})[\mathbf{x}'(t+\Delta t) - \mathbf{x}'(t)][\mathbf{x}(t+2\Delta t) - 2\mathbf{x}(t+\Delta t) + \mathbf{x}(t)] \\
&\quad - (1/\Delta t)^2(1/\Delta \mathbf{x})[\mathbf{x}(t+\Delta t) - \mathbf{x}(t)][\mathbf{x}(t+2\Delta t) - 2\mathbf{x}(t+\Delta t) + \mathbf{x}(t)] \\
&\approx (1/\Delta t)^2(1/\Delta \mathbf{x})[\mathbf{x}'(t+\Delta t) - \mathbf{x}'(t)][\mathbf{x}'(t+2\Delta t) - \mathbf{x}(t+2\Delta t) \\
&\quad - 2\mathbf{x}'(t+\Delta t) + 2\mathbf{x}(t+\Delta t) + \mathbf{x}'(t) - \mathbf{x}(t)] + (1/\Delta t)^2(1/\Delta \mathbf{x})[\mathbf{x}'(t+\Delta t) \\
&\quad - \mathbf{x}(t+\Delta t) - \mathbf{x}'(t) + \mathbf{x}(t)][\mathbf{x}(t+2\Delta t) - 2\mathbf{x}(t+\Delta t) + \mathbf{x}(t)] \\
&\approx (1/\Delta t)(1/\Delta \mathbf{x})(L)\mathbf{u}'(t)\{\mathcal{N}[\mathbf{x}(t+2\Delta t), t+2\Delta t] - \mathcal{N}[\mathbf{x}(t+\Delta t), t+\Delta t] \\
&\quad + \mathcal{N}[\mathbf{x}(t), t]\} + (1/\Delta t)^2(1/\Delta \mathbf{x})(L)\{\mathcal{N}[\mathbf{x}(t+\Delta t), t+\Delta t] - \mathcal{N}[\mathbf{x}(t), t]\} \\
&\quad \cdot [\mathbf{x}(t+2\Delta t) - 2\mathbf{x}(t+\Delta t) + \mathbf{x}(t)]
\end{aligned}$$

$$\begin{aligned}
&\approx \mathbf{u}'(t) \left[\underbrace{\{\mathcal{N}[\mathbf{x}(t+2\Delta t), t+2\Delta t] - \mathcal{N}[\mathbf{x}(t+2\Delta t), t+\Delta t]\} L/\Delta t (1/\Delta \mathbf{x})}_{L \cdot \partial \mathcal{N}[\mathbf{x}(t+2\Delta t)]/\partial t \sim L^2 \cdot \partial^2 n/\partial t \partial \mathbf{x}} \right. \\
&\quad + \underbrace{\{\mathcal{N}[\mathbf{x}(t+2\Delta t), t+\Delta t] - \mathcal{N}[\mathbf{x}(t+\Delta t), t+\Delta t]\} (L/\Delta \mathbf{x}) (1/\Delta t)}_{L \cdot \partial \mathcal{N}(t+\Delta t)/\partial \mathbf{x} \sim L^2 \cdot \partial^2 n/\partial \mathbf{x}^2} \\
&\quad - \underbrace{\{\mathcal{N}[\mathbf{x}(t+\Delta t), t+\Delta t] - \mathcal{N}[\mathbf{x}(t+\Delta t), t]\} (L/\Delta t) (1/\Delta \mathbf{x})}_{L \cdot \partial \mathcal{N}[\mathbf{x}(t+\Delta t)]/\partial t \sim L^2 \cdot \partial^2 n/\partial t \partial \mathbf{x}} \\
&\quad \left. - \underbrace{\{\mathcal{N}[\mathbf{x}(t+\Delta t), t] - \mathcal{N}[\mathbf{x}(t), t]\} (L/\Delta \mathbf{x}) (1/\Delta t)}_{L \cdot \partial \mathcal{N}(t)/\partial \mathbf{x} \sim L^2 \cdot \partial^2 n/\partial \mathbf{x}^2} \right] \\
&\quad + \frac{\partial \mathbf{u}}{\partial t}(\Delta t) \left[\underbrace{\{\mathcal{N}[\mathbf{x}(t+\Delta t), t+\Delta t] - \mathcal{N}[\mathbf{x}(t+\Delta t), t]\} (L/\Delta t) (1/\Delta \mathbf{x})}_{L \cdot \partial \mathcal{N}[\mathbf{x}(t+\Delta t)]/\partial t \sim L^2 \cdot \partial^2 n/\partial \mathbf{x} \partial t} \right. \\
&\quad \left. + \underbrace{\{\mathcal{N}[\mathbf{x}(t+\Delta t), t] - \mathcal{N}[\mathbf{x}(t), t]\} (L/\Delta \mathbf{x}) (1/\Delta t)}_{L \cdot \partial \mathcal{N}(t)/\partial \mathbf{x} \sim L^2 \cdot \partial^2 n/\partial \mathbf{x}^2} \right]
\end{aligned}$$

$$\sim \mathbf{u}' \partial^2 n/\partial t \partial \mathbf{x} \quad \& \quad (\partial \mathbf{u}/\partial t)(\partial^2 n/\partial t \partial \mathbf{x} + \partial^2 n/\partial \mathbf{x}^2)$$

In summary, the measurement error of the flow acceleration ϵ_a is approximately ascribed to $\partial^2 n / \partial \mathbf{x} \partial t$, $\mathbf{u} \partial^2 n / \partial \mathbf{x}^2$, $(\partial \mathbf{u} / \partial t)(\partial^2 n / \partial \mathbf{x} \partial t)$ and $(\partial \mathbf{u} / \partial t)(\partial^2 n / \partial \mathbf{x}^2)$, spatial and spatio-temporal gradients of refractive index field.

List of Figures

1.1	Mixing pictures. (a) Mixing cream into coffee. (b) Smoke discharges in the atmosphere.	1
1.2	Dynamic viscosity μ (a) and density ρ (b) as a function of the concentration ϕ (mass fraction), for a water-ethanol mixture. Here $\phi = 0$ and $\phi = 1$ correspond to the pure water and ethanol phases, respectively. The red solid lines indicate functions fitted to the experimental data (dots). The figure is reproduced from [142] and explicit fitting expression for $\mu(\phi)$ and $\rho(\phi)$ can be found in [46].	3
1.3	Schematic of the scalar spectrum for $Sc \sim 1$ (red) and $Sc \gg 1$ (blue). The cyan arrows denotes the mean flux of scalar fluctuations. The figure is reproduced from [63].	5
1.4	The measured spectra in the literature (reproduced from [157] and [78], respectively). (a) Spectra of scalar fluctuation along the jet axis for $Z/D = 4$ to $Z/D = 30$. Here D is the diameter of jet nozzle and E_ϕ^* means the dimensionless scalar spectra for simplicity, see [157] for details. (b) Spectra of scalar fluctuation for different initial concentration at the jet exit ϕ_0 and spectra of streamwise velocity fluctuation. The scalar and velocity spectra are normalized by ϕ_0^2 and U_0^2 (jet exit bulk velocity). η_r^{-1} denotes the wave number corresponding to the spatial resolution of their OFLIF technique, see [78] for details.	6
1.5	(a) Undisturbed background pattern, recorded as reference. (b) The same background pattern behind a water-ethanol mixing process. Image distortion and displacements can be observed due to the different refractive indexes of water and ethanol. Note that for clear demonstration, the images are tuned through brightness and contrast.	9

1.6	An example of CO ₂ exchange driven by a wind at the ocean–atmosphere surface. The picture is reproduced from [138]. . . .	11
2.1	(a) A sketch of a T-junction section and coordinates. (b) The green dashed line means the position where PIV measurements are taken and the camera view is from the back of the T-mixer looking down the outlet channel. The red dashed line denotes the position where PLIF measurements are taken and the camera is placed upon the junction. The coordinate origin is the centerpoint of the junction.	16
2.2	The mixing regimes with different Re in the T-junction ($y/H = 0$ plane): (a) Steady symmetric flow, (b) Engulfment flow, and (c) Unsteady symmetric flow. The pictures are reproduced from the experimental results [160].	17
2.3	T-mixer test device consisting of two equally sized tanks (red and cyan) feeding two inlets which meet at a T-junction, where the incoming fluid streams make a 90 degree turn and then mix along the main channel. In the main (mixing) channel PLIF measurements are made. (a) picture of the setup (b) sketch of the top view. (c) The optical configuration viewed along the laser sheet.	18
2.4	The example of the PLIF calibration linear curves at three characteristic pixel locations in the PLIF image. The averaged grayscale values are computed using 100 snapshots at each of the five calibration concentration levels. Symbols show the ensemble average, and the error bars show the standard deviation values. The figure is reproduced from [181].	21

2.5	(a) Colormap of a PLIF measurement, where the concentration ϕ of fluorescent dye is normalized by the maximum. (b) Profiles of ϕ at three selected positions in (a). (c) Probability density function (PDF) of $ \nabla\phi $, where the red and the blue lines correspond to the statistics from the area-of-interest and the area-of-reference (marked in a), which have the same area (40 by 600 pixels) and are at the same distance from the channel mid-plane. Note that 48,000,000 data points ($40 \times 600 \times 2000$; pixels \times snapshots) were collected to obtain sufficiently converged statistics.	22
2.6	Close-up of the concentration profiles of figure 2.5(b) at the area of interest (a) and the area of reference (b).	23
2.7	PDF of the scalar fluctuation, ϕ' (a), and scalar dissipation rate, χ (b), for the area of interest and the area of reference, respectively.	23
2.8	PLIF snapshots at different times, from 1 s to 4 s.	25
2.9	(a) Picture of the T-mixer setup with two equally sized tanks (1), inlet channels (2), pistons and driving systems (3), a T-junction (4) as in figure 2.3(a) and an outlet channel (5). (b) Numerically computed velocity profiles at different development lengths for $Re = 650$	27
2.10	(a) Sketch of the T-mixer setup, where the left branch is omitted (represented by three dots) to leave sufficient space for the details of the right-branch inlet. The setup consists of two symmetric branches and a T-junction section, where PIV measurements are taken. The arrows indicate the flow direction. The green parts show the laser sheet.	27
2.11	(a) The sketch of five equidistant marked positions (400 mm) for the measurement of the piston velocity. (b) A snapshot when the cart of the driving system gets through a marked position. (c) Example sketch for the piston velocity measurements with $Re = 800$. The position velocity is calculated by the mean of the velocities in segments, namely $\sum_{i=1}^4 (x_{i+1} - x_i)/[4(t_{i+1} - t_i)]$. . .	31

2.12	The comparison between the measured mean velocity and the mean velocity from LabView signals at different Re , (a) for velocity and (b) for the ratio of the measured velocity and the input velocity. The red color denotes the data from the left side piston, while the blue color denotes the data from the right side piston.	32
2.13	The relative uncertainty of Re with different piston speeds (a). The Re uncertainty with different Re (b). The uncertainties when $Re < 100$ are not shown because the corresponding piston speeds are not verified.	33
2.14	Evaluation of PIV recordings using cross-correlation. The picture is adapted from [61].	35
2.15	(a) Comparison of velocity profiles between PIV and analytical solution in the left inlet channel of the T-mixer at $Re = 700$ and $x/H = -2.5$. In the inset, the red solid line is the analytical velocity profile from the square duct flow [146] and the blue hollow circle means the velocity profile from PIV measurements. (b) Comparison of centerline ($z/H = 0$) velocity normalized by the bulk mean velocity (U_0) versus dimensionless developed time t/t_{adv} for varying Reynolds numbers (here $t_{adv} = H/U_0$). The arrow indicates the direction of the curves' transition from $Re = 300$ to $Re = 1100$. (c) The critical developed time t_c/t_{adv} when the centreline velocity reaches 98% of asymptotic steady state velocity. (d) Centerline u/U_0 at different Re when $t/t_{adv} = 30$ and $t/t_{adv} = 50$	37
2.16	The velocity field from PIV results when (a) $Re = 100$ and (b) $Re = 160$. The velocity vector components are displayed every 3 points in x and z directions for clarity.	38
2.17	The velocity field from PIV results at a different time when $Re = 280$: (a) $t = 0$ and $t = 4.375t_{adv}$; (b) $t = 1.094t_{adv}$; (c) $t = 2.187t_{adv}$; (d) $t = 3.281t_{adv}$. The period is $4.375t_{adv}$. The velocity vector components are displayed every 3 points in x and z directions for clarity.	39

2.18	The velocity field from PIV results at a different time when $Re = 360$: (a) $t = 0$; (b) $t = 1.278t_{adv}$; (c) $t = 2.556t_{adv}$; (d) $t = 3.834t_{adv}$. The quasi period approximates $5.112t_{adv}$, as shown in figure 2.19. The velocity vector components are displayed every 3 points in x and z directions for clarity. how to estimate the frequency, More snapshots	40
2.19	(a) The time correlation of the velocity magnitude when $Re = 220$ and 360 . (b) Strouhal number as a function of Reynolds number. The data from the simulations of Schikarski et al. [142] are shown as black circles.	41
2.20	(a) The velocity profile at $x/H = -2.5$ when $Re = 500$. The green solid line denotes the analytical solution and the red dash dot line is the laminar velocity profile according to thermal effects. (b) The sketch of the T-mixer inlet channel with a temperature difference. The gravity acceleration is along the negative z direction.	42
2.21	A snapshot of the thermal convection of PIV results after 20 minutes stopping of the driving systems at left inlet channels. .	43
3.1	(a) Two-dimensional schematic of tracing a light ray in a three-dimensional inhomogeneous refractive index field. The gray area (enclosed by two black dashed lines) marks the range of θ_0 . The ray position shift is $\epsilon_r (= \mathbf{r}_0 - \mathbf{r}')$ marked by an orange double-head arrow. (b) Illustration of tracer position and tracer velocity at three times (t_0, t_1, t_2) for the homogeneous and the inhomogeneous refractive index field cases. For the latter, the red dots at the position \mathbf{r}' in (a) form elliptical shaped tracers, while the green circles indicate the imaged tracers from the former case. Black dots mark the respective tracer center. Black and gray arrows indicate the respective velocity, and the blue double-head arrow marks the position error at t_0	52
3.2	(a) The illustration of the numerical experiment domain (gray box, $L \times L \times L$), part of the DNS domain (black box), where the green layer denotes a light sheet. The camera views the light sheet through the gray box. (b) An example of the isosurface of the refractive index field.	57

3.3	Examples of rendered images of tracers: (a) tracer image rendered in the uniform index field; (b) image of the same tracers for the air flow (C1); (c) image of the same tracers for the water flow (C4).	59
3.4	(Color online) Validation of the code: trace rays in a graded-index lens (a)–(c) and a Maxwell’s fish-eye lens (d)–(f). (a) Contours of the refractive index field. (b) A profile of the refractive index. (c) The analytical solution and the simulation result. (d) Contours of the refractive index field. (e) The profile of the refractive index at $x_1 = 0$. (f) The analytical solution and simulation results. Rays are initialized at $(x_1, x_2) = (0, -1)$ with different incident angle θ_0 . The feature of the fish-eye lens gives the destination of the rays at $x_2 (x_1 = 0) = 1$ independent on θ_0	61
3.5	PDF distributions of $ \epsilon_x $ for the case C1 (air) with different simulation step sizes in Runge-Kutta method (a) and with different grid numbers (b).	61
3.6	Ray deflection $ \Delta\theta $ against dimensionless spatial gradients of the refractive indices $ N L$. For the data of previous studies, N was obtained by Δn_{\max} divided by n and by a characteristic length, and these three values were extracted from each corresponding reference with our best estimation. Δn_{\max} is listed in table 3.1. The data of $0 \leq \theta_0 \leq 0.6$ are in blue symbols and those of $0.6 < \theta_0 \leq 0.9$ are in red. Note that only 4000 data points are plotted to avoid oversizing the figure.	63
3.7	The relationship between the length of the light trajectory S and initial incidence angle $ \theta_0 $: (a) air flow (C1) and (b) water flow (C4). The gray dots denote the sample points, and the grayscale is the two-dimensional probability density function of $ \theta_0 $ and S/L , where darker corresponds to larger value of PDF.	63
3.8	(a) Probability distribution of ray deflection angles $ \Delta\theta $ (in unit of rad), where the maximum 10% and the minimum 10% of the data are marked as blue and red, respectively. (b) Probability distribution of spatial gradients of the refractive index $ \nabla n/n $ which the rays pass through, while the DNS data on all grids are shown as reference.	65

3.9	(a) PDF distribution of change of tracer area ΔA , where A is the tracer area in a uniform refractive index field. The $\Delta A/A$ of air was amplified by $K_{\text{water}}\rho_{\text{water}}/(K_{\text{air}}\rho_{\text{air}}) \approx 1185$ to match the data range of the water for comparison, see the red dotted line. (b) PDF distribution of the circularity C of the imaged tracers.	66
3.10	PDF distribution of the magnitude of position error $ \epsilon_x $ for all five cases in this study. The symbols mark the PDF peaks. The inset shows $ \epsilon_x /L$ at the PDF peaks versus $K_{\text{fluid}}\rho_{\text{fluid}}$ (bottom horizontal axis) and Δn_{max} (top horizontal axis).	66
3.11	The distribution of ray deflection distance $ \epsilon_r $, relative difference of the refractive index $ \tilde{N}l $ and initial incidents $ \theta_0 $: (a) air and (b) water.	67
3.12	Tracer position error $ \epsilon_x $ against the relative difference of the refractive indices $ \tilde{N}l $: (a) air flow (C1) and (b) water flow (C4). The dots are grayscaled with the incidence angle $\tilde{\theta}_0$, the larger $\tilde{\theta}_0$ the darker dots.	68
3.13	Colormap of the flow velocity (u_3) and the acceleration (a_3) at time 11.4 (L_0/U_0) from the DNS (a,d), the air flow case (b, e) and the water flow case (c, f). The velocity and acceleration are made dimensionless with U_0 and U_0^2/L_0 , respectively, as introduced in Section 3.3.1.	69
3.14	PDF distribution of the relative velocity error ϵ_{u_3}/u_3 (a), ϵ_{u_2}/u_2 (b), the mean of ϵ_u/u (c), and the corresponding standard deviation (d), the magnitude of the relative error $\epsilon_{ \mathbf{u} }/ \mathbf{u} $ (e) and the angle between \mathbf{u}' and \mathbf{u} (f). In (c) and (d) the filled colors in symbols correspond to C0 and C4 as in (a).	69
3.15	PDF distribution of the relative velocity error ϵ_{a_3}/a_3 (a), ϵ_{a_2}/a_2 (b), the mean of ϵ_a/a (c) and the corresponding standard deviation (d), the magnitude of the relative error $\epsilon_{ \mathbf{a} }/ \mathbf{a} $ (e) and the angle between \mathbf{a}' and \mathbf{a} (f). In (c) and (d) the filled colors in symbols correspond to C0 and C4 as in (a).	71

4.1	Schematic of the working principle for measuring the topography and the height of free air-liquid surface $h(x, y)$, with a surface normal direction \mathbf{n} . $(\hat{x}, \hat{y}, \hat{z})$ and O denote the Cartesian coordinate system and the origin, respectively. The displacement from a point P to the point P' (due to the surface refraction) is $\delta\mathbf{r}$. β is the angle between the light (black line with an arrow) and the camera axis.	81
4.2	Schematic of the derivation of working principle. The inset shows the zoom-in around the point S	82
4.3	(a) The vector map of $\beta(x, y)$ obtained in the calibration procedure, where the direction of a vector is given by β_x and β_y , and the color shows the magnitude $ \beta $. Every other vector along each direction is shown for clarity. (b) A portion of dot pattern is shown: pink dots (tuned from black) are from a calibration image, while cyan dots (tuned from black) are from a measurement image of surface ripples, and the overlap is in blue. (c) The displacements $\delta\mathbf{r}$ (amplified 4 times in length for clarity) between the pink and the cyan dots in (b).	83
4.4	Schematic of measuring topography and height of liquid ripples in a tank. The dimensions are not in scale.	85
4.5	The contours of topography from the FS-SS method (a) and from our method (b). (c) Comparison of $h - \bar{h}$ between present method and FS-SS method in experiments of dynamic ripples, where the gray squares denote individual data in space. A black dot shows the average of the individual points in a bin with the size of 0.3 mm, and an error bar shows the standard deviation of the data in the bin.	87
4.6	The effects of initial guesses in Newton method on $h(x, y)$ in solution. (a) The mean height \bar{h} resulted from initial guesses $h_0 = 15, 20, 25, 30$ against iteration steps, where the inset shows a zoom for iteration steps larger than 18. (b–d) The contours of topography differences, $h(x, y, h_0 = 30) - h(x, y, h_0 = 20)$, $h(x, y, h_0 = 25) - h(x, y, h_0 = 20)$ and $h(x, y, h_0 = 15) - h(x, y, h_0 = 20)$, respectively.	88

4.7	The different flat surfaces with the same calibration viewing angles, $\beta(x, y)$. (a) The contour of the 10 mm surface height. (b) The contour of the 20 mm surface height.	88
4.8	(a) Side view schematic of a lock-exchange experimental setup for propagation of current fronts in a dam-break flow. The camera and illumination systems are the same as in figure 4.4. (b) Top-view schematic of visualization measurements. The thick black arrow indicates the flow direction, and the gray rectangular marks the area where $h(x, y)$ is measured. The dot lines enclose the field-of-view of the visualization camera, and the dash line marks the perspective view of the camera. The dimensions are not in scale.	89
4.9	(a) Contours of a sample $h(x, y)$ of the current body at $t - t_f = 234$ ms. (b) Time series of \bar{h} for the current body, where $t_f (= 152$ ms) is time duration of the current front passing the measurement domain. The gate is opened at $t \approx -40$ ms.	91
4.10	Illustration of the image processing in the visualization measurement: (a) The image of the standard deviation of the background images; (b) A sample of visualization image; (c) The tuned image with marking the pixel with grayscale larger (or smaller) than three times of the standard deviation as black (or white), where a red line marks the height profile. Illustration of obtaining $h_n(x)$ (e) from $h(x, y)$ (d), where dashed lines indicate the perspective direction and five red squares denote the data from the five dashed lines.	91
4.11	Comparison of streamwise profiles of current body between the visualization and present method. (a) The streamwise profiles $h_v(x)$ (visualization) and $h_n(x)$ (present method) along the streamwise direction x . Gray band show the error bar of visualization measurement. (b) $h_n(x)$ versus $h_v(x)$, where individual data are shown in points and the grayscale level indicates the probability density function (pdf) (the darker the larger pdf), and red squares show the bin-averaged data.	92

4.12	(a) Contours of a sample of the current front with no numerical noise. (b) The height profile of the current front, where the blue solid line shows the profile at $y = 25$ mm in (a). The red dashed line shows a typical profile of a gravity current, which is extracted from the top panel of figure 4 in Maxworthy et al. [108], and the values are adjusted to shown in the same figure. (c) Contours of a sample of the current front with spike-like numerical noise downstream of the front.	93
4.13	(a) Spatio-temporal diagram of the current fronts, where the color indicates the $h(x, y)$ averaged over y , $(\bar{h})_y(x) = \sum_{i=1}^N h(x, y_i)/N$. The dash line indicates the front speed in our experiments. The front speed of Lowe et al. [105] is nearly the same as our experiments and is also denoted by this dash line. The dash-dot line indicates the front speed of Adegok et al. [1]. (b) The corresponding spatial averaged height $\bar{h}(t)$, in sharing the same axis t	94
4.14	(a) Radially averaged spectra of $h(x, y) - \bar{h}$ for three interrogation window sizes. The inset shows the same data in logarithm-logarithm axes. (b–d) Contours of the same region obtained with interrogation window 24^2 , 48^2 and 96^2 pixels ² , respectively.	100
4.15	The illustration of breakdown condition of the working principle: (a) Large oscillation amplitude of surface wave, where the light ray is refracted more than once as marked by hollow triangles. (b) Critical condition for formation of caustics.	101
4.16	Contours of a sample of the surface ripples (the same snapshot as in figure 4.5 which is obtained by solving (a) the linearized equation (4.2), (b) equation (4.1) and (c) their difference. . .	102
4.17	Contours of a sample of the current body (the same snapshot as in figure 4.9) obtained by solving (a) the linearized equation (4.2) and (b) equation (4.1) and (c) their difference. . . .	102
4.18	Contours of a sample of the current body (the same snapshot as in figure 4.12) obtained by solving (a) the linearized equation (4.2) and (b) equation (4.1) and (c) their difference. (d) Three height profiles chosen from (a) (solid lines) and (b) (dashed lines) at $y = 15$ mm, 35 mm and 55 mm.	103

List of Tables

2.1	The list of the main geometry parameters for the T-mixer system.	29
3.1	The list of studies on tracer position error (or angle deflection) from inhomogeneous refractive index field.	50
3.2	Parameters in the simulation cases.	56
4.1	A brief list of refraction methods for free surface measurements.	80
4.2	The averaged surface height \bar{h} computed from the displacements including the camera vibration $\delta\mathbf{r} + \delta\mathbf{r}_{\text{vibration}}$ for the measurement sample of \bar{h} from the experiments of liquid ripples, and $\delta\mathbf{r}_{\text{vibration}}(x, y) = c_r y + c_t$	98
4.3	The relative errors (%) of $\bar{h}(x, y)$ referring to the case $c_r = 0$ and $c_t = 0$ in table 4.2.	98
4.4	The effect of interrogation window size on the surface height and topography of the snapshot in figure 4.5(c).	99

Bibliography

- [1] P. B. Adegok, W. Atherton, and R. M. A. Khaddar. A novel simple method for measuring the velocity of dam-break flow. *WIT Transactions on Ecology and the Environment*, 184:23–34, 2014.
- [2] R. Afshar Ghotli, A. A. Raman, S. Ibrahim, and S. Baroutian. Liquid-liquid mixing in stirred vessels: a review. *Chemical Engineering Communications*, 200(5):595–627, 2013.
- [3] R. S. Alnayli, Z. S. Shanon, and A. S. Hadi. Study the linear and nonlinear optical properties for laser dye Rhodamine B. In *Journal of Physics: Conference Series*, volume 1234, page 012022. IOP Publishing, 2019.
- [4] M. A. André and P. M. Bardet. Velocity field, surface profile and curvature resolution of steep and short free-surface waves. *Experiments in Fluids*, 55:1709, 2014.
- [5] K. E. Atkinson. *An Introduction to Numerical Analysis*. John Wiley & Sons, 2 edition, 1989.
- [6] F. Aureli, S. Dazzi, A. Maranzoni, and P. Mignosa. A combined colour-infrared imaging technique for measuring water surface over non-horizontal bottom. *Experiments in Fluids*, 55(3):1701, 2014.
- [7] K. Bai and J. Katz. On the refractive index of sodium iodide solutions for index matching in PIV. *Experiments in Fluids*, 55:1704, 2014.
- [8] S. Banerjee, D. Scott, and E. Rhodes. Mass transfer to falling wavy liquid films in turbulent flow. *Industrial & Engineering Chemistry Fundamentals*, 7(1):22–27, 1968.

- [9] M. Banner and O. Phillips. On the incipient breaking of small scale waves. *Journal of Fluid Mechanics*, 65(4):647–656, 1974.
- [10] G. K. Batchelor. Small-scale variation of convected quantities like temperature in turbulent fluid Part 1. general discussion and the case of small conductivity. *Journal of Fluid Mechanics*, 5(1):113–133, 1959.
- [11] G. Belforte, G. Mattiazzo, S. Mauro, and L. Tokashiki. Measurement of friction force in pneumatic cylinders. *Tribotest*, 10(1):33–48, 2003.
- [12] J. H. Bell and R. D. Mehta. Contraction design for small low-speed wind tunnels. Technical report, 1988.
- [13] E. J. Bock, T. Hara, N. M. Frew, and W. R. McGillis. Relationship between air-sea gas transfer and short wind waves. *Journal of Geophysical Research: Oceans*, 104(C11):25821–25831, 1999.
- [14] E. Bodenschatz, W. Pesch, and G. Ahlers. Recent developments in Rayleigh-Bénard convection. *Annual Review of Fluid Mechanics*, 32(1):709–778, 2000.
- [15] Z. Borden and E. Meiburg. Circulation based models for Boussinesq gravity currents. *Physics of Fluids*, 25:101301, 2013.
- [16] M. Born, E. Wolf, A. B. Bhatia, P. C. Clemmow, D. Gabor, A. R. Stokes, A. M. Taylor, P. A. Wayman, and W. L. Wilcock. *Principles of Optics: Electromagnetic Theory of Propagation, Interference and Diffraction of Light*. Cambridge University Press, 7 edition, 1999.
- [17] P. Bradshaw and R. Pankhurst. The design of low-speed wind tunnels. *Progress in Aerospace Sciences*, 5:1–69, 1964.
- [18] Y. Brahami. *Active scalar mixing in turbulent jet flows*. PhD thesis, Normandie Université, 2020.
- [19] M. S. Brito, C. P. Fonte, M. M. Dias, J. C. B. Lopes, and R. J. Santos. Flow regimes and mixing of dissimilar fluids in T-jets mixers. *Chemical Engineering & Technology*, 45(2):355–364, 2022.
- [20] D. Buaria, M. P. Clay, K. R. Sreenivasan, and P. Yeung. Small-scale isotropy and ramp-cliff structures in scalar turbulence. *Physical Review Letters*, 126(3):034504, 2021.

- [21] D. Buaria, M. P. Clay, K. R. Sreenivasan, and P. Yeung. Turbulence is an ineffective mixer when Schmidt numbers are large. *Physical Review Letters*, 126(7):074501, 2021.
- [22] P. Burattini, P. Lavoie, A. Agrawal, L. Djenidi, and R. Antonia. Power law of decaying homogeneous isotropic turbulence at low Reynolds number. *Physical Review E*, 73(6):066304, 2006.
- [23] S. Camarri, A. Mariotti, C. Galletti, E. Brunazzi, R. Mauri, and M. V. Salvetti. An overview of flow features and mixing in micro T and arrow mixers. *Industrial & Engineering Chemistry Research*, 59(9):3669–3686, 2020.
- [24] J. Carlier and K. Sodjavi. Turbulent mixing and entrainment in a stratified horizontal plane shear layer: joint velocity-temperature analysis of experimental data. *Journal of Fluid Mechanics*, 806:542–579, 2016.
- [25] H. J. Catrakis and P. E. Dimotakis. Mixing in turbulent jets: scalar measures and isosurface geometry. *Journal of Fluid Mechanics*, 317:369–406, 1996.
- [26] P. Chatwin and P. J. Sullivan. The effect of aspect ratio on longitudinal diffusivity in rectangular channels. *Journal of Fluid Mechanics*, 120:347–358, 1982.
- [27] D. Chaudhuri, D. Sengupta, E. D’Asaro, R. Venkatesan, and M. Ravichandran. Response of the salinity-stratified bay of bengal to cyclone phailin. *Journal of Physical Oceanography*, 49(5):1121–1140, 2019.
- [28] R. A. Chaudhury, M. Herrmann, D. H. Frakes, and R. J. Adrian. Length and time for development of laminar flow in tubes following a step increase of volume flux. *Experiments in Fluids*, 56(1):1–10, 2015.
- [29] S. K. R. Cherlo and S. Pushpavanam. Effect of depth on onset of engulfment in rectangular micro-channels. *Chemical Engineering Science*, 65(24):6486–6490, 2010.

- [30] M. P. Clay. *Strained turbulence and low-diffusivity turbulent mixing using high performance computing*. PhD thesis, Georgia Institute of Technology, 2017.
- [31] P. J. Cobelli, A. Maurel, V. Pagneux, and P. Petitjeans. Global measurement of water waves by Fourier transform profilometry. *Experiments in Fluids*, 46(6):1037–1047, 2009.
- [32] S. Corrsin. On the spectrum of isotropic temperature fluctuations in an isotropic turbulence. *Journal of Applied Physics*, 22(4):469–473, 1951.
- [33] J. Crimaldi. The effect of photobleaching and velocity fluctuations on single-point LIF measurements. *Experiments in Fluids*, 23(4):325–330, 1997.
- [34] J. Crimaldi. Planar laser induced fluorescence in aqueous flows. *Experiments in Fluids*, 44(6):851–863, 2008.
- [35] D. Dabiri, X. Zhang, and M. Gharib. Quantitative visualization of three-dimensional free surface slopes and elevations. In Y. Nakayama, editor, *Atlas of Visualization*. CRC Press LLC Boca Raton, 1997.
- [36] W. J. Dahm and K. A. Buch. Lognormality of the scalar dissipation pdf in turbulent flows. *Physics of Fluids A: Fluid Dynamics*, 1(7):1290–1293, 1989.
- [37] P. Danckwerts. Significance of liquid-film coefficients in gas absorption. *Industrial & Engineering Chemistry*, 43(6):1460–1467, 1951.
- [38] L. Dasi, F. Schuerg, and D. Webster. The geometric properties of high-Schmidt-number passive scalar iso-surfaces in turbulent boundary layers. *Journal of Fluid Mechanics*, 588:253–277, 2007.
- [39] P. Davidovits, C. E. Kolb, L. R. Williams, J. T. Jayne, and D. R. Worsnop. Mass accommodation and chemical reactions at gas-liquid interfaces. *Chemical Reviews*, 106(4):1323–1354, 2006.
- [40] P. A. Davidson. *Turbulence: An Introduction for Scientists and Engineers*. Oxford University Press, 2015.

- [41] M. A. de Araújo, R. Silva, E. de Lima, D. P. Pereira, and P. C. de Oliveira. Measurement of gaussian laser beam radius using the knife-edge technique: improvement on data analysis. *Applied Optics*, 48(2):393–396, 2009.
- [42] A. de Lamotte, A. Delafosse, S. Calvo, F. Delvigne, and D. Toye. Investigating the effects of hydrodynamics and mixing on mass transfer through the free-surface in stirred tank bioreactors. *Chemical Engineering Science*, 172:125–142, 2017.
- [43] J. A. Dijkman, F. Rietz, K. A. Lörincz, M. van Hecke, and W. Losert. Refractive index matched scanning of dense granular materials. *Review of Scientific Instruments*, 83(1):011301, 2012.
- [44] P. E. Dimotakis. Turbulent mixing. *Annual Review of Fluid Mechanics*, 37:329–356, 2005.
- [45] P. E. Dimotakis, H. J. Catrakis, and D. C. Fourchette. Flow structure and optical beam propagation in high-Reynolds-number gas-phase shear layers and jets. *Journal of Fluid Mechanics*, 433:105–134, 2001.
- [46] M. Dizechi and E. Marschall. Viscosity of some binary and ternary liquid mixtures. *Journal of Chemical and Engineering Data*, 27(3):358–363, 1982.
- [47] J. H. Duncan, H. Qiao, V. Philomin, and A. Wenz. Gentle spilling breakers: crest profile evolution. *Journal of Fluid Mechanics*, 379:191–222, 1999.
- [48] C. Eckart. An analysis of the stirring and mixing processes in incompressible fluids. *Journal of Marine Research*, 7:265–275, 1948.
- [49] J. Edson, C. J. Zappa, J. Ware, W. R. McGillis, and J. Hare. Scalar flux profile relationships over the open ocean. *Journal of Geophysical Research: Oceans*, 109(C8), 2004.
- [50] G. E. Elsinga and G. C. Orlicz. Particle imaging through planar shock waves and associated velocimetry errors. *Experiments in Fluids*, 56(6):129, Jun 2015.

- [51] G. E. Elsinga, B. W. van Oudheusden, and F. Scarano. Evaluation of aero-optical distortion effects in PIV. *Experiments in Fluids*, 39(2):246–256, Aug 2005.
- [52] L. Engelen, S. Creëlle, L. Schindfessel, and T. De Mulder. Spatio-temporal image-based parametric water surface reconstruction: a novel methodology based on refraction. *Measurement Science and Technology*, 29(3):035302, 2018.
- [53] M. Engler, N. Kockmann, T. Kiefer, and P. Woias. Numerical and experimental investigations on liquid mixing in static micromixers. *Chemical Engineering Journal*, 101(1–3):315–322, 2004.
- [54] M. Faden, C. Linhardt, S. Höhlein, A. König-Haagen, and D. Brüggemann. Velocity field and phase boundary measurements during melting of n-octadecane in a cubical test cell. *International Journal of Heat and Mass Transfer*, 135:104–114, 2019.
- [55] A. Fani, S. Camarri, and M. V. Salvetti. Investigation of the steady engulfment regime in a three-dimensional T-mixer. *Physics of Fluids*, 25(6):064102, 2013.
- [56] A. Fani, S. Camarri, and M. V. Salvetti. Unsteady asymmetric engulfment regime in a T-mixer. *Physics of Fluids*, 26(7):074101, 2014.
- [57] A. Fouras, D. L. Jacono, G. J. Sheard, and K. Hourigan. Measurement of instantaneous velocity and surface topography in the wake of a cylinder at low Reynolds number. *Journal of Fluids and Structures*, 24(8):1271–1277, 2008.
- [58] G. L. Foutch and A. H. Johannes. Reactors in process engineering. In R. A. Meyers, editor, *Encyclopedia of Physical Science and Technology*, pages 23–43. Academic Press, New York, 3 edition, 2003.
- [59] S. T. Fredriksson. *Estimating the air-water gas transfer velocity during low wind conditions*. PhD thesis, University of Gothenburg, 2016.
- [60] C. Gibson and W. Schwarz. The universal equilibrium spectra of turbulent velocity and scalar fields. *Journal of Fluid Mechanics*, 16(3):365–384, 1963.

- [61] L. GmbH. *Product-Manual for DaVis 10.0: FlowMaster*. LaVision GmbH, Göttingen, Anna-Vandenhoeck-Ring 19, D-37081 Göttingen, 4 2018.
- [62] G. Gomit, L. Chatellier, D. Calluau, and L. David. Free surface measurement by stereo-refraction. *Experiments in Fluids*, 54(6):1540, 2013.
- [63] T. Gotoh and P. Yeung. Passive scalar transport in turbulence: A computational perspective. In P. A. Davidson, Y. Kaneda, and K. R. Sreenivasan, editors, *Ten Chapters in Turbulence*, pages 87–131. Cambridge University Press, 2012.
- [64] J. Gradl and W. Peukert. Characterization of micro mixing for precipitation of nanoparticles in a T-mixer. In *Micro and Macro Mixing*, pages 105–124. Springer, 2010.
- [65] E. Grandjean and P. A. Monkewitz. Experimental investigation into localized instabilities of mixed Rayleigh-Bénard-Poiseuille convection. *Journal of Fluid Mechanics*, 640:401–419, 2009.
- [66] H. Grant, B. Hughes, W. Vogel, and A. Moilliet. The spectrum of temperature fluctuations in turbulent flow. *Journal of Fluid Mechanics*, 34(3):423–442, 1968.
- [67] B. D. Guenther. *Modern Optics*. Oxford University Press, 2 edition, 2015.
- [68] L. Gui and W. Merzkirch. A comparative study of the MQD method and several correlation-based PIV evaluation algorithms. *Experiments in Fluids*, 28(1):36–44, 2000.
- [69] G. Guo, H. Liu, and B. Zhang. Aero-optical effects of an optical seeker with a supersonic jet for hypersonic vehicles in near space. *Applied Optics*, 55(17):4741–4751, 2016.
- [70] X. Guo and L. Shen. Numerical study of the effect of surface waves on turbulence underneath. Part 1. Mean flow and turbulence vorticity. *Journal of Fluid Mechanics*, 733:558–587, 2013.
- [71] X. He, X. Shang, and P. Tong. Test of the anomalous scaling of passive temperature fluctuations in turbulent Rayleigh-Bénard convection

- with spatial inhomogeneity. *Journal of Fluid Mechanics*, 753:104–130, 2014.
- [72] Herlina and G. H. Jirka. Experiments on gas transfer at the air-water interface induced by oscillating grid turbulence. *Journal of Fluid Mechanics*, 594:183–208, 2008.
- [73] H. Herlina and J. Wissink. Direct numerical simulation of turbulent scalar transport across a flat surface. *Journal of Fluid Mechanics*, 744:217–249, 2014.
- [74] H. Herlina and J. Wissink. Simulation of air-water interfacial mass transfer driven by high-intensity isotropic turbulence. *Journal of Fluid Mechanics*, 860:419–440, 2019.
- [75] M. Hoffmann, M. Schlüter, and N. Rübiger. Experimental investigation of liquid-liquid mixing in T-shaped micro-mixers using μ -LIF and μ -PIV. *Chemical Engineering Science*, 61(9):2968–2976, 2006.
- [76] H. Hu, B. Wang, K. Zhang, W. Lohry, and S. Zhang. Quantification of transient behavior of wind-driven surface droplet/rivulet flows using a digital fringe projection technique. *Journal of Visualization*, 18(4):705–718, 2015.
- [77] A. Issakhov and A. Baitureyeva. Modeling of a passive scalar transport from thermal power plants to atmospheric boundary layer. *International Journal of Environmental Science and Technology*, 16(8):4375–4392, 2019.
- [78] K. Iwano, J. Hosoi, Y. Sakai, and Y. Ito. Power spectrum of high Schmidt number scalar in a turbulent jet at a moderate Reynolds number. *Experiments in Fluids*, 62(6):1–6, 2021.
- [79] K. P. Iyer, J. Schumacher, K. R. Sreenivasan, and P. Yeung. Steep cliffs and saturated exponents in three-dimensional scalar turbulence. *Physical Review Letters*, 121(26):264501, 2018.
- [80] B. Jähne and H. Haußecker. Air-water gas exchange. *Annual Review of Fluid Mechanics*, 30(1):443–468, 1998.

- [81] B. Jähne, M. Schmidt, and R. Rocholz. Combined optical slope/height measurements of short wind waves: principle and calibration. *Measurement Science and Technology*, 16(10):1937, 2005.
- [82] T. F. Johnston. Beam propagation (M^2) measurement made as easy as it gets: the four-cuts method. *Applied Optics*, 37(21):4840–4850, 1998.
- [83] E. J. Jumper and S. Gordeyev. Physics and measurement of aero-optical effects: past and present. *Annual Review of Fluid Mechanics*, 49:419–441, 2017.
- [84] S. A. Kaiser, J. H. Frank, and M. B. Long. Use of Rayleigh imaging and ray tracing to correct for beam-steering effects in turbulent flames. *Applied Optics*, 44(31):6557–6564, 2005.
- [85] G. Karimi and M. Kawaji. An experimental study of freely falling films in a vertical tube. *Chemical Engineering Science*, 53(20):3501–3512, 1998.
- [86] B. J. Kim, Y. Z. Liu, and H. J. Sung. Micro PIV measurement of two-fluid flow with different refractive indices. *Measurement Science and Technology*, 15(6):1097, 2004.
- [87] J. Kim and P. Moin. Transport of passive scalars in a turbulent channel flow. In *Turbulent Shear Flows 6*, pages 85–96. Springer, 1989.
- [88] T. Kirmse, J. Agocs, A. Schröder, J. M. Schramm, S. Karl, and K. Hanne-mann. Application of particle image velocimetry and the background-oriented schlieren technique in the high-enthalpy shock tunnel Göttingen. *Shock Waves*, 21(3):233–241, 2011.
- [89] T. Kirmse, A. Gardner, and C. Krombholz. Investigation of aero-optical effects in model deformation measurements in a transonic flow. In A. Dillmann, G. Heller, H.-P. Kreplin, W. Nitsche, and I. Peltzer, editors, *New Results in Numerical and Experimental Fluid Mechanics VIII: Contributions to the 17th STAB/DGLR Symposium Berlin, Germany 2010*, pages 665–672. Springer Berlin Heidelberg, Berlin, Heidelberg, 2013.

- [90] J. Kolaas, B. H. Riise, K. Sveen, and A. Jensen. Bichromatic synthetic Schlieren applied to surface wave measurements. *Experiments in Fluids*, 59(8):128, 2018.
- [91] A. N. Kolmogorov. Dissipation of energy in the locally isotropic turbulence. *Reprinted in Proceedings of the Royal Society of London. Series A: Mathematical and Physical Sciences*, 434(1890):15–17, 1991.
- [92] A. N. Kolmogorov. The local structure of turbulence in incompressible viscous fluid for very large Reynolds numbers. *Reprinted in Proceedings of the Royal Society of London. Series A: Mathematical and Physical Sciences*, 434(1890):9–13, 1991.
- [93] R. H. Kraichnan. Small-scale structure of a scalar field convected by turbulence. *Physics of Fluids*, 11:945–953, 1968.
- [94] E. B. Kraus and J. A. Businger. *Atmosphere-ocean interaction*, volume 27. Oxford University Press, 1994.
- [95] V. Kudryavtsev, B. Chapron, and V. Makin. Impact of wind waves on the air-sea fluxes: A coupled model. *Journal of Geophysical Research: Oceans*, 119(2):1217–1236, 2014.
- [96] J. Kurata, K. Grattan, H. Uchiyama, and T. Tanaka. Water surface measurement in a shallow channel using the transmitted image of a grating. *Review of Scientific Instruments*, 61(2):736–739, 1990.
- [97] R. Kuyper, T. H. Van Der Meer, C. Hoogendoorn, and R. Henkes. Numerical study of laminar and turbulent natural convection in an inclined square cavity. *International Journal of Heat and Mass Transfer*, 36(11):2899–2911, 1993.
- [98] G. Lauber and W. H. Hager. Experiments to dam-break waves: Horizontal channel. *Journal of Hydraulic Research*, 36(3):291–307, 1998.
- [99] C. K. Law. *Combustion Physics*. Cambridge University Press, 2010.
- [100] W. K. Lewis and W. G. Whitman. Principles of gas absorption. *Industrial & Engineering Chemistry*, 16(12):1215–1220, 1924.
- [101] J. H. Liang, S. R. Emerson, E. A. D’Asaro, C. L. McNeil, R. R. Harcourt, P. P. Sullivan, B. Yang, and M. F. Cronin. On the role of sea-state in

- bubble-mediated air-sea gas flux during a winter storm. *Journal of Geophysical Research: Oceans*, 122(4):2671–2685, 2017.
- [102] D. Livescu, C. Canada, K. Kanov, R. Burns, IDIES staff, and J. Pulido. Homogeneous buoyancy driven turbulence data set, available at <http://turbulence.pha.jhu.edu/docs/README-HBDT.pdf>, 2014.
- [103] D. Livescu and J. Ristorcelli. Buoyancy-driven variable-density turbulence. *Journal of Fluid Mechanics*, 591:43–71, 2007.
- [104] D. Lohse and K.-Q. Xia. Small-scale properties of turbulent Rayleigh-Bénard convection. *Annual Review of Fluid Mechanics*, 42:335–364, 2010.
- [105] R. J. Lowe, J. W. Rottman, and P. F. Linden. The non-Boussinesq lock-exchange problem. Part 1. Theory and experiments. *Journal of Fluid Mechanics*, 537:101, 2005.
- [106] X.-H. Ma, X.-D. Zhou, Z. Lan, L. Yi-Ming, and Y. Zhang. Condensation heat transfer enhancement in the presence of non-condensable gas using the interfacial effect of dropwise condensation. *International Journal of Heat and Mass Transfer*, 51(7-8):1728–1737, 2008.
- [107] J. C. Maxwell. *The scientific papers of James Clerk Maxwell*, volume 1 of *Cambridge Library Collection - Physical Sciences*. Cambridge University Press, 2011.
- [108] T. Maxworthy, J. Leilich, J. E. Simpson, and E. H. Meiburg. The propagation of a gravity current into a linearly stratified fluid. *Journal of Fluid Mechanics*, 453:371–394, 2002.
- [109] W. R. McGillis, J. B. Edson, C. J. Zappa, J. D. Ware, S. P. McKenna, E. A. Terray, J. E. Hare, C. W. Fairall, W. Drennan, M. Donelan, et al. Air-sea CO₂ exchange in the equatorial pacific. *Journal of Geophysical Research: Oceans*, 109(C8), 2004.
- [110] S. P. McKenna. *Free-surface turbulence and air-water gas exchange*. PhD thesis, Massachusetts Institute of Technology, 2000.
- [111] P. L. Miller and P. E. Dimotakis. Reynolds number dependence of scalar fluctuations in a high Schmidt number turbulent jet. *Physics of Fluids A: Fluid Dynamics*, 3(5):1156–1163, 1991.

- [112] P. L. Miller and P. E. Dimotakis. Stochastic geometric properties of scalar interfaces in turbulent jets. *Physics of Fluids A: Fluid Dynamics*, 3(1):168–177, 1991.
- [113] P. L. Miller and P. E. Dimotakis. Measurements of scalar power spectra in high Schmidt number turbulent jets. *Journal of Fluid Mechanics*, 308:129–146, 1996.
- [114] A. Minakov, V. Rudyak, A. Dekterev, and A. Gavrilov. Investigation of slip boundary conditions in the T-shaped microchannel. *International Journal of Heat and Fluid Flow*, 43:161–169, 2013.
- [115] F. Moisy, M. Rabaud, and K. Salsac. A synthetic Schlieren method for the measurement of the topography of a liquid interface. *Experiments in Fluids*, 46(6):1021, 2009.
- [116] N. J. W. Morris. *Image-based water surface reconstruction with refractive stereo*. PhD thesis, 2004.
- [117] V. Mosorov. Applications of tomography in reaction engineering (mixing process). In *Industrial Tomography*, pages 509–528. Elsevier, 2015.
- [118] I. Ng, V. Kumar, G. J. Sheard, K. Hourigan, and A. Fouras. Experimental study of simultaneous measurement of velocity and surface topography: in the wake of a circular cylinder at low Reynolds number. *Experiments in Fluids*, 50(3):587–595, 2011.
- [119] F. Nicolas, V. Todoroff, A. Plyer, G. Le Besnerais, D. Donjat, F. Micheli, F. Champagnat, P. Cornic, and Y. Le Sant. A direct approach for instantaneous 3D density field reconstruction from background-oriented schlieren (BOS) measurements. *Experiments in Fluids*, 57(1):1–21, 2016.
- [120] X. Nicolas, A. Mojtabi, and J. K. Platten. Two-dimensional numerical analysis of the Poiseuille-Bénard flow in a rectangular channel heated from below. *Physics of Fluids*, 9(2):337–348, 1997.
- [121] C. Noss, P. Bodmer, K. Koca, and A. Lorke. Flow and turbulence driven water surface roughness and gas exchange velocity in streams. In *E3S Web of Conferences*, volume 40, page 05018. EDP Sciences, 2018.

- [122] P. Odier, J. Chen, and R. E. Ecke. Entrainment and mixing in a laboratory model of oceanic overflow. *Journal of Fluid Mechanics*, 746:498–535, 2014.
- [123] M. Oljaca and A. Glezer. The effects of induced dissipative small-scale motions and mixing on optical distortion in a plane shear layer. *Journal of Fluid Mechanics*, 619:295–329, 2009.
- [124] G. Paolillo and T. Astarita. On the PIV/PTV uncertainty related to calibration of camera systems with refractive surfaces. *Measurement Science and Technology*, 32(9):094006, 2021.
- [125] V. A. Patil and J. A. Liburdy. Optical measurement uncertainties due to refractive index mismatch for flow in porous media. *Experiments in Fluids*, 53(5):1453–1468, 2012.
- [126] E. L. Paul, V. A. Atiemo-Obeng, and S. M. Kresta. *Handbook of Industrial Mixing*. Wiley Online Library, 2004.
- [127] M. Pinelli, H. Herlina, J. G. Wissink, and M. Uhlmann. Direct numerical simulation of turbulent mass transfer at the surface of an open channel flow. *Journal of Fluid Mechanics*, 933, 2022.
- [128] H. Pitsch and H. Steiner. Scalar mixing and dissipation rate in large-eddy simulations of non-premixed turbulent combustion. *Proceedings of the Combustion Institute*, 28(1):41–49, 2000.
- [129] R. Poole, M. Alfateh, and A. Gauntlett. Bifurcation in a T-channel junction: Effects of aspect ratio and shear-thinning. *Chemical Engineering Science*, 104:839–848, 2013.
- [130] S. B. Pope. *Turbulent Flows*. Cambridge University Press, 2000.
- [131] P. Poredoš, N. Petelin, T. Žel, B. Vidrih, P. Gatarić, and A. Kitanovski. Performance of the condensation process for water vapour in the presence of a non-condensable gas on vertical plates and horizontal tubes. *Energies*, 14(8):2291, 2021.
- [132] M. Raffel. Background-oriented schlieren (BOS) techniques. *Experiments in Fluids*, 56(3):60, 2015.

- [133] M. Raffel and F. Kost. Investigation of aerodynamic effects of coolant ejection at the trailing edge of a turbine blade model by PIV and pressure measurements. *Experiments in Fluids*, 24(5-6):447–461, 1998.
- [134] M. Raffel, C. E. Willert, F. Scarano, C. J. Kähler, S. T. Wereley, and J. Kompenhans. *Particle Image Velocimetry: A Practical Guide*. Springer, 3 edition, 2018.
- [135] L. K. Rajendran, S. P. M. Bane, and P. P. Vlachos. PIV/BOS synthetic image generation in variable density environments for error analysis and experiment design. *Measurement Science and Technology*, 30(8):085302, 2019.
- [136] J. F. Ready. *Industrial Applications of Lasers*. Elsevier, 1997.
- [137] L. F. Richardson. *Weather Prediction by Numerical Process*. Cambridge University Press, 1992.
- [138] H. Riebeek and R. Simmon. The ocean’s carbon balance, 2008.
- [139] M. Sakai, T. Ohmori, and M. Fujii. Two-color picosecond time-resolved infrared super-resolution microscopy. *Handai Nanophotonics*, 3:189–195, 2007.
- [140] R. Savelsberg and W. van de Water. Turbulence of a free surface. *Physical Review Letters*, 100(3):034501, 2008.
- [141] T. Schikarski and M. Avila. T-mixer a novel system to investigate decaying turbulence in a wall-bounded environment. In *16th European Turbulence Conference*, 2017.
- [142] T. Schikarski, W. Peukert, and M. Avila. Direct numerical simulation of water-ethanol flows in a T-mixer. *Chemical Engineering Journal*, 324:168–181, 2017.
- [143] T. Schikarski, H. Trzenschiok, W. Peukert, and M. Avila. Inflow boundary conditions determine T-mixer efficiency. *Reaction Chemistry & Engineering*, 4(3):559–568, 2019.
- [144] J. F. G. Schneiders, S. Pröbsting, R. P. Dwight, B. W. van Oudheusden, and F. Scarano. Pressure estimation from single-snapshot tomographic

- PIV in a turbulent boundary layer. *Experiments in Fluids*, 57(4):53, Mar 2016.
- [145] F. Schwertfirm, J. Gradl, H. C. Schwarzer, W. Peukert, and M. Manhart. The low Reynolds number turbulent flow and mixing in a confined impinging jet reactor. *International Journal of Heat and Fluid Flow*, 28(6):1429–1442, 2007.
- [146] R. K. Shah and A. L. London. *Laminar flow forced convection in ducts: a source book for compact heat exchanger analytical data*. Academic press, 2014.
- [147] A. Sharma, D. V. Kumar, and A. K. Ghatak. Tracing rays through graded-index media: a new method. *Applied Optics*, 21(6):984–987, 1982.
- [148] J. O. Shin, S. B. Dalziel, and P. F. Linden. Gravity currents produced by lock exchange. *Journal of Fluid Mechanics*, 521:1–34, 2004.
- [149] L. Skrbek and S. R. Stalp. On the decay of homogeneous isotropic turbulence. *Physics of Fluids*, 12(8):1997–2019, 2000.
- [150] A. Soleymani, H. Yousefi, and I. Turunen. Dimensionless number for identification of flow patterns inside a T-micromixer. *Chemical Engineering Science*, 63(21):5291–5297, 2008.
- [151] N. Soulopoulos, Y. Hardalupas, and A. Taylor. Mixing and scalar dissipation rate statistics in a starting gas jet. *Physics of Fluids*, 27(12):125103, 2015.
- [152] K. R. Sreenivasan. Turbulent mixing: A perspective. *Proceedings of the National Academy of Sciences*, 116(37):18175–18183, 2019.
- [153] S. R. Stalp, L. Skrbek, and R. J. Donnelly. Decay of grid turbulence in a finite channel. *Physical Review Letters*, 82(24):4831, 1999.
- [154] J. Stam and E. Languéno. Ray tracing in non-constant media. In X. Pueyo and P. Schröder, editors, *Rendering Techniques '96*, pages 225–234, Vienna, 1996. Springer Vienna.
- [155] A. Stella, G. Guj, J. Kompenhans, M. Raffel, and H. Richard. Application of particle image velocimetry to combusting flows: design

- considerations and uncertainty assessment. *Experiments in Fluids*, 30(2):167–180, 2001.
- [156] K. Stephan. *Heat Transfer in Condensation and Boiling*. Springer, 1 edition, 1992.
- [157] B. Talbot, N. Mazellier, B. Renou, L. Danaila, and M. A. Boukhalfa. Time-resolved velocity and concentration measurements in variable-viscosity turbulent jet flow. *Experiments in Fluids*, 47(4):769–787, 2009.
- [158] D. J. Tan, D. Edgington-Mitchell, and D. Honnery. Measurement of density in axisymmetric jets using a novel background-oriented schlieren (BOS) technique. *Experiments in Fluids*, 56(11):1–11, 2015.
- [159] T. Theofanous, R. Houze, and L. Brumfield. Turbulent mass transfer at free, gas-liquid interfaces, with applications to open-channel, bubble and jet flows. *International Journal of Heat and Mass Transfer*, 19(6):613–624, 1976.
- [160] S. Thomas, T. Ameel, and J. Guilkey. Mixing kinematics of moderate Reynolds number flows in a T-channel. *Physics of Fluids*, 22(1):013601, 2010.
- [161] S. Thomas and T. A. Ameel. An experimental investigation of moderate Reynolds number flow in a T-channel. *Experiments in Fluids*, 49(6):1231–1245, 2010.
- [162] R. Tsubaki and I. Fujita. Stereoscopic measurement of a fluctuating free surface with discontinuities. *Measurement Science and Technology*, 16(10):1894, 2005.
- [163] D. E. Turney and S. Banerjee. Air-water gas transfer and near-surface motions. *Journal of Fluid Mechanics*, 733:588–624, 2013.
- [164] D. E. Turney, W. C. Smith, and S. Banerjee. A measure of near-surface fluid motions that predicts air-water gas transfer in a wide range of conditions. *Geophysical Research Letters*, 32(4), 2005.
- [165] A. J. Ulseth, R. O. Hall, M. Boix Canadell, H. L. Madinger, A. Niayifar, and T. J. Battin. Distinct air-water gas exchange regimes in low-and high-energy streams. *Nature Geoscience*, 12(4):259–263, 2019.

- [166] V. Valori. PhD thesis, Delft University of Technology, 2018.
- [167] M. van Meerkerk, C. Poelma, and J. Westerweel. Scanning stereo-PLIF method for free surface measurements in large 3D domains. *Experiments in Fluids*, 61(1):19, 2020.
- [168] C. Vanderwel and S. Tavoularis. Measurements of turbulent diffusion in uniformly sheared flow. *Journal of Fluid Mechanics*, 754:488–514, 2014.
- [169] C. Vanselow and A. Fischer. Influence of inhomogeneous refractive index fields on particle image velocimetry. *Optics and Lasers in Engineering*, 107:221–230, 2018.
- [170] C. Vanselow, O. Hoppe, D. Stöbener, and A. Fischer. Stereoscopic particle image velocimetry in inhomogeneous refractive index fields of combustion flows. *Applied Optics*, 60(28):8716–8727, 2021.
- [171] C. Vanselow, D. Stöbener, J. Kiefer, and A. Fischer. Particle image velocimetry in refractive index fields of combustion flows. *Experiments in Fluids*, 60:149, 2019.
- [172] C. Vic, A. C. Naveira Garabato, J. Green, A. F. Waterhouse, Z. Zhao, A. Melet, C. de Lavergne, M. C. Buijsman, and G. R. Stephenson. Deep-ocean mixing driven by small-scale internal tides. *Nature Communications*, 10(1):1–9, 2019.
- [173] N. A. Vinnichenko, A. V. Pushtaev, Y. Y. Plaksina, and A. V. Uvarov. Measurements of liquid surface relief with moon-glade background oriented Schlieren technique. *Experimental Thermal and Fluid Science*, 114:110051, 2020.
- [174] T. Wang and W. R. Geyer. The balance of salinity variance in a partially stratified estuary: Implications for exchange flow, mixing, and stratification. *Journal of Physical Oceanography*, 48(12):2887–2899, 2018.
- [175] R. Wanninkhof, W. E. Asher, D. T. Ho, C. Sweeney, and W. R. McGillis. Advances in quantifying air-sea gas exchange and environmental forcing. *Annual Review of Marine Science*, 1:213–244, 2009.

- [176] Z. Warhaft. Passive scalars in turbulent flows. *Annual Review of Fluid Mechanics*, 32(1):203–240, 2000.
- [177] T. Watanabe and T. Gotoh. Statistics of a passive scalar in homogeneous turbulence. *New Journal of Physics*, 6(1):40, 2004.
- [178] J. Westerweel. Fundamentals of digital particle image velocimetry. *Measurement Science and Technology*, 8(12):1379, 1997.
- [179] F. White. *Fluid Mechanics*. McGraw-Hill Series in Mechanical Engineering. McGraw Hill, 2011.
- [180] B. Wieneke. PIV uncertainty quantification from correlation statistics. *Measurement Science and Technology*, 26:074002, 2015.
- [181] D. Xu and J. Chen. Experimental study of stratified jet by simultaneous measurements of velocity and density fields. *Experiments in Fluids*, 53(1):145–162, 2012.
- [182] D. Xu and J. Chen. Accurate estimate of turbulent dissipation rate using PIV data. *Experimental Thermal and Fluid Science*, 44:662–672, 2013.
- [183] C. Yu, M. Chang, and T. Lin. Structures of moving transverse and mixed rolls in mixed convection of air in a horizontal plane channel. *International Journal of Heat and Mass Transfer*, 40(2):333–346, 1997.
- [184] C. J. Zappa, W. E. Asher, A. T. Jessup, J. Klinke, and S. Long. Micro-breaking and the enhancement of air-water transfer velocity. *Journal of Geophysical Research: Oceans*, 109(C8), 2004.
- [185] C. J. Zappa, M. L. Banner, H. Schultz, A. Corrada-Emmanuel, L. B. Wolff, and J. Yalcin. Retrieval of short ocean wave slope using polarimetric imaging. *Measurement Science and Technology*, 19(5):055503, 2008.
- [186] C. J. Zappa, W. R. McGillis, P. A. Raymond, J. B. Edson, E. J. Hintsa, H. J. Zemmelen, J. W. Dacey, and D. T. Ho. Environmental turbulent mixing controls on air-water gas exchange in marine and aquatic systems. *Geophysical Research Letters*, 34(10), 2007.

- [187] K. Zha, S. Busch, C. Park, and P. C. Miles. A novel method for correction of temporally- and spatially-variant optical distortion in planar particle image velocimetry. *Measurement Science and Technology*, 27(8):085201, 2016.
- [188] G. Zhang, A. Xu, D. Zhang, Y. Li, H. Lai, and X. Hu. Delineation of the flow and mixing induced by Rayleigh-Taylor instability through tracers. *Physics of Fluids*, 33(7):076105, 2021.
- [189] J. Zhang, S. Liu, C. Cheng, W. Li, X. Xu, H. Liu, and F. Wang. Investigation of three-dimensional flow regime and mixing characteristic in T-jet reactor. *Chemical Engineering Journal*, 358:1561–1573, 2019.
- [190] X. Zhang and C. S. Cox. Measuring the two-dimensional structure of a wavy water surface optically: A surface gradient detector. *Experiments in Fluids*, 17(4):225–237, 1994.
- [191] Y. Zhou and W. H. Cabot. Time-dependent study of anisotropy in Rayleigh-Taylor instability induced turbulent flows with a variety of density ratios. *Physics of Fluids*, 31(8):084106, 2019.

